

Predicting brain mechanics during closed head impact

- numerical and constitutive aspects -

CIP-DATA LIBRARY TECHNISCHE UNIVERSITEIT EINDHOVEN

Brands, Davy W.A.

Predicting brain mechanics during closed head impact : numerical and constitutive aspects / by Davy W.A. Brands. - Eindhoven : Technische Universiteit Eindhoven, 2002.

Proefschrift. - ISBN 90-386-2713-0

NUGI 834

Trefwoorden: hoofd; letselbiomechanica / hersenweefsel; constitutieve modellering / hersenweefsel; materiaalkarakterisering / letselbiomechanica;

eindige-elementenmethode / hersenweefsel; golfvoortplanting; numerieke aspecten

Subject headings: head; injury biomechanics / brain tissue; constitutive modelling / brain tissue; material characterization / impact biomechanics; finite element modelling / brain tissue; wave propagation; numerical aspects

Printed by the University Press Facilities, Eindhoven, The Netherlands

This research was financially supported by TNO Prins Maurits Laboratory, The Netherlands and the University Research Program of Ford Motor company.

**Predicting brain mechanics during
closed head impact
- numerical and constitutive aspects -**

PROEFSCHRIFT

ter verkrijging van de graad van doctor
aan de Technische Universiteit Eindhoven,
op gezag van de Rector Magnificus, prof.dr. R.A. van Santen,
voor een commissie aangewezen door het College voor Promoties
in het openbaar te verdedigen op
donderdag 14 maart 2002 om 16.00 uur

door

Davy Wilhelmus Anna Brands

geboren te Maastricht

Dit proefschrift is goedgekeurd door de promotoren:

prof.dr.ir. D.H. van Campen

en

prof.dr.ir. J.S.H.M. Wismans

Copromotor:

dr.ir. P.H.M. Bovendeerd

voor Bianca
voor mijn ouders

Contents

| | |
|--|-----------|
| Summary | xi |
| 1 General introduction | 1 |
| 1.1 Introduction to head injury biomechanics | 2 |
| 1.1.1 Epidemiology of head injury | 2 |
| 1.1.2 Basic anatomy of the head | 2 |
| 1.1.3 Load-injury scheme | 3 |
| 1.1.4 Head injury criteria | 4 |
| 1.1.5 Head models | 6 |
| 1.2 Finite Element modelling of head impact | 9 |
| 1.2.1 Mathematical model | 9 |
| 1.2.2 Numerical solution method | 10 |
| 1.2.3 Model validation | 11 |
| 1.2.4 Conclusion | 12 |
| 1.3 Scope of study | 12 |
| 1.3.1 Objectives | 12 |
| 1.3.2 Strategy | 13 |
| 1.3.3 Outline of the thesis | 13 |
| 2 Numerical accuracy: analysis of wave propagation in blunt head impact | 15 |
| 2.1 Introduction | 16 |
| 2.2 Elementary theory on wave propagation | 16 |
| 2.2.1 Elastic wave equation | 16 |
| 2.2.2 Solution for 1-D elastic wave equation | 18 |
| 2.2.3 Viscoelastic theory | 19 |
| 2.3 Importance of wave phenomena in the human head | 20 |
| 2.3.1 Lower bound of frequency range | 20 |
| 2.3.2 Upper bound of frequency range | 21 |
| 2.3.3 Reflection: mode conversion | 22 |
| 2.4 Simulation of wave propagation: | |
| theoretical considerations | 23 |
| 2.4.1 Numerical stability | 23 |
| 2.4.2 Numerical accuracy | 23 |

| | | |
|----------|---|-----------|
| 2.5 | Simulation of wave propagation: numerical results | 26 |
| 2.5.1 | Analytical solution | 26 |
| 2.5.2 | The numerical model | 27 |
| 2.5.3 | Results | 28 |
| 2.6 | Discussion | 30 |
| 2.6.1 | Wave propagation during head impact | 30 |
| 2.6.2 | Numerical accuracy | 31 |
| 2.6.3 | Implications for existing head models | 32 |
| 2.6.4 | Methods of improvement | 33 |
| 2.7 | Conclusions | 34 |
| 3 | Comparison of the dynamic behaviour of brain tissue and two model materials | 35 |
| 3.1 | Introduction | 36 |
| 3.2 | Materials and methods | 36 |
| 3.3 | Results | 40 |
| 3.4 | Discussion | 42 |
| 3.5 | Conclusions | 45 |
| 3.6 | Acknowledgments | 45 |
| 4 | Large shear strain dynamic behaviour of brain tissue and silicone gel model material | 47 |
| 4.1 | Introduction | 48 |
| 4.2 | Materials and methods | 48 |
| 4.3 | Results | 54 |
| 4.4 | Discussion | 59 |
| 4.5 | Conclusions | 64 |
| 4.6 | Acknowledgments | 64 |
| 5 | A non-linear viscoelastic material model for brain tissue | 65 |
| 5.1 | Introduction | 66 |
| 5.2 | General formulation of the model | 66 |
| 5.2.1 | Multiplicative strain decomposition | 66 |
| 5.2.2 | Constitutive assumptions | 68 |
| 5.2.3 | Multi-mode description | 70 |
| 5.3 | Determination of brain tissue material parameters | 70 |
| 5.3.1 | Small strain experiments: Multi-mode Maxwell model | 71 |
| 5.3.2 | Large strain stress relaxation experiments | 72 |
| 5.3.3 | Bulk behaviour: Ultrasonic experiments | 74 |
| 5.4 | Numerical implementation | 75 |
| 5.4.1 | Time integration in MADYMO | 75 |
| 5.4.2 | Stress computation | 76 |
| 5.4.3 | Accuracy of the time integration scheme | 77 |
| 5.5 | Simulation of stress relaxation experiments | 79 |
| 5.5.1 | Model description | 79 |

| | | |
|----------|---|------------|
| 5.5.2 | Results | 79 |
| 5.5.3 | Discussion and conclusions | 80 |
| 5.6 | Conclusion | 81 |
| 6 | FE modelling of transient rotation of a simple physical head model | 83 |
| 6.1 | Introduction | 84 |
| 6.2 | Experimental model | 85 |
| 6.2.1 | Experimental setup | 85 |
| 6.2.2 | Experimental results | 88 |
| 6.2.3 | Discussion on experiment | 89 |
| 6.3 | Numerical model | 91 |
| 6.3.1 | Methods | 91 |
| 6.3.2 | Numerical results: REF material model | 93 |
| 6.3.3 | Numerical results: CPL material model | 95 |
| 6.4 | Discussion | 96 |
| 6.5 | Conclusions | 98 |
| 7 | Effects of constitutive modelling on brain response in a 3-D FE head model | 99 |
| 7.1 | Introduction | 100 |
| 7.2 | Numerical model | 100 |
| 7.3 | Results | 104 |
| 7.3.1 | Reference model: REF | 105 |
| 7.3.2 | Model variants: cpl and sof | 107 |
| 7.4 | Discussion | 110 |
| 7.4.1 | Numerical model accuracy | 110 |
| 7.4.2 | Reference model response | 110 |
| 7.4.3 | Variation of material models | 112 |
| 7.5 | Conclusions | 113 |
| 8 | Discussion, Conclusions and Recommendations | 115 |
| 8.1 | Introduction | 116 |
| 8.2 | Discussion | 116 |
| 8.2.1 | Requirements for the numerical accuracy of FE head models | 116 |
| 8.2.2 | Brain tissue constitutive behaviour: experiments and model | 117 |
| 8.2.3 | Application in a three-dimensional head model | 118 |
| 8.2.4 | Consequences for head modelling | 119 |
| 8.3 | Conclusions | 120 |
| 8.4 | Recommendations | 121 |
| 8.4.1 | Numerical quality, validation of head models | 121 |
| 8.4.2 | Constitutive modelling of brain tissue | 121 |
| 8.4.3 | Geometry and interface description in head models | 122 |
| | References | 123 |
| A | Test of numerical implementation | 133 |
| A.1 | Introduction | 134 |

| | | |
|----------|--|------------|
| A.2 | Simple shear stress relaxation | 134 |
| A.3 | Objectivity: uni-axial deformation | 137 |
| A.4 | Hydrostatic compression | 138 |
| A.5 | Combined shear and extension: cyclic loading and unloading | 139 |
| A.6 | Conclusions | 141 |
| B | Modification of non-linear viscoelastic material model | 143 |
| B.1 | Modification of the model | 144 |
| B.2 | Requirements for positive stiffness | 144 |
| B.3 | Determination of brain tissue material parameters | 145 |
| B.4 | Implications for material behaviour | 146 |
| B.5 | Discussion and conclusions | 147 |
| | Samenvatting | 149 |
| | Dankwoord | 153 |
| | Curriculum Vitae | 155 |

Summary

Annually, motor vehicle crashes world wide cause over a million fatalities and over a hundred million injuries. Of all body parts, the head is identified as the body region most frequently involved in life-threatening injury. To understand how the brain gets injured during an accident, the mechanical response of the contents of the head during impact has to be known. Since this response cannot be determined during an *in-vivo* experiment, numerical Finite Element (FE) modelling is often used to predict this response. Current FE head models contain a detailed geometrical description of anatomical components inside the head but lack accurate descriptions of the brain material behaviour and contact between e.g. skull and brain. Also, the numerical solution method used in current models (explicit Finite Element Method) does not provide accurate predictions of transient phenomena, such as wave propagation, in the nearly incompressible brain material.

The aim of this study is to contribute to the improvement of FE head models used to predict the mechanical response of the brain during a closed head impact. The topics of research are the accuracy requirements of explicit FEM for modelling the dynamic behaviour of brain tissue, and the development of a constitutive model for describing the nearly incompressible, non-linear viscoelastic behaviour of brain tissue in a FE model.

The accuracy requirements of the numerical method used depend on the type of mechanical response of the brain, wave propagation or a structural dynamics type of response. The impact conditions for which strain waves will propagate inside the brain have been estimated analytically using linear viscoelastic theory. It was found that shear waves (S-waves) can be expected during a traffic related impact, (frequencies between 25 and 300 Hz), while compressive waves (P-waves) are expected during short duration, high velocity, ballistic impacts (frequencies between 10 kHz and 3 MHz). For this reason FE head models should be capable of accurately replicating the wave front during wave propagation, which poses high numerical requirements.

An accuracy analysis, valid for one-dimensional linear viscoelastic material behaviour and small strains, revealed that modelling wave propagation phenomena with explicit FEM introduces two types of errors: numerical dispersion and spurious reflection. These errors are introduced by the spatial and temporal discretisation and cause the predicted wave propagation velocity to be lower than in reality. As a result, strain and strain rate levels will deviate from reality. Since both strain and strain

rate are associated with the occurrence of brain injury they should be predicted correctly. However, given the element size in current state of the art 3-D human head models, accurate modelling of wave propagation is impossible. For accurate modelling of S-waves the typical element size in head models (5 *mm*) should be decreased by a factor of ten which can be accomplished by mesh refinement. For accurate modelling of P-waves the typical element size should be decreased by a factor of hundred. For this reason mesh refinement is not feasible anymore and developments on spatial and temporal discretisation methods used in the Finite Element Method are recommended. As these developments are beyond the scope of this research, shear behaviour is emphasised in the remainder of the study.

The mechanical behaviour of brain tissue has been characterised using simple shear experiments. The small strain behaviour of brain tissue is investigated using an oscillatory strain (amplitude 1%). Frequencies relevant for impact (1-1000 *Hz*) could be obtained using the Time/Temperature Superposition principle. Strains associated with the occurrence of injury (20% simple shear) were applied in stress relaxation experiments. It was found that brain tissue behaves as a non-linear viscoelastic material. Shear softening (i.e. decrease in stiffness) appeared for strains above 1% (approximately 35% softening for shear strains up to 20%) while the time relaxation behaviour was nearly strain independent.

A constitutive description capable of capturing the material behaviour observed in the material experiments was developed. The model is a non-linear extension of a linear multi-mode Maxwell model. It utilises a multiplicative decomposition of the deformation gradient tensor into an elastic and an inelastic part. The inelastic, time dependent behaviour is modelled using a simple Newtonian law acting on the deviatoric part of the stress only. The elastic, strain dependent behaviour is modelled by a hyper-elastic, second order Mooney-Rivlin material formulation. Although isotropy was assumed in this study, the model formulation is such that implementing anisotropy, present in certain regions of the brain, is possible. Brain tissue material parameters were obtained from small strain oscillatory experiments and the constant strain part from the stress relaxation experiments.

The constitutive model was implemented in an existing explicit FE code (MADYMO). In view of the nearly incompressible behaviour of brain tissue, Heun's (predictor-corrector) integration method was applied for obtaining sufficient numerical accuracy of the model at time steps common for head impact simulations. As a first test, the initial part of the stress relaxation experiments, which was not used for fitting the material parameters, was simulated and could be reproduced successfully.

To test both the numerical accuracy of explicit FEM and the constitutive model formulation at conditions resembling a traffic related impact a physical (i.e. laboratory) head model has been developed. A silicone gel (Dow Corning Sylgard 527 A&B) was used to mimic the dynamical behaviour of brain tissue. The gel was mechanically characterized in the same manner as brain tissue. It was found that silicone gel behaves as a linear viscoelastic solid for all strains tested (up to 50%). Its material parameters are in the same range as the small strain parameters of brain tissue, but viscous damping at high frequencies is more pronounced. It was concluded that for trend studies and benchmarking of numerical models the gel is

a good model material. The gel was put in a cylindrical cup that was subjected to a transient rotational acceleration. Gel deformation was recorded using high speed video marker tracking. The gel was modelled using the new constitutive law and the physical model experiments were simulated. Good agreement was obtained with experimental results indicating the model to be suitable for modelling the nearly incompressible silicone gel. It was shown that correct decoupling of hydrostatic and deviatoric deformation in the stress formulation is necessary for correct prediction of the response of the nearly incompressible material.

Finally, the constitutive model was applied in an existing 3-D FE model of the human head to assess the effect of non-linear brain tissue material behaviour on the response. The external mechanical load on the 3-D FE head model (an eccentric rotation) was chosen such as to obtain strains within the validity range of the material experiments (20% shear strain). This resulted in external loading levels values below the ones associated with injury in literature. A possible explanation for this is the fact that shear stiffness values, commonly used in head models in literature, are too high in comparison with material data found in recent literature and own experiments. Also the estimated injury threshold of 20% strain, indicated by studies on isolated axons, might be too conservative. Another possible explanation may be that a certain degree of coupling between hydrostatic and deviatoric parts of the deformation in the stress formulation might exist in reality which is not modelled in current constitutive formulation.

Application of the non-linear behaviour in the model influences the level of stresses (decrease by 11%) and strains (increase by 21%) in the brain but not the temporal and spatial distribution. However, it should be noted that these effects on stresses and strains hold for one specific loading condition in one specific model only. For a more general conclusion on the effects of non-linear modelling in brain tissue, application in different models is recommended.

Chapter 1

General introduction

A general introduction in the field of injury biomechanics is provided. First epidemiology and the importance of head injury biomechanics is presented. To facilitate a discussion on the development of head injuries during impact basic anatomy of the head is presented. Furthermore, the events during an impact are classified as a mechanical part which leads to an internal mechanical response of the brain inside the head and a subsequent part which involves the development of injury, the injury mechanism. This classification is used to point out the limitations of existing head injury criteria and to discuss the various types of head models used for improving insight in the relation between a load on the head and the resulting injury. The present study focuses on gaining insight in the internal mechanical response. Finite Element (FE) models are found to be a powerful tool to investigate the mechanical response of the head. When used in combination with biological or physical models they can provide insight into which mechanical quantities are responsible for the occurrence of injury. If this knowledge is established they even can predict the occurrence of injury. The status of FE head modelling is reviewed in a separate section paying attention to geometry, constitutive behaviour, interface conditions between various structures inside the head, numerical solution methods and experimental validation. The scope of the present research, presented in the final section, is on the improvement of FE models, in particular on constitutive modelling of brain tissue and on numerical artefacts present in the predictions of current FE head models.

1.1 Introduction to head injury biomechanics

1.1.1 Epidemiology of head injury

Annually, motor vehicle crashes worldwide cause over a million fatalities and over a hundred million injuries. In 1998, traffic accidents were the leading cause of death for the age groups of 1 to 34 years in the United States [163]. Focusing on the European Union (EU) countries only, there were about 45000 reported fatalities and 1.5 million casualties in 1995 [47]. The socio-economic costs (the pure economic costs plus the value of lost human lives and seriously injured persons) of traffic accidents in the EU for 1999 were estimated to exceed 160 billion Euro [48].

Of all body parts, the head is identified as the body region most frequently involved in life-threatening injury in crash situations [46]. In the United States, 2 million cases of *traumatic brain injury* (TBI) were recorded in 1990, 51600 of which resulted in fatal outcome [160]. Despite development of injury protection measures (belts, air bags, helmets), and increase of governmental regulations, traffic accidents were still responsible for about 40% of all TBI cases in the United Kingdom in 1997 [157]. Furthermore, about one third of the hospitalized victims suffered from permanent disability [31; 158]. As a result, TBI due to crash impacts provide a high contribution to societal costs [32; 166]. For prevention of head injuries, the mechanism how an impact on the head leads to injury has to be understood. This is the subject of study in the field of *head injury biomechanics*.

1.1.2 Basic anatomy of the head

To ease the discussion on the mechanics of head injuries, the relevant aspects of the anatomy of the head are presented here. The head consists of a *facial area* and the *cranial skull* surrounded by the *scalp*. The *face* is not of interest in this study and will not be discussed. The outer surface of the head is covered by the *scalp*, which is a soft tissue layer with a thickness of about 5 to 7 *mm*. Underneath, the cranial skull, or *neuro cranium*, is present. It is the part of the skull that covers the brain. Further

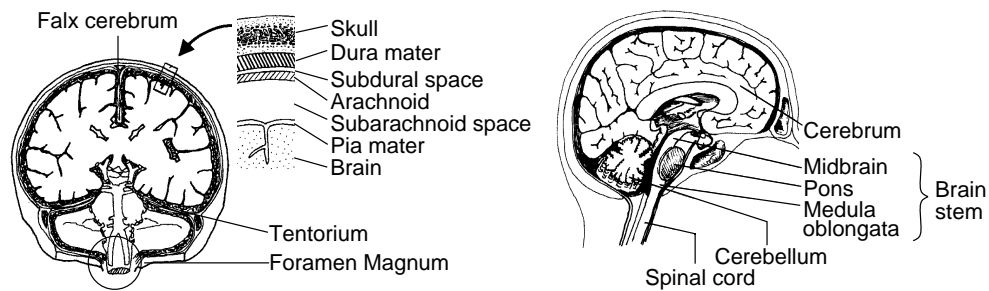


Figure 1.1: Overview of important anatomical components of the head. based on [121]. Left: Coronal section of the meninges of the brain. Right: Principal parts of the brain in sagittal section.

inwards, three membranes are present that surround the brain: the *meninges*. From outside to the inside these are: the *dura mater*, the *arachnoid* and the *pia mater* (refer to Figure 1.1). These meninges are separated from each other by *subdural* and *subarachnoidal* spaces respectively. These spaces contain water-like liquid, the *cerebrospinal fluid* (CSF). It is believed that this fluid plays an important role in the shock absorbing capacities of the head. Blood vessels called *bridging veins*, cross the meninges. The brain itself, consists largely of a network of nerve cells, *neurons* and supportive cells, *glia*. These are functionally arranged into areas that are gray or white in color. *Gray matter* is composed primarily of nerve cell bodies (*neurons*) while *white matter* is composed of myelinated nerve cell processes (*axons*). Also blood vessels are present inside the brain tissue. The brain is structurally separated in several parts. The most important ones are, the *cerebrum*, the *cerebellum*, and the *brain stem* which consists of *midbrain*, *pons* and *medulla oblongata*. It connects the brain to the *spinal cord* via an opening in the skull called *foramen magnum* (see Figure 1.1). The cerebrum and cerebellum are divided in left and right *hemispheres* by *falx cerebri* and the *falx cerebelli* respectively. These are invaginations of the *dura mater*. A similar invagination, the *tentorium*, separates cerebrum and cerebellum. Also CSF filled cavities are present in various parts of the brain, the *ventricles*.

1.1.3 Load-injury scheme

The processes leading to head injury during an accident are shown schematically in Figure 1.2. The mechanical load applied on the head during an accident is called the *external mechanical load*. The nature of this load acting on the head itself can be influenced by the application of injury prevention measures such as helmets and airbags. The external mechanical load can be a *contact load* by an object hitting the head or a *non-contact* (inertial) load, transferred to the head via the neck (acceleration). Depending whether the object hit penetrates the head or not, contact loads can be categorised as *penetrating impact* and *non-penetrating* (or *blunt*) impact. This research will focus on *closed head impacts*, i.e. transient loading due to

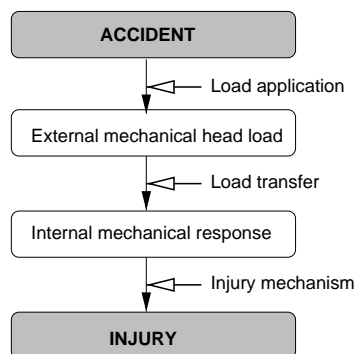


Figure 1.2: Load-injury scheme showing stages from accident to head injury. Labels on the right indicate mechanisms between stages.

non-penetrating impacts or inertial loading. The external mechanical load causes an *internal mechanical response* of the various anatomical components of the head which can be expressed in local quantities such as stresses and strains. When the internal mechanical response exceeds an *injury tolerance level* of an anatomical component, injury to this component occurs via an *injury mechanism* (i.e. the sequence of physiological changes leading to injury due to a mechanical stimulus). Different parts of the head may be injured through a variety of different injury mechanisms.

This research will focus on *traumatic brain injury* (TBI). The internal mechanical response of the brain is a key quantity for understanding the transformation of the external mechanical load to injury. It originates from the external mechanical load that is transferred from the scalp to the brain tissue via the skull and an interface consisting of meninges and CSF. The internal mechanical response is influenced by magnitude and time duration of the external mechanical load. The magnitude of the external mechanical load has to be such that stresses and/or strains associated with injury do occur inside the brain tissue. This means that certain tolerance levels have to be exceeded. The duration of an impact determines the nature of the strain field in the brain. Short duration impacts are defined here as impacts in which the characteristic loading time is on the order of the characteristic time period of the head system (determined by the eigenfrequencies). They occur when a projectile with low mass (e.g. a bullet) hits (the protected) head at high velocity. These will also be called *ballistic impacts*. The internal mechanical response of the brain then is dominated by *wave propagation*. This means that a wave front that consists of a large stress or strain gradient propagates in the brain tissue. The behaviour of the strain or stress field at the wave front is important. The propagation of stress waves inside brain tissue has, since long, been hypothesised to be of importance in the internal mechanical response [54; 59; 62; 114; 115] but, to this authors knowledge, it has never clearly been pointed out under which circumstances wave propagation is likely to be present in the internal mechanical response. When the head hits a heavy object with lower velocity, a longer duration impact occurs. The internal mechanical response then is called of *structural dynamics* type. Wave fronts propagating as such cannot be distinguished anymore, instead the response will be more of a low gradient type. At even slower loading conditions a *quasi-static* response will occur in which inertia effects can be neglected. However, this type of response is not relevant for impact conditions.

1.1.4 Head injury criteria

To assess the risk of sustaining a head injury, and to assess the effectiveness of potential protection measures, an *injury criterion* is needed (i.e. a physical parameter which correlates well with injury severity of the body part in question [115]). The first extensive quantification of head tolerance to impact is the Wayne State Tolerance Curve (WSTC) [66; 67; 85]. The WSTC shows that, in linear acceleration loading, the risk of brain damage due to non-penetrating impacts is determined by both the magnitude and the duration of the acceleration pulse. Short duration, high acceleration impacts (2 ms and 400 g respectively) lead to similar injury risk as

long duration, low acceleration impacts (30 *ms* and 80 *g* respectively). The curve is developed using a combination of linear skull fracture data in (embalmed) cadaver heads (short duration impacts), brain concussion data in animal heads (medium duration impacts) and, non injury producing, low acceleration, volunteer data. The later is considered as asymptotic value of the curve for long impact durations. The validity of the curve was confirmed through a series of experiments on subhuman primates by Ono *et al.* [116]. The WSTC served as the basis for the injury criterion currently used in automotive impact regulations, the *Head Injury Criterion* (HIC), It is defined as [155],

$$\text{HIC} = \left\{ (t_2 - t_1) \left(\frac{1}{t_2 - t_1} \int_{t_1}^{t_2} a(t) dt \right)^{2.5} \right\}_{\max} \quad (1.1)$$

in which $a(t)$ is the resultant translational head acceleration and t_1 and t_2 the, varying, initial and final times of the interval during which HIC attains a maximum value. For regulations the maximum interval $t_2 - t_1$ is set to 15 or 36 *ms* [42]. For cadaver data in frontal impact, HIC has been shown to be a reasonable discriminator between severe and less severe injury [140]. It also correlates with the risk for cranial fracture in cadavers after impact [124]. However, for impacts in various directions, bad correlation between HIC and injury severity has been found [107]. An important drawback of HIC is that head rotation is not taken into account although rotation is debated to be the primary cause for various types of traumatic brain injury [2; 60; 70]. Head injury criteria including head rotation also were proposed but never extensively validated (e.g. GAMBIT in [108] and HIP in [109]).

The injury criteria presented so far predict injury risk from the external mechanical load on the head, which can be measured directly from a crash dummy head, but do not take into account the internal mechanical response. Furthermore, they do not discriminate between various types of traumatic brain injury, such as such as *subdural hematoma* (SDH, disruption of the bridging veins between skull and brain), *blood brain barrier breakdown*, (BBB, (temporary) breakdown of blood vessels within the brain) or *diffuse axonal injury* (DAI, neural damage involving prolonged loss of consciousness).

Recent research focuses on so called next-generation injury assessment tools that use computational head models. A more detailed injury prediction is obtained using a computed internal mechanical response resulting from dummy-measured external mechanical loading [15]. An example of such injury assessment tool is SIMon, a simulated injury monitor, recently proposed by Bandak *et al.* [15]. It includes a simple Finite Element model of the head originally developed in [12; 40]. It addresses both the load transfer from external mechanical load on the head to internal mechanical response and prediction of the risk of injury using tissue level injury tolerances. However, these tolerance levels and the underlying injury mechanisms are not yet well established and need additional research. The various types of head models used in head injury research will be discussed in more detail in next section.

1.1.5 Head models

Head models are often used in approval tests for cars and helmets. Moreover they can be used for research on the internal mechanical response and injury mechanisms. In the subsequent section head models used in research will be emphasised. These can be divided in three categories: *biological models*, *physical models* and *numerical models*. For each model category advantages and disadvantages in terms of mechanical accessibility (to what extent can the internal mechanical response be measured), injury information (does the model provide information on how injury occurs), and biofidelity (how realistic is the model for modelling the human head) will be discussed.

Biological models For the purpose of this study the following four types of biological models are distinguished: *in-vivo human models*, *animal models*, *human cadavers* and *tissue level models*. The first three types of models, the so called *whole head biological models* in Figure 1.2, in principle allow the investigation of the internal mechanical response after impact. However, capturing this response is complicated due to the inaccessibility of the brain in the cranial cavity. The experiments needed to exercise biological models are complicated by precautions needed when working with *in-vivo* models or for keeping *in-vitro* models fresh. Furthermore, ethical aspects have to be considered when using a biological model.

In-vivo human models provide maximum biofidelity. However their use is severely limited since external head loading has to be applied below the injury range [161]. Victims in accidents can constitute as a source of *in-vivo* human data within the injury range however the external mechanical loading history during such accident is not available. For this reason the external mechanical load on the head of the victim is reconstructed using data found on the site of the accident. Subsequently, the internal mechanical response of the head is reconstructed using Finite Element modelling. Finally, this response is correlated to the physical injury sustained, visualised using MRI scanning or CT scanning, or to functional injuries, determined using cognitive investigation methods. A disadvantage of this method is that the accuracy of the reconstruction method is low due to many uncertainties encountered in the reconstruction process of the mechanical response [154].

Animal models enable extension of the external mechanical load into the injury range. They are subjected to a well prescribed external mechanical load after which the resulting injury is investigated [60; 98; 99; 100; 131]. In this manner a relation between external mechanical load and injury sustained can be obtained. In early studies, a qualitative idea of the internal mechanical response was obtained using invasive methods such as the cranial window [64; 65; 133]. More recently, the use of the non-invasive MRI tagging method is investigated [43]. Also Finite Element modelling of the animal head is used to reconstruct the internal response [99; 131; 152]. Exact translation of external mechanical loading from animal data

to human values is generally impossible due to geometry differences in combination with viscoelastic material behaviour of the brain tissue.

Human cadaver models also allow experiments within the injury range. Detailed information on the topology of the resulting injuries can be gained from dissection after the impact experiments. Some information on the internal mechanical response has been obtained using intracranial pressure measurements [104; 150], intracranial miniature accelerometers [68; 150] or by high speed x-ray marker tracking techniques [3]. However, these methods are always invasive. Furthermore it is unknown how postmortem changes influence the mechanical response measured.

Tissue level biological models are living tissue specimens on which mechanical experiments are performed [10; 56; 141]. A load is applied on for example an isolated axon and physiological changes in terms of resting potential (depolarization) are determined [56]. Since these models are not exercised *in situ* (i.e. not inside the head), they are not suited for prediction of internal mechanical response. However, tissue level injury tolerance levels can be obtained. Apart from potential differences between animal and human tissue characteristics the biofidelity is good.

Physical head models are widely used in the evaluation of protective measures. Most well known are the rigid crash dummy heads and head impactors, used in approval tests for cars and helmets. The resultant acceleration history of the head is measured and HIC is determined. Head models that include some anatomical structures such as the brain, can provide insight into the internal mechanical response of the head at impact loading. The most simplified method is to model the contents of the head as lumped masses connected by a damped spring system [162]. Other models include deformable brain tissue mimicking materials such as water [73], oil [69] or silicone gel [24; 71; 90; 157]. A more complete overview of physical models can be found in Bradshaw *et al.* [24].

It is relatively easy to perform experiments with physical models. Furthermore, models with deformable brain tissue materials can provide validation data for numerical head models since model properties are well defined. However, differences between the models and the real head prevent quantitative derivation of tissue level tolerance levels. Furthermore, it is unknown to which extent the mechanical behaviour of the model materials used resembles the real head material behaviour.

Numerical head models commonly used for gaining insight in the internal mechanical response of the head in terms of field parameters such as stresses and strains, are Finite Element Models (FEM) [11; 36; 37; 40; 72; 94; 126; 127; 136; 150; 151; 167; 168; 169]. Numerical models, in principle, can offer a good biofidelity when thoroughly validated. However validation of such model is not trivial and has been a topic of research for many years. When a validated model is established it is easy to exercise it in different impact situations. Furthermore these models can also serve as a tool for development of injury prevention measures.

It can be concluded that biological models can provide data on injury sustained due to some external mechanical load, but provide only minor information on internal mechanical response. This is due to mechanical inaccessibility. FE models and physical models can be used for obtaining information on the internal mechanical response of brain tissue during an impact but do not allow for prediction of injury without prior assumptions about tissue level injury tolerance levels. This means that for obtaining insight in the complete pathway between external mechanical load on the head and TBI a combination of head models and research methods has to be used. An example of this is to use a biological model (animal or cadaver) to provide data on external mechanical load and injury sustained, while the internal response is reconstructed using numerical or physical models. By comparing the internal response obtained from numerical or physical models with histological data on injury locations in the head of a biological model, insight can be gained in tissue tolerance levels in terms of stress and strain quantities.

Table 1.1 provides an overview of the various research techniques for assessment of tissue tolerance levels, as well as potential stress and strain candidates for prediction of injury. It can be seen that tissue tolerance levels are formulated in virtually all strain and stress measures. Von Mises stress (VMS) and maximum principal strains (MPS) showed statistical correlation with the occurrence of DAI. MPS also could be associated with BBB. Pressure has been proposed as an injury criterion especially in relation with cavitation in the CSF layer due to negative pressures at the contre-coup site of an impact, but research on the validity of this theory is ongoing [112]. Bandak and co-workers developed a *cumulative damage strain measure* (CDSM). It is based on the assumption that DAI can be associated with the cumulative volume of the brain matter experiencing tensile strains over a critical level sometime during impact [11]. This tensile strain is represented by the maximum principal strain in the criterion. A similar measure based on negative pressure, the *dilatation damage measure* (DDM) was proposed in [13]. The application of these criteria implies the use of a FE model to predict the internal mechanical response.

Table 1.1: Overview of stress/strain quantities associated with injury by various authors. NUM: Numerical study only, no direct correlation, PHY: Physical model study only, TLB: Tissue level biological models, NCA: Animal models combined with numerical model, PCA: Physical model combined with animal experiments.

| Method | Max shear strain | Max. Principal strain | Von Mises stress | Pressure |
|--------|--------------------|--------------------------|------------------|--------------------|
| NUM | [35; 70; 150; 167] | [11] | | [14; 33; 165; 167] |
| PHY | [157] | | | [14; 63; 111; 157] |
| TLB | | [9; 10]*,[141]* | | |
| NCA | [152] | [99]*,[131] ⁺ | [99]*,[131; 152] | |
| PCA | [90; 92] | | | |

* Statistical correlation with Diffuse Axonal Injury.

⁺ Statistical correlation with Blood Brain Barrier damage.

1.2 Finite Element modelling of head impact

In the previous section two stages were distinguished in the pathway from external mechanical load on the head to brain injury during an accident: the development of the internal mechanical response and the development of TBI when this internal mechanical response exceeds tissue level tolerance levels. For this reason it is expected that insight in the internal mechanical response of the head will lead to improved understanding of the subsequent injury mechanisms causing certain types of injury. In this study Finite Element (FE) head modelling will be used for obtaining insight in the internal mechanical brain response.

The use of FE techniques for modelling the head started in the early seventies of the last century. FE head models that have been developed from 1971 until 1998 are reviewed in literature in [74; 130; 154]. A FE head model basically consist of a set differential equations, the mathematical model, that is solved numerically using the Finite Element Method. To create the mathematical model, assumptions for the geometry, material behaviour and interface conditions between of the various substructures of the head have to be made. These assumptions present in current FE head models are reviewed in section 1.2.1. When solving the resulting equations, numerical artefacts are introduced by the FE method used. For this reason the numerical solution method typically used for these models will be discussed next. Finally the methodology used for validating these complex models is discussed in section 1.2.3.

1.2.1 Mathematical model

Geometry modelling In the first FE models, the skull-brain system was usually approximated by a two or three-dimensional spherical or elliptical fluid filled shell [74]. With the advancement of imaging techniques such as for example Computed Tomography scanning (CT) and Magnetic Resonance Imaging (MRI) an increasing amount of geometrical data has become available in digital format. With the additional increase of CPU power, this resulted in an increase in geometric complexity in FE models, leading to three-dimensional models with many anatomical details (e.g. [36; 37; 40; 72; 94; 126; 127; 167; 168; 169]). Also, two-dimensional models with even higher geometrical detail (including temporal lobes and sulci (folds) at brain surface) have been presented recently [99; 100; 110].

Interface modelling Interfaces exist between the various structures within the cranial cavity. Experiments show that relative motion occurs between the various brain parts during impact [3; 132]. This is especially true for the skull and brain separated by meninges and CSF. Until now, modeling each of these structures individually has been infeasible, amongst others because of the problems associated with the combination of solid and fluid behaviour in one model. Instead, interface mechanical behaviour is modelled with a certain degree of suppression of the relative tangential and normal motion of skull and brain. For the tangential motion, descriptions range from no slip via different friction levels to frictionless motion

[37; 99]. Some models use a failure criterion, above which skull and brain can separate [40; 41]. Other models approximate the interface by a layer of soft, easily deformable elements [72; 99; 167].

Modelling of brain tissue material behaviour It has been shown experimentally that brain tissue exhibits non-linear, time dependent material behaviour [4; 44; 120]. Regional differences in material behaviour are present [5; 123]. Furthermore, fibrous parts of the brain show anisotropy (brainstem [8], corpus callosum [123]). The bulk modulus of brain tissue is about 10^6 times higher than the shear modulus, indicating nearly incompressible material behaviour [45; 61; 83; 84].

Most FE head models to date assume isotropic linear viscoelastic material behaviour for brain tissue. Regional differences in brain material behaviour have been incorporated in some models in that grey and white matter were modelled using different material parameters [3; 99; 167; 168]. Physical model simulation results show that deformations occurring in the brain exceed the validity range of infinitesimal strain theory [24; 141]. Also the nearly incompressible material behaviour puts special demands on the constitutive formulations used. It is not obvious whether correct large strain formulations have been used in every FE head model reported [113].

Application of non-linear material models for modelling impact in 3-D human head FE models has not been found in literature. Application in a 2-D animal FE model was found but no comparison with linear models was presented [99; 100]. Low velocity indenter animal experiments have been simulated using a 3-D animal FE model in [98]. The material models used in these studies all were based on hyperelastic Strain Energy Density functions (SED) expressed in strain invariants (Green elastic materials). First- [95; 118] and second-order [96; 97] versions of the Mooney-Rivlin SED (original by Mooney [101]) are used as well as a first-order Ogden, or Seth [137] SED. Viscoelastic behaviour is modelled by making the constants in the SED time dependent using a Prony series, akin to the definition of the stress relaxation function in linear viscoelastic theory (quasi-linear theory [53]). As such, the time dependent behaviour is independent of the strain applied.

The material parameters for the Ogden variant have been fitted to large deformation shear tests and have been checked for unconfined compression behaviour and reasonable agreement has been found [123]. The Mooney-Rivlin based models are fitted on results of unconfined compression experiments found in [44; 57; 96]. No check on the simple shear behaviour has been reported.

1.2.2 Numerical solution method

The accuracy of the numerical solution depends on spatial and temporal discretisation used by the Finite Element Method. The requirements for the discretisation used are determined by the type of internal mechanical response to be expected at certain types of impact. When a wave propagation response is expected, numerical requirements to accurately replicate the wave front are higher than when a structural dynamic type of response is expected. The numerical accuracy is almost never treated in references

found on head modelling. However, they have been shown to have a significant effect on simulation results in a FE code commonly used for head modelling [113].

1.2.3 Model validation

To assess the quality of FE head models, usually the computed brain response is compared with experimental results obtained from cadaver experiments. In doing so, two problems are encountered. Firstly the suitability of the data set used for complete model validation. Apart from post-mortem effects, the suitability of the experimental results is influenced by limited spatial resolution and invasive techniques used to obtain quantitative data. This will be illustrated with some examples. Most commonly used for model validation (e.g. in [37; 72; 128; 168]) are pressure histories measured at four points in the CSF-layer of a cadaver subjected to frontal impact by Nahum *et al.* [104]. Apart from effects discussed before another drawback is that shear effects inside the brain are not represented in the experimental pressure data used. Al-Bsharat *et al.* [3] simulated low speed occipital impact and compared relative skull-brain displacements with three-dimensional x-ray marker trajectories determined in a cadaver. Although the primary objective of this study was to gain insight in the skull-brain interface, this data set also can be used for providing insight in the shear behaviour. Turquier *et al.* [151] used intra-cranial acceleration as well as epi-dural and ventricular pressure signals obtained from cadaver experiments in [150]. They found qualitative agreement with experimental data but also found oscillations in their response which they attributed to numerical artefacts. This raises a second limitation of this type of validation methods. Even if these datasets would contain sufficient information to completely validate a FE model, there is still a methodological problem in that the identification of the origin of discrepancies between model and experimental results is difficult since errors can be introduced by the experimental method, mathematical model assumptions or the numerical solution procedure.

Physical models which include a deformable brain structure can be used as a tool to assess the quality of the numerical solution method separately. Such experimental model can be designed to minimise the number of mathematical modelling assumptions while maximising mechanical accessibility. This can be achieved by using a known, simplified geometry, materials with known material properties, using transparent components for optical measurement techniques, etc. When confidence in the numerical method is gained in this manner, the recommendations obtained from this method can be applied in a complete head model, thus reducing effects of numerical artefacts in the solution method. However, references found in literature which compare numerical model results with physical model results, only focus on determining the effects of interface modelling at the skull-brain interface and not on numerical accuracy [34; 55; 149].

1.2.4 Conclusion

It can be concluded that current state of the art head FE models contain detailed geometrical description of anatomical components inside the head but lack accurate descriptions of non-linear brain material behaviour and interfaces inside the head. Furthermore it is not obvious to which extent numerical artefacts influence the responses obtained especially when a wave propagation response is expected. Current model validation methods involve complete biological head models. Although this provides maximum biofidelity, the method lacks the capability of distinguishing between sources of discrepancies between model and experiment results, e.g experimental errors, mathematical model assumptions and the numerical solution procedure artefacts. Physical models can be a valuable tool to obtain more insight in the presence of numerical artefacts as they can be designed such as to minimise the number of modelling assumptions and maximising mechanical accessibility.

1.3 Scope of study

It has been shown that the development of TBI during an impact on the head consists of two stages. In the first stage the external mechanical load on the head is transferred into the head and causes the internal mechanical response of the brain inside the head. The second stage consists of the development of traumatic brain injury via an injury mechanism. The present research focuses on the first stage: the determination of the internal mechanical response of brain tissue. This will be done using Finite Element models. Important aspects of these models are: geometry, constitutive models, interface conditions between of the various intracranial substructures and numerical accuracy. The focus in this study will be on constitutive modelling of brain tissue and on the accuracy of the solution method.

1.3.1 Objectives

The aim of this study is to contribute to the improvement of FE head models used to predict the mechanical response of the brain during a closed head impact. More specifically the objectives are:

- to investigate the accuracy of numerical methods commonly used for predicting brain response (explicit FEM) in crash impact, especially in relation to wave propagation
- to develop a constitutive model for describing the nearly incompressible, non-linear viscoelastic behaviour of brain tissue in a Finite Element model,
- to assess the effects of non-linear material behaviour on the internal mechanical response by applying the constitutive model in a 3-D Finite Element model, and
- to discuss the consequences of this research for current state of the art head modelling.

It has to be noted that developments on spatial and temporal discretisation methods used in the Finite Element Method are not a topic of this research.

1.3.2 Strategy

Numerical accuracy As the numerical requirements for predicting a wave propagation response are higher than for a structural dynamics response, it will be estimated when wave propagation inside brain tissue is likely to occur. This will be done using small strain linear viscoelastic theory. The accuracy of current explicit Finite Element Models then will be treated in terms of a wave propagation problem. It will be shown that if wave propagation is predicted correctly, lower frequency (structural dynamic) response is also predicted correctly. Accuracy requirements will be developed using a simple one dimensional wave propagation problem. The capability of current head models to predict a wave propagation response accurately will be estimated. Recommendations are given on required temporal and spatial discretisation needed for accurate modelling of wave propagation.

The validity of these recommendations at large strains cannot be tested using analytical solutions anymore. For this reason, a simple physical head model is developed that mimics the brain behaviour during a traffic related impact. In this model geometry and boundary conditions are known. The material behaviour of the brain tissue mimicking material is mechanically characterised. In this manner, uncertainties in the mathematical model are eliminated as much as possible, leaving differences between numerical model and experimental results to be caused by numerical artefacts.

Constitutive modelling The constitutive behaviour of brain tissue is characterised using shear experiments in a strain and frequency range representative for traffic related impacts. This provides data on the non-linear viscoelastic behaviour of brain tissue. This data is used for the development of a constitutive model suitable for large deformations and rotations. The constitutive model is implemented in an existing explicit Finite Element code commonly used for crash impact simulations [148]. The accuracy of the model in predicting the large strain response of nearly incompressible materials such as brain tissue is tested using the simple physical model.

Application The non-linear viscoelastic material model is applied in an existing 3-D FE model of the human head in order to assess the effect of non-linear brain tissue material behaviour on the computed response. The quality of the response calculated will be discussed using the knowledge on numerical accuracy obtained before.

1.3.3 Outline of the thesis

Chapter 2 contains the investigation on the presence and accurate modelling of wave propagation inside brain tissue. Chapters 3 and 4 deal with the mechanical characterisation of brain tissue as well as the material for mimicking the brain

tissue in the physical model. First a comparison for small strains (1%) but realistic frequencies (1-1000 Hz) is presented in Chapter 3. Then the comparison is extended to large strains (up to 20% and 50% for brain tissue and model material respectively) in Chapter 4. In Chapter 5 a non-linear viscoelastic material model will be developed and brain tissue material parameters will be fitted to the experimental data. Chapter 6 contains the experimental and numerical results of the physical model experiments which serve for the investigation to numerical artefacts at large strains as well as for testing the newly developed material model. The material model with non-linear brain tissue material parameters will be applied in a three-dimensional Finite Element Model of the head in Chapter 7. Finally the result of this study will be discussed in Chapter 8.

Chapter 2

Numerical accuracy: analysis of wave propagation in blunt head impact

The numerical accuracy of the explicit finite element method (explicit FEM), commonly used for modelling the internal mechanical response of the human head during impact, is treated in terms of a wave propagation problem. First the conditions for strain waves to propagate inside the head have been estimated. It was found that, due to the nearly incompressible, viscoelastic nature of brain tissue, dilatational (P) waves and distortional (S) waves exist at different frequency ranges. S-waves can be expected during a traffic related impact, with frequencies between 25 and 300 Hz, while P-waves are expected during ballistic impacts with frequency between 10 kHz and 3 MHz. Therefore, wave propagation inside brain tissue should be considered a real possibility and FE head models should provide an accurate replication of it. When modelling wave propagation phenomena with explicit FEM, two types of errors occur: numerical dispersion and spurious reflection. The first error is influenced by the mesh density applied while the latter error is influenced by mesh inhomogeneities. An analysis with P-waves yielded the rule of thumb that for modelling wave propagation correctly, at least 24 elements per maximum wavelength should be used (error in strain rate less than 2.5%). Theory indicates that this rule also holds for S-waves. Considering the mesh density used in current state of the art 3-D human FE head models, accurate modelling of wave propagation is impossible. For modelling S-waves mesh refinement in current explicit FEM is an option. For modelling P-waves changes in spatial discretisation are recommended.

2.1 Introduction

As explained in Chapter 1, FE models are an important tool for assessment of the internal mechanical response. A FE head model basically consist of a set differential equations, the mathematical model, that is solved numerically using the Finite Element Method. In this Chapter, numerical artefacts, introduced by the FE method during solving of the mathematical model equations, are investigated. Only FE methods commonly used for head impact modelling (so called explicit FEM) will be considered in this Chapter.

The internal mechanical response of the head may be either of wave propagation nature or of structural dynamics nature, depending on the type of impact subjected to the head. The modelling requirements for wave phenomena are higher than for modelling a structural dynamics response. For this reason a wave propagation problem will be used to estimate the accuracy of the explicit FEM.

The outline of this Chapter is as follows. First, elementary theory on wave propagation is presented. It is used to investigate the impact conditions for which wave propagation inside brain tissue is likely to occur in section 2.3. Section 2.4 contains an analytical investigation of numerical errors introduced by the explicit FEM. This theory is checked numerically by simulation of wave propagation in a 1-D beam in section 2.5. Section 2.6 contains a discussion on: the likelihood of wave propagation inside the brain due to impact type, implications for the modelling accuracy in existing head models and potential improvements. Conclusions are shown in section 2.7.

2.2 Elementary theory on wave propagation

Biological tissues, including brain tissue, behave like viscoelastic solids. It will be assumed that elementary wave theory in semi-infinite, isotropic, linear viscoelastic media can be used for the analysis in this Chapter. The theory presented is based on [19].

2.2.1 Elastic wave equation

In absence of body forces the three-dimensional equations of motion in a continuum are given by,

$$\vec{\nabla} \cdot \boldsymbol{\sigma} = \rho \frac{\partial^2 \vec{u}}{\partial t^2} \quad (2.1)$$

where ρ is the mass density of the material, $\vec{\nabla} \cdot \boldsymbol{\sigma}$ the divergence of the symmetric Cauchy stress tensor, t the time, and \vec{u} the displacement vector. The linear strain, $\boldsymbol{\varepsilon}$, is defined as,

$$\boldsymbol{\varepsilon} = \frac{1}{2} \left(\left(\vec{\nabla} \vec{u} \right)^c + \left(\vec{\nabla} \vec{u} \right) \right) \quad (2.2)$$

in which superscript c denotes the conjugate of a tensor. Linear elastic material behaviour is described by Hooke's law,

$$\boldsymbol{\sigma} = \lambda_L \text{trace}(\boldsymbol{\varepsilon}) \mathbf{I} + 2\mu_L \boldsymbol{\varepsilon} \quad (2.3)$$

in which λ_L and μ_L are the Lamé parameters for the material. Substitution of Hooke's law into equation (2.1) gives the Navier equations for the medium,

$$(\lambda_L + \mu_L) \vec{\nabla} \left(\vec{\nabla} \cdot \vec{u} \right) + \mu_L \nabla^2 \vec{u} = \rho \frac{\partial^2 \vec{u}}{\partial t^2} \quad (2.4)$$

in which $\nabla^2 \equiv \vec{\nabla} \cdot \vec{\nabla}$. By applying the vector identity,

$$\nabla^2 \vec{u} = \vec{\nabla} \left(\vec{\nabla} \cdot \vec{u} \right) - \vec{\nabla} \times \left(\vec{\nabla} \times \vec{u} \right) \quad (2.5)$$

and introducing both dilatation $\Delta = \vec{\nabla} \cdot \vec{u}$, which represents the change in volume of the material, and rotation $\vec{\omega} = \frac{1}{2} \left(\vec{\nabla} \times \vec{u} \right)$ [76], equation (2.4) can be rewritten as,

$$(\lambda_L + 2\mu_L) \vec{\nabla} \Delta - 2\mu_L \vec{\nabla} \times \vec{\omega} = \rho \frac{\partial^2 \vec{u}}{\partial t^2} \quad (2.6)$$

Equation (2.6) is the three-dimensional wave equation for unbounded linear elastic media. It describes the propagation of two types of waves through the medium: waves of distortion or S-waves, in which particle motion occurs perpendicular to the direction of propagation of the wave, and waves of dilatation or P-waves, which correspond with the change of volume.

The dilatational wave equation is derived by taking the divergence of equation (2.6),

$$\nabla^2 \Delta = \frac{1}{c_p^2} \frac{\partial \Delta}{\partial t^2} \quad (2.7)$$

with $c_p = \sqrt{\frac{\lambda_L + 2\mu_L}{\rho}}$ the propagation velocity of the P-wave.

The distortional wave equation is obtained by taking the cross-product of the gradient operator and equation (2.6),

$$\nabla^2 \vec{\omega} = \frac{1}{c_s^2} \frac{\partial \vec{\omega}}{\partial t^2} \quad (2.8)$$

in which $c_s = \sqrt{\frac{\mu}{\rho}}$ represents the propagation velocity of the S-wave.

Often, linear elastic material parameters are provided in terms of Young's modulus E and Poisson's ratio ν . They are related to the Lamé parameters λ_L and μ_L by,

$$\lambda_L = \frac{\nu E}{(1 + \nu)(1 - 2\nu)} \quad \text{and} \quad \mu_L = \frac{E}{2(1 + \nu)} \quad (2.9)$$

Alternatively, bulk modulus K and shear modulus G can be used.

$$K = \lambda_L + \frac{2}{3}\mu_L \quad \text{and} \quad G = \mu_L \quad (2.10)$$

With these parameters, the expressions for the wave propagation velocities become,

$$c_p = \sqrt{\frac{K + \frac{4}{3}G}{\rho}} \quad \text{and} \quad c_s = \sqrt{\frac{G}{\rho}} \quad (2.11)$$

2.2.2 Solution for 1-D elastic wave equation

A general solution of the 1-D wave equation for P-waves will be derived using elementary theory to serve as analytical solution for comparison with the numerical solution in section 2.5. This theory supposes that the motion due to the wave is primarily one-dimensional. In a linear elastic material this can be accomplished by setting Poisson's ratio ν to zero. The Lamé parameters then become $\lambda_L = 0$ and $\mu_L = \frac{E}{2}$. Substituting this in the three-dimensional wave equation (2.6) and accounting for one-dimensional motion by $\vec{u} = u$, gives the one-dimensional wave equation,

$$\frac{\partial^2 u}{\partial x^2} - \frac{1}{c^2} \frac{\partial^2 u}{\partial t^2} = 0 \quad (2.12)$$

where $c = \sqrt{\frac{E}{\rho}}$ is the phase velocity of the one-dimensional wave. Taking the partial derivative of one-dimensional wave equation (2.12) with respect to x ,

$$\frac{\partial^2}{\partial t^2} \left(\frac{\partial u}{\partial x} \right) = c^2 \frac{\partial^2}{\partial x^2} \left(\frac{\partial u}{\partial x} \right) \quad (2.13)$$

shows that the strain, $\varepsilon = \partial u / \partial x$, is governed by the same one-dimensional wave equation that governs the displacement. A general solution of this equation was given by d'Alembert as,

$$\varepsilon = f_1(k(x - ct)) + f_2(k(x + ct)) \quad (2.14)$$

where f_1 and f_2 are arbitrary, twice-differentiable functions. k represents the wave number, defined as,

$$k = \frac{2\pi}{\lambda} = \frac{\omega}{c} \quad (2.15)$$

with λ , the wavelength and ω , the angular frequency. It can be seen that f_1 describes a wave propagating in positive x direction and f_2 one propagating in negative x direction. The boundary conditions applied determine which solution occurs in the real material. Since we are dealing with a linear relation between stress and strain, the general d'Alembert solution, equation (2.14), can be written as a series of time-harmonic waves,

$$\varepsilon = \text{Re} \left(\sum_j |\varepsilon_j| e^{i(k_j x - \omega t)} \right), \quad j = 1 \text{ to } \infty \quad (2.16)$$

in which i denotes the imaginary number and $\text{Re}(a)$ the real part of number a .

Wave propagation in a slender elastic beam of infinite length will be used in this chapter for determination of the numerical quality of Finite Element Models. It is assumed that the beam consists of the domain $x \geq 0$. It is loaded with a prescribed force history, $F(x = 0, t)$ at its edge, $x = 0$. Since there is only one-dimensional

motion, the cross-area of the beam remains constant ($A = A_0$), so the resulting strain at the beams edge can be written as,

$$\varepsilon(x = 0, t) = \frac{F(x = 0, t)}{EA_0} \quad (2.17)$$

Since $x \geq 0$ and since the boundary condition is applied at $x = 0$, the only physical realistic wave will be a forward propagating one. The general solution for the strain wave propagating the beam therefore will be of the form,

$$\varepsilon(x, t) = f(k(x - ct)) \quad (2.18)$$

Applying boundary condition (2.17) the analytical solution for the strain history inside the slender beam becomes,

$$\varepsilon(x, t) = \frac{F(k(x - ct))}{EA_0} \quad (2.19)$$

2.2.3 Viscoelastic theory

Linear viscoelastic material behaviour can be included in the linear elastic theory by simply writing both bulk modulus and shear modulus as complex quantities (denoted with superscript *), as,

$$G^*(\omega) = G'(\omega) + iG''(\omega) \text{ and } K^*(\omega) = K'(\omega) + iK''(\omega) \quad (2.20)$$

in which $G'(\omega)$ and $K'(\omega)$ are called elastic or storage moduli and, $G''(\omega)$ and $K''(\omega)$ are loss moduli and $i = \sqrt{-1}$ the imaginary number. Note that all properties depend on the angular frequency, ω . The complex moduli reduce to the real linear elastic moduli, defined by equation (2.10), when the loss moduli are zero and the storage moduli are independent of frequency.

The complex moduli are used in equation (2.11) to obtain complex phase velocities for P-waves,

$$c_p^*(\omega) = \sqrt{\frac{K^*(\omega) + \frac{4}{3}G^*(\omega)}{\rho}} \quad (2.21)$$

and for S-waves,

$$c_s^*(\omega) = \sqrt{\frac{G^*(\omega)}{\rho}} \quad (2.22)$$

or more generally,

$$c^*(\omega) = \|c^*(\omega)\| e^{i\varphi} \quad (2.23)$$

in which $\|c^*(\omega)\|$ is the 2 norm and $\varphi(\omega)$ the phase angle of the complex phase velocity. The general solution for a forward propagating time-harmonic displacement wave in a viscoelastic material can be written in complex notation as,

$$\vec{u} = A\vec{d}e^{i(k^*(\omega)\vec{x}\cdot\vec{p}-\omega t)} \quad (2.24)$$

in which , $k^*(\omega)$ is the complex wave number, \vec{x} the position vector, and \vec{p} and \vec{d} unit vectors in the directions of wave propagation and particle displacement respectively. $k^*(\omega)$ can be obtained by substituting the complex phase velocity, $c^*(\omega)$ in equation (2.15) while assuming that the angular velocity, ω , is a real number,

$$k^*(\omega) = \frac{\omega}{\|c^*(\omega)\|} (\cos\varphi(\omega) - i\sin\varphi(\omega)) = k_{re}(\omega) + ik_{im}(\omega) \quad (2.25)$$

In this equation, index *re* and *im* denote the real and imaginary parts of a complex quantity respectively. Substitution in equation (2.24) yields,

$$\vec{u} = A\vec{d}e^{-k_{im}\vec{x}\cdot\vec{p}}e^{ik_{re}(\vec{x}\cdot\vec{p}-\frac{\|c^*\|^2}{c_{re}}t)} \quad (2.26)$$

Attenuation Equation (2.26) shows that the amplitude of the wave decreases as function of the imaginary part of the wave number, $k_{im}(\omega)$, and the distance traveled $\vec{x} \cdot \vec{p}$. This is called wave attenuation. For this reason, $k_{im}(\omega)$, is often denoted in literature as attenuation coefficient, $\alpha(\omega)$.

Dispersion The effective *phase velocity*, which we define here as the phase velocity by which a wave with certain frequency actually travels in the material, is given in equation (2.26) by,

$$c_{eff}(\omega) = \frac{\|c^*(\omega)\|^2}{c_{re}(\omega)} \quad (2.27)$$

Note that $c_{eff}(\omega)$ is frequency dependent, i.e. components with different frequencies will travel at different phase velocities. This is called *dispersion*. For linear elastic material behaviour, c_{eff} reduces to the real, frequency independent, elastic wave velocity according to equation (2.11).

2.3 Importance of wave phenomena in the human head

The extent to which wave phenomena are present in the human head during an impact is estimated using elementary wave theory. Lower and upper frequency bounds for which wave propagation occurs will be estimated using boundary conditions, posed by geometry, and viscoelastic material damping. Furthermore, waves, traveling inside the head, will reflect at boundaries between the various substructures within the head. As a result P-waves can convert to S-waves and vice versa. This mode conversion can act as a different source for the presence of a certain wave type.

2.3.1 Lower bound of frequency range

As explained in Chapter 1, the dynamic response of the contents of the head is said to be dominated by wave propagation when the characteristic loading time is on the

order of the time constants of the system, reflected in the system eigenfrequencies. A lower bound for the frequency range at which waves exist can be found by observing the largest wavelength, λ_{max} , that fits within the head diameter, L , i.e.

$$\lambda_{max} = \frac{c}{f_{min}} = L \quad (2.28)$$

Assuming a head diameter of 0.2 m and applying a typical shear wave velocity of 5 m/s [102] provides a typical lower frequency bound of 25 Hz for S-waves. For P-waves the propagation velocity equals 1550 m/s [45; 83], providing a minimum frequency of 7750 Hz .

2.3.2 Upper bound of frequency range

Since brain tissue behaves like a viscoelastic solid, waves traveling in the tissue will display frequency dependent attenuation. An upper bound of the frequency range for wave propagation in the head is defined as the frequency at which an incident wave will be attenuated by 99% after having propagated 0.2 m through the head, i.e. from one side to the other.

S-waves Values for storage and loss shear modulus do depend significantly on frequency (see for example [120]). Also there is a large spread between values reported by various authors. Values at upper and lower end of the measured frequency spectrum found in literature, are used to obtain an impression of the extreme situations of material damping (see Table 2.1). Application in the viscoelastic solution, equation (2.26), provides the amplitude of the wave as a function of frequency f and distance traveled $\vec{x} \cdot \vec{p}$. The normalised amplitude of S-waves as function of frequency and distance traveled, is shown in Figure 2.1. The attenuation when using the Peters *et al.* data is larger than in the Shuck *et al.* data. For this reason, the upper bound for the relevant frequency range for S-waves in the head has been estimated to be 300 Hz using the Shuck *et al.* data.

P-waves Etoh *et al.* [45] determined the attenuation coefficient, α , of brain tissue for frequencies between 0.35 and 5 MHz using ultra sound. Their data was found to be in range of older data by Goldman and Hueter [61], and could be fitted by the following function,

$$\alpha = af^2 + \frac{b}{2\pi}f \quad (2.29)$$

Table 2.1: Material parameters used for estimating the viscous behaviour of brain tissue.

| Reference | G' [Pa] | G'' [Pa] | Frequency [Hz] |
|----------------------------|------------------|------------------|----------------|
| Peters <i>et al.</i> [120] | 600 | 150 | 16 |
| Shuck <i>et al.</i> [134] | $1.5 \cdot 10^5$ | $8.0 \cdot 10^4$ | 400 |

The values of the fit parameters a and b were not mentioned in their paper but were determined graphically from fit results presented instead; $a = -1.7 \cdot 10^{-12} s^2/m$ and $b = 7.1 \cdot 10^{-5} s/m$. This function fits the experimental data well for frequencies up to 3 MHz approximately. Figure 2.2 shows the normalised amplitude of a P-wave obtained using the fitted attenuation coefficients as function of frequency and propagation distance. The attenuation at 0.2 m equals 53% at 350 kHz and increases to 98% at 3 MHz. When assuming equation (2.29) to be valid for frequencies below 350 kHz also, it can be seen that the attenuation at 0.2 m is less than 10% for frequencies up to 50 kHz.

2.3.3 Reflection: mode conversion

In general, two phenomena can be observed when a wave hits a boundary of two media with different material properties. First, part of the incident wave will be reflected and another part will be diffracted into the other medium. Second, mode conversion can occur, i.e. a P-wave transforms into an S-wave and vice versa (refer to e.g. [1] for more information on mode conversion). In the head however, mode conversion is expected to be irrelevant. This is due to the different frequency ranges at which P- and S-waves can propagate inside a head. When a P-wave would be

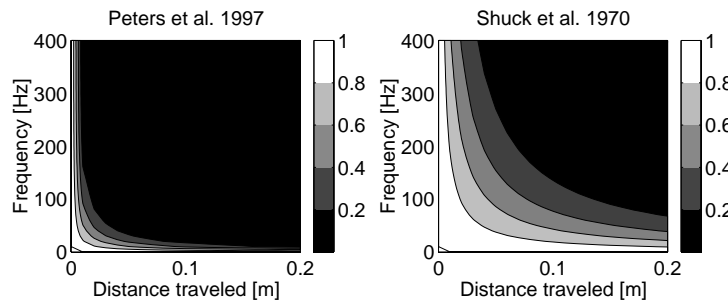


Figure 2.1: Normalised amplitude of S-waves in brain tissue as a function of frequency and propagation distance, based on linear viscoelastic theory. Shear moduli taken from Table 2.1.

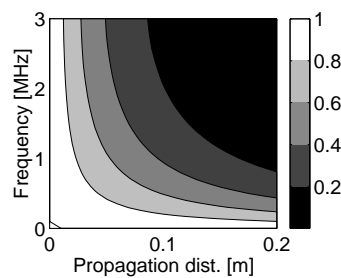


Figure 2.2: Attenuation behaviour of P-waves according to fitted data by [45]. Normalised amplitude as function of frequency and propagation distance.

converted in to an S-wave, its frequency would be that high that the S-wave would be attenuated in very short distance, thus disabling effective propagation. When a S-wave will be converted in a P-wave, the frequency will be that low that the resulting pressure will more be of a structural dynamical response instead of a wave propagation response.

2.4 Simulation of wave propagation: theoretical considerations

When simulating elastic wave propagation using the explicit Finite Element Method, both accuracy and numerical stability are important. These phenomena are influenced by both the spatial and temporal discretisation used.

2.4.1 Numerical stability

In typical FE codes used for impact modelling, time discretisation is performed using explicit time integration methods such as the Central Difference Method (e.g. LS-DYNA3D [86], PAM-CRASH [117], MADYMO [148]). In such explicit time integration method, quantities for the next time increment are predicted from known quantities at current and previous moments in time. No iteration is performed during one time increment, providing low computational effort per time step. However, small time steps have to be used because explicit integration methods are only conditionally stable. For the Central Difference Method, the maximum time step Δt_{max} to be used for stability is determined by the the Courant number [38], C ,

$$C = \frac{c \cdot \Delta t_{max}}{\Delta x} \leq 1 \quad (2.30)$$

This requirement means that, during one time step, the distance traveled by the fastest wave in the model ($c \cdot \Delta t_{max}$) should be smaller than the smallest typical element size in the mesh (Δx). The stability requirement gives an upper bound for the time step to be used. If a smaller the time step is taken the time integration procedure becomes more accurate.

2.4.2 Numerical accuracy

Two error sources appear when wave propagation is modelled using FEM: *numerical dispersion* and *spurious reflections*. Both error sources depend mainly on the spatial discretisation used (element formulation and mesh density). In explicit FE codes, spatial discretisation is usually achieved by constant strain elements with linear displacement functions and lumped mass matrices. A three-dimensional brick element contains eight integration points when full integration is applied. Computational costs can be reduced by using a reduced integration technique in which only one integration point per element is used. Both methods will be considered.

Numerical dispersion is the phenomenon that waves of different wavelength travel at different phase velocities due to numerical artefacts. For constant strain elements with lumped mass matrices, it can be shown analytically that, in a one-dimensional situation, the phase velocity in the discrete mesh c_{FEM} is related to the theoretical phase velocity c via [20],

$$\frac{c_{FEM}}{c} = \frac{\sin \frac{\pi \Delta x}{\lambda}}{\frac{\pi \Delta x}{\lambda}} \quad (2.31)$$

This means that the phase velocity in the discrete mesh is dependent on the wavelength λ and element size Δx . Also it can be seen that there cannot be any wave propagation when $\Delta x = \lambda$. Since wavelength λ is related to its frequency f by the phase velocity c , an upper bound on the frequency in the mesh for which no waves will be propagated can be found as [17; 20],

$$f_{cutoff} = \frac{c}{\Delta x} \quad (2.32)$$

Mullen and Belytschko [103] extended this analysis to two-dimensional Finite Element semi-discretisations. They considered the two dimensional wave equation which is valid for both P-waves and S-waves. Figure 2.3 shows the dispersion $\frac{c_{FEM}}{c}$ in square elements, as a function of the angle between the elements and wave propagation direction. Θ . It can be seen that the dispersion increases when Θ increases from 0 to 45° . Moreover, numerical dispersion depends on the element integration scheme used, full versus reduced integration. For $\Theta = 0$, no differences between fully and reduced integrated elements exist and dispersion is governed by equation (2.31). However, when a wave arrives at a certain angle $\Theta \neq 0$, the dispersive errors in the reduced integrated elements increase stronger than in the fully integrated ones.

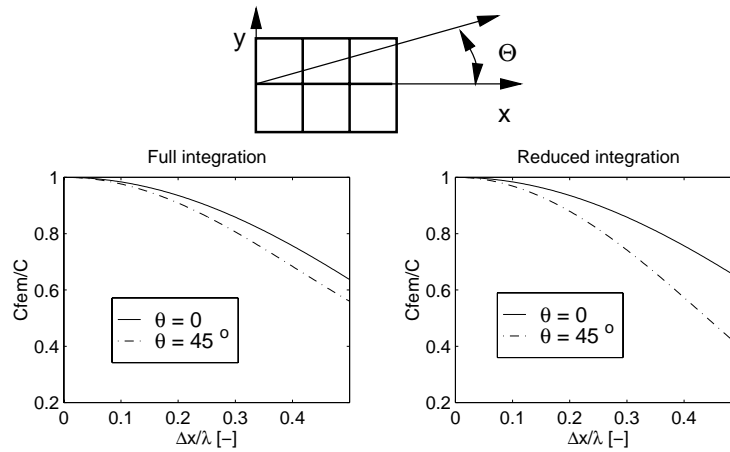


Figure 2.3: Numerical dispersion in bilinear quadrilateral elements with lumped mass matrix, as a function of relative mesh density $\frac{\Delta x}{\lambda}$ for various directions Θ (extreme values shown) (Figure according to theory in [103]).

It can be concluded that for constant strain elements with lumped mass matrix, commonly used in explicit FE codes, 18 elements per wavelength should be used to reduce the dispersion error to less than 1%, independent of incident angle.

Spurious reflection due to mesh non-uniformity In a uniform Finite Element mesh, elastic waves propagate without reflection. However, due to non-uniformity in the mesh distribution, spurious reflections can occur in the computed solution. Bažant *et al.* [17] analyzed a compressive wave traveling in a rectangular mesh consisting of two uniform parts with different element sizes (Δx_1 and Δx_2 in Figure 2.4). Amplitudes of the waves diffracted and reflected at the transition plane between the mesh parts were derived analytically. Influences of element size ratio $\frac{\Delta x_2}{\Delta x_1}$, and number of elements per wavelength of the second mesh part, $\frac{\lambda}{\Delta x_2}$, were determined and shown in Figure 2.5. In the ideal case there would be no reflection, so the amplitude of the, normalised, diffracted wave would be equal to one. Figure 2.5 shows that spurious reflection occurs when a wave passes between two elements of different sizes. For increasing element size difference this reflection increases. It can also be seen that this effect is more prominent when wavelength λ covers only a few

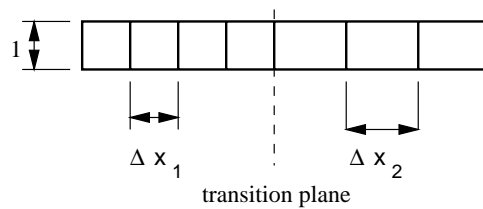


Figure 2.4: Rectangular Finite Element Mesh used by Bažant *et al.* [17]

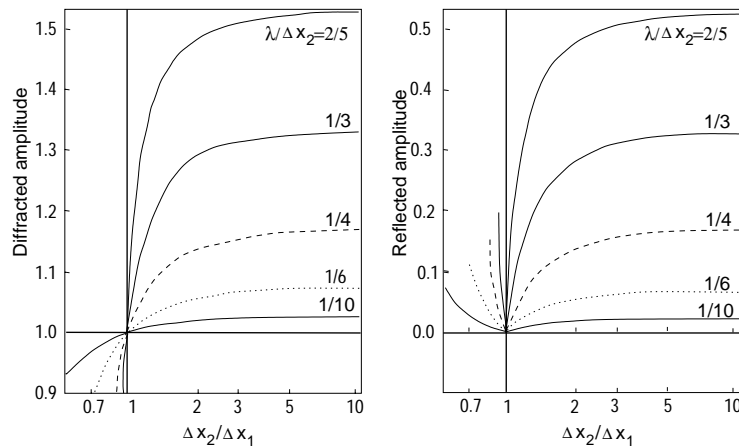


Figure 2.5: Amplitude of diffracted wave and reflected wave normalised to the amplitude of the incident wave, as function of mesh size ratio $\frac{\Delta x_2}{\Delta x_1}$ and relative mesh size $\frac{\lambda}{\Delta x_2}$. (Data taken from [17])

Finite Element sizes Δx_2 . If $\lambda > 10\Delta x_2$ the normalised amplitude of the reflected wave will be less than 2.5% for all mesh size ratios shown.

2.5 Simulation of wave propagation: numerical results

The theory presented in previous section is valid for single frequency waves only and does not take into account effects of the temporal discretisation. In a realistic loading history, multiple frequencies are present. The resulting wave form therefore will be a wave envelope consisting of components with various wavelengths. In this section, suitable discretisation requirements for realistic input conditions are investigated. This has been done by modelling the propagation of one-dimensional P-waves in a slender linear elastic beam in an explicit Finite Element Code (MADYMO), thus taking in to account both temporal and spatial discretisation. The reason for modelling P-waves is to obtain a true one-dimensional problem which is impossible while modelling S-waves.

2.5.1 Analytical solution

For slender beams in which the wavelength is much longer than the beam diameter, one-dimensional elementary wave theory can be used. The beam is loaded at one edge by a prescribed force history, $F(t)$, resembling a pulse obtained by impacting a head of a seated cadaver [104]. This pulse is often used for benchmarking head models (e.g. [37; 72]). For reasons of simplicity the pulse is approximated by,

$$F(t) = F_{max} \sin^4(2\pi f_0 t) \begin{cases} F_{max} = 6900 \text{ N} & 0 \leq t \leq \frac{1}{2f_0} \\ F_{max} = 0 \text{ N} & t > \frac{1}{2f_0} \end{cases} \quad (2.33)$$

with $f_0 = 62.5 \text{ Hz}$ (see Figure 2.6). The analytical solution for the strain wave is

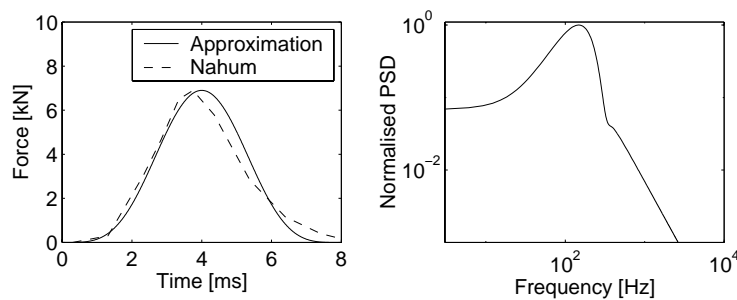


Figure 2.6: Input force history fitted on Nahum pulse [104] (left) and power spectral density normalised to maximum frequency contribution (right).

obtained by substituting $F(t)$ into equation (2.19),

$$\varepsilon(x, t) = \frac{F_{max}}{EA_0} \sin^4 \left(\frac{2\pi f_0}{c} (x - ct) \right) \quad (2.34)$$

2.5.2 The numerical model

A slender linear elastic beam has been modelled in MADYMO. The length of the beam was chosen as 30 m and its square cross-sectional area, A_0 , was set to $9 \cdot 10^{-4} \text{ m}^2$. The material properties of the beam are such that the wave propagation velocity c_0 approximates the speed of sound in brain tissue ($1500 \frac{\text{m}}{\text{s}}$ [45; 83]). To obtain a true one-dimensional wave propagation response, Poisson's ratio, ν , is set to zero. The material parameters are shown in Table 2.2.

Spatial discretisation The beam has been modelled using cubic elements, with one element over the cross-section of the beam. As shown in section 2.4, choices of both spatial and temporal discretisation depend on the wavelength expected in the mesh. In Figure 2.6, the Power Spectral Density of the input force pulse normalised to its maximum value is shown. It can be seen that frequencies which contribute with more than 1 percent to the total power cover a wide frequency range (normalised PSD > 0.01 for $0 \leq f \leq 830 \text{ Hz}$). In the absence of a distinct characteristic frequency, the discretisation will be arbitrarily related to the longest wavelength present. It is determined by the duration of the force applied and equals, $\lambda_{max} = \frac{c_0}{2f_0} = 12 \text{ m}$. Mesh densities ranging from 12 to 100 elements per maximum wavelength have been used. When changing the mesh density, the initial shape of all elements was kept cubic by adapting the area of the beam edge, A_0 .

Boundary conditions The impact on the beam has been modelled by a prescribed nodal force at the beam edge at $x = 0$ according to equation (2.33). In order to enable comparison of the strain results, the prescribed load has been scaled to the beam area, A_0 , such that the applied stress remains the same for all mesh densities.

Temporal discretisation The maximum time step required for stability is determined by the Courant number in equation (2.30). The Courant number is kept at constant value when applying different mesh densities. In the reference

Table 2.2: linear elastic material parameters used for modelling one-dimensional P-wave propagation in a linear elastic slender beam with MADYMO.

| Material parameter | Value |
|-----------------------------|------------------------|
| E | 2.25 GPa |
| ν | 0.0 [-] |
| ρ | 1000 kg/m ³ |
| $c = \sqrt{\frac{E}{\rho}}$ | 1500 m/s |

simulations, a Courant number of $\frac{1}{2}$ was used. Also a Courant number of 0.8475 (the maximum Courant number MADYMO allows) has been used to study the effect of the time discretisation on the accuracy of the solution. The simulation time has been set to 20 ms, which is the theoretical time for the wave to reach to end of the beam. In this manner no reflection at the end of the beam should occur during the simulation.

2.5.3 Results

Strain histories obtained with 12 elements per longest wavelength are compared to the theoretical results at various positions in the beam in Figure 2.7. In theory the pulse propagates through the beam without any dispersion, i.e its shape remains the same. In the numerical solution three types of error arise: the amplitude is overestimated, the amplitude reduces during propagation, and the shape of the wave envelope changes. This latter error is characterised by decrease and increase of the strain gradients at the front and rear of the wave envelope respectively. Furthermore additional waves trailing the actual wave envelope occur.

The errors will be analysed more quantitatively in terms of maximum absolute strain, strain rate and wave envelope propagation velocity.

Strain and strain rate Figure 2.8 shows the relative error, E_{rel} , in the strain amplitude and maximum strain rate at various points in the beam as function of mesh density used. The relative error is defined as,

$$E_{rel} = \frac{|S_{num,max} - S_{th,max}|}{|S_{th,max}|} \quad (2.35)$$

in which $S_{num,max}$ and $S_{th,max}$ represent maximum values of numerical and theoretical solutions respectively.

The left plot in Figure 2.8 shows the error in the strain amplitude. This error seems to decrease while the wave travels through the beam. However, this is caused by the fact that the maximum strain is overestimated in the numerical solution. As the wave travels further the maximum amplitude will become less than the theoretical one and

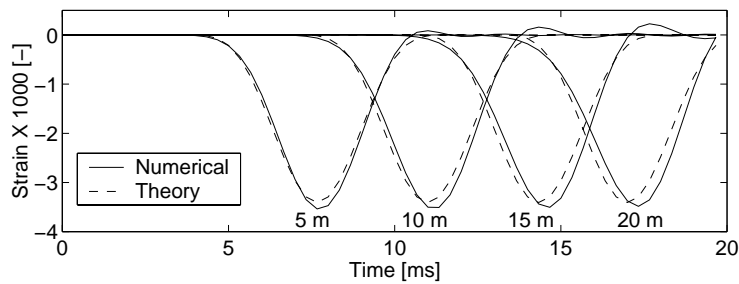


Figure 2.7: Numerical time-strain history determined at various positions in the beam. Numerical solution (12 elements/ λ_{max} , $C = 0.5$) versus theory.

the error will increase again. To reduce the relative error in the strain amplitude to less than 1%, mesh densities of approximately 24 elements per maximum wavelength have to be used. For coarser meshes the error increases strongly.

The relative error in the strain rate (Figure 2.8, right plot) increases while the wave propagates through the beam. For decreasing element sizes the error decreases. When 50 elements per maximum wavelength are used, the error decreases to less than 1%.

Wave propagation velocity Due to numerical dispersion, the shape of the wave envelope changes, making the determination of a single wave propagation velocity impossible. For this reason phase velocities are determined at five strain levels, $1000 \cdot \varepsilon = -1, -1.5, -2, -2.5, -3$, during increasing and decreasing phase of the strain. The mean, maximum and minimum phase velocities in the wave envelope obtained with two time step sizes, are shown in Figure 2.9 for increasing mesh density. It can be seen that increasing the element size provides lower wave propagation velocities, as expected theoretically. For the reference simulation ($C = 0.5$), the mean dispersion error becomes larger than 1% when less than 16 elements per maximum wavelength

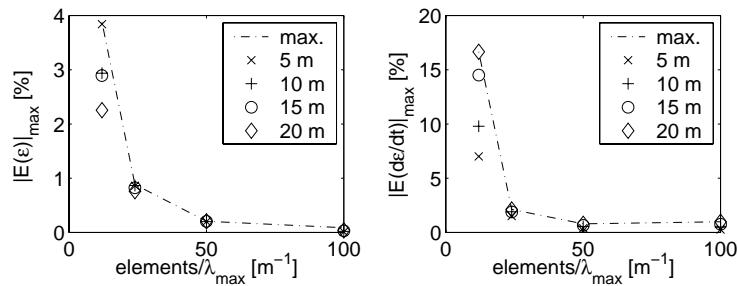


Figure 2.8: Relative errors in strain amplitude (left) and maximum strain rate (right) at various propagation distances (shown in legend) as function of mesh density used ($C = 0.5$).

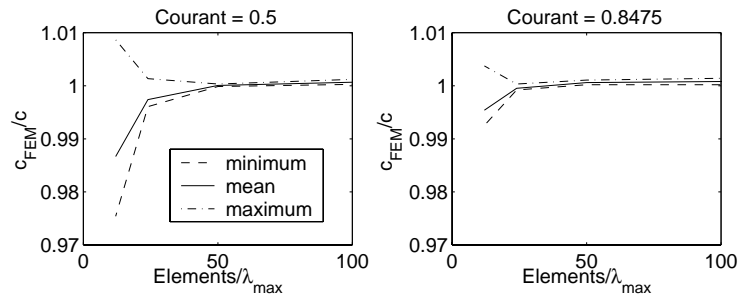


Figure 2.9: Effect of mesh density (in elements per maximum wavelength) and time step used on dispersion behaviour. Left: reference simulations, $C = 0.5$, right: maximum time step, $C = 0.8475$.

are used. The phase velocity values determined at the wave front, are smaller than the ones at the rear of the wave (indicated by the maximum and minimum values in the plots). This effect is larger for coarser meshes.

Comparing the left and right plots in Figure 2.9 shows that the errors obtained at the smallest time step ($C = 0.5$) are larger than the ones obtained at the larger time step. So, decreasing the time step size leads to an increasing dispersion error.

2.6 Discussion

Finite Element head models are used to assess the dynamical behaviour of the head. Most 3-D FE head models found in literature are developed using the explicit Finite Element Method. Linear (visco)elastic material behaviour for the brain tissue is assumed in all cases. For this reason the theory of the previous section can be used to assess if current headmodels are capable of describing wave phenomena correctly. First it will be estimated during which type of impacts the presence of wave propagation in brain tissue is likely. Then numerical requirements for accurate modelling will be summarised from previous sections. Implications of these findings for current state of the art headmodels will be provided next. Finally, some methods for improvement will be provided.

2.6.1 Wave propagation during head impact

The conditions for strain waves to propagate inside the head have been estimated using linear viscoelastic theory for isotropic material behaviour. A lower bound of the relevant frequency range is obtained by defining that waves can propagate only when the wavelength fits inside a typical head measure (0.2 m). The upper bound of the relevant frequency range is defined as the frequency at which an incident wave will be attenuated by 99% after having propagated 0.2 m . It was concluded that dilatational, or P-waves exist in a frequency range between 8 kHz and 3 MHz . This is consistent with findings of Young and Morpheu [165], who numerically analysed a fluid filled sphere and concluded that impact durations less than 0.1 ms were needed to obtain a wave propagation response instead of a structural dynamic one. Distortional or S-waves exist at frequencies between 25 Hz and 300 Hz . The contribution of mode conversion at reflection at the boundaries of brain substructures is considered to be of no importance, since the relevant frequency ranges for P- and S-waves are distinctly different.

The presence of wave propagation in the head also depends on impact loading applied. The analysis of the Power Spectral Density in section 2.5 showed that the upper bound for the frequency in typical, low velocity, traffic related impacts is on the order of 1 kHz . For this reason P-waves will not be present in such impact but S-waves will. During a non-penetrating ballistic impact, first a direct impact with a duration of approximately 2 to $100\text{ }\mu\text{s}$ [18; 23] will occur. After this, inertia will cause the head to rotate with a typical duration on the order of ms [22]. This means that P-waves can be present at the start and S-waves might develop later on. For this

reason it can be concluded that, from a mechanics point of view, wave propagation inside the head should be considered a real possibility for both low velocity, high mass, traffic related impacts as well as high velocity, low mass, ballistic impacts.

2.6.2 Numerical accuracy

When modelling wave propagation with explicit FEM two types of errors can appear: numerical dispersion and spurious reflection due to mesh inhomogeneities. Although only P-waves were considered in the accuracy analysis, the theory presented in section 2.4 is valid for both P- and S-waves. For this reason we assume that for modelling S-waves the same accuracy requirements hold.

Numerical dispersion The wave velocity calculated will always be lower than the analytical one due to numerical dispersion. For single frequency waves this could be investigated analytically. Taking less elements per wave length increases numerical dispersion. When the element size equals the wave length waves are not propagated anymore (see equation (2.32)). When modelling a realistic input, multiple frequencies are present. Waves with long wavelengths travel faster in the mesh than short ones (see Figure 2.3). As a result the strain gradient at the front of a wave envelope decreases in time while the gradient at the rear of the envelope increases. These effects have been quantified numerically using errors in maximum strain, strain rate and average propagation velocity of a wave envelope propagating in a beam. It was found that the strain rate requirement is the most stringent. When 24 elements per maximum wavelength are used, the strain rate error equals 2.5% after a wave has traveled 1.66 times its maximum wavelength (the length of the beam). The dispersion error (average propagation velocity) and maximum strain error then are less than 1%. Further increase of the mesh density leads to small improvements of the accuracy only. For this reason, 24 elements per maximum wavelength will be used as a guideline for accurate modelling of wave propagation.

However, some remarks have to be made. First, this value should be seen as a lower bound since it is determined for 1-D wave propagation only. The analytical results in Figure 2.3 on page 24 show that in the two-dimensional case, where waves do not necessarily propagate along the mesh direction, the number of elements per wavelength should be increased by 40%. Although not investigated here, it is expected that this effect will be stronger in a three dimensional mesh. However, this effect can be partially made ineffective by accounting for the effect of temporal discretisation. The error introduced by the Central Difference time integration scheme used by MADYMO proved to be compensatory with the dispersion error caused by the spatial discretisation. It can be derived theoretically, that for a Courant number $C = 1$ no dispersion will occur when elements with linear displacement interpolation functions are used [20]. Since all results presented are valid for $C = 0.5$, numerical dispersion can be reduced by taking the time step close to the critical time step determined by the Courant number. However, in a realistic mesh, multiple element sizes are present. This means that the Courant number varies per element. As a result, the gain in accuracy will vary per element also. Also, choosing the Courant

number close to one may result in instabilities when severe deformations occur. A solution of this problem is to update the time step during the simulation using the Courant criterion based on the deformed mesh. Finally, it has to be noted that the exact number of elements per maximum wavelength depends on the actual pulse shape used. For this reason the mesh density proposed should be used at reasonable smooth input signals only.

Spurious reflection due to mesh size inhomogeneities is expected to play a minor role when the mesh requirements for numerical dispersion are met. A numerical investigation in a simple one-dimensional layout showed that the dispersion requirements are indeed stronger than the ones on mesh homogeneity [26]. However it has to be reminded that only cubic elements were used in that study. The effect of strongly deformed or even degenerated elements was not investigated.

2.6.3 Implications for existing head models

As wave propagation in the brain is a real possibility, FE head models should be capable of accurate description of wave propagation. With given constraints such as temporal and spatial integration techniques currently present in explicit Finite Element codes, this accuracy is mainly determined by the element size used. It was seen that a wave can propagate in a one dimensional FE mesh with reduced integrated, lumped mass, constant strain elements, when the frequency is lower than the cut-off frequency provided in equation (2.32) on Page 24. For obtaining an accurate solution in a typical traffic related impact, at least 24 elements per maximum wavelength are needed. These facts will be used for estimating the performance of current FE head models.

The element size used in 3-D FE head models ranges from approximately 5 mm to 18 mm [36; 37; 40; 72; 77; 128; 167]. Assuming an element size of 5 mm and knowing that P-waves travel in brain tissue at approximately $1550 \frac{m}{s}$ [45], provides a cut-off frequency of 310 kHz while an accurate solution is provided for frequencies up to 13 kHz only. S-waves travel at approximately $5 \frac{m}{s}$ ($1-10 \frac{m}{s}$ [102]) yielding a cut-off frequency of 1000 Hz and a maximum frequency for accuracy of 42 Hz. These values are plotted in Figure 2.10 for comparison with the frequency ranges expected during traffic related and ballistic impact. Also, the frequency range for which S- and P-waves are expected inside the head are plotted. These numbers indicate that only the lower end of the relevant frequency spectrum can be modelled accurately. This is especially true since the frequency limits best case values based on one-dimensional theory and smallest element size reported. Given current estimations, it can be seen that the modelling demands for correct modelling of P-waves in a high velocity impact are most stringent. A coarse estimation is that for modelling S-waves, the frequency that limits the accuracy has to be increased by a factor of 10 while for P-waves this is a factor of 100.

2.6.4 Methods of improvement

The results presented here hold for explicit FEM which use constant strain elements with a lumped mass matrix and the Central Difference time integration scheme. A method to prevent spurious wave reflection as well as wave dispersion from overshadowing the true dynamic response in explicit FE packages is to eliminate all wavelengths which are smaller than the critical wavelength determined using the accuracy requirement in equation (2.31) or Figure 2.3. This can be done by expanding the applied load in a Fourier series and delete all frequency terms corresponding to wavelengths smaller than the critical one [17]. An other possibility is to adjust the mesh size such that the greatest part of the frequency contents of the applied load can be modelled correctly.

Although it is beyond the scope of this thesis to make alterations to element type and time integration scheme used, some comments on how to improve the prediction of wave propagation by using different spatial discretisation methods will be provided. Elements with lumped mass matrices are known to be computationally effective, but underestimate the wave propagation velocity. Elements with consistent mass matrix tend to overestimate wave velocities. The least dispersion was obtained when a generalised mass matrix $M = \frac{1}{2}M_{consistent} + \frac{1}{2}M_{lumped}$ was used [20]. Elements with quadratic interpolation functions were found to display negligible numerical dispersion. However, these elements can introduce a significant amount of additional noise into the solutions due to the existence of two solutions at each wavelength (refer to [20] for background information).

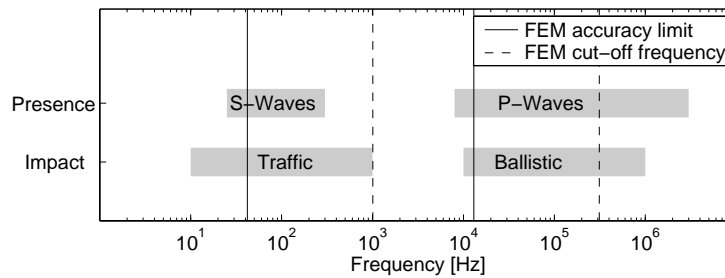


Figure 2.10: Capability of modelling wave propagation by current state of the art FE head models. *Impact:* Frequencies expected during various impact types. *Presence:* Frequencies at which waves can occur inside the head. *FEM accuracy limit:* maximum frequencies for accurate wave propagation modelling. *FEM cut-off frequency:* maximum frequency that can propagate in mesh (equation (2.32)).

2.7 Conclusions

The following conclusions can be drawn from previous discussion.

- Wave propagation inside brain tissue should be considered a real possibility for both low velocity, high mass, traffic related impacts as well as high velocity, low mass, ballistic impacts.
- Typically 24 elements per wave length are needed for accurate modelling.
- When decreasing the number of elements per wave length, the predicted wave propagation velocity decreases. As a result, computed maximum strain values and strain rate values will be incorrect
- In current state of the art 3-D human head models the smallest element size equals 5 mm, making accurate modelling of wave propagation impossible.
- For modelling S-waves the frequency that limits the accuracy of the model should be increased by a factor of 10. Reducing the mesh size of 0.5 mm is a possible solution, especially with the advances in computer hardware.
- For modelling P-waves current explicit FEM the frequency that limits the accuracy of the model should be increased by a factor of 100. Reducing the mesh size is not a realistic option anymore. Instead alternative methods should be pursued such as the use of elements with quadratic displacement functions or generalised mass matrix.

As developments on spatial and temporal discretisation methods are not a topic of this research, it is decided to emphasise shear phenomena in brain tissue for the remainder of this research.

Chapter 3

Comparison of the dynamic behaviour of brain tissue and two model materials

This section has been published in the Stapp Car Crash Conference proceedings¹. It contains the small strain characterisation of porcine brain tissue as well as that of two potential model materials for use in the physical head model. Brain measurement data are evaluated against literature data, and a model material has been chosen for use in the physical model in Chapter 6.

¹Brands, D.W.A., Bovendeerd, P.H.M., Peters, G.W.M., Paas, M., Bree ,van J. and J.S.H.M. Wismans (1999): "Comparison of the dynamic behaviour of brain tissue and two model materials", *Proceedings of the 43th Stapp Car Crash Conference*, Paper no. 99sc21, pp. 57-64.

Abstract

Linear viscoelastic material parameters of porcine brain tissue and two brain substitute materials for use in mechanical head models (edible bone gelatin and dielectric silicone gel) were determined in small deformation, oscillatory shear experiments. Frequencies to 1000 Hertz could be obtained using the Time/Temperature Superposition principle. Brain tissue material parameters (i.e. dynamic modulus (phase angle) of 500 (10°) and 1250 Pa (27°) at 0.1 and 260 Hz respectively) are within the range of data reported in literature. The gelatin behaves much stiffer (modulus on the order of 100 kPa) and does not show viscous behaviour. Silicone gel resembles brain tissue at low frequencies but becomes more stiffer and more viscous at higher frequencies (dynamic modulus (phase angle) 245 Pa (7°) and 5100 Pa (56°) at 0.1 and 260 Hz respectively). Furthermore, the silicone gel behaves linearly for strains up to at least 10%, whereas brain tissue exhibits non-linear behaviour for strains larger than 1%.

3.1 Introduction

Mechanical head models are used for head injury assessment and research. Most well known are crash dummy heads and head impactors used in approval tests for cars and helmets. Head models that include some anatomical structures such as the brain, can provide insight into the response mechanisms within the head at impact loading, thereby avoiding the technical and ethical problems related to in vivo and in vitro experiments on animals and humans. Moreover, they can provide validation data for numerical head models. An important component of such a detailed mechanical head model is the model material, mimicking the behaviour of real brain tissue.

In this study, linear viscoelastic material parameters of two brain substitute materials will be presented and compared with those of porcine brain tissue. The substitute materials are a gelatin mixture used by the North Atlantic Treaty Organisation (NATO) as a tissue mimicking material [105] and transparent silicone gel from Dow Corning (Sylgard 527 A&B dielectric silicone gel), a brain model material used previously in mechanical head models by Viano *et al.* [157] and Meaney *et al.* [92]. Both model materials and the porcine brain tissue were subjected to oscillatory shear experiments up to 16 Hz , on the same apparatus, making one on one comparison possible. By applying the Time/Temperature Superposition Principle for both brain tissue and model materials, the frequency range could be extended up to 1000 Hz [51].

3.2 Materials and methods

Experimental Setup

Experiments are performed on two rotational viscometers, Rheometrics Fluids Spectrometer II (RFS) and Rheometrics ARES (ARES) [125], using a plate-plate

configuration. These viscometers are basically the same. The temperature control on the ARES is more accurate, while the torque transducer of the RFS is more sensitive. Samples are centered between 50-mm diameter flat parallel disks. A prescribed oscillatory strain is applied on the one plate, while the torque is measured on the other plate that is fixed. The frequency range of the measuring devices is limited by inertial effects (0.1 to 16 Hz). The strain applied is defined as the plate displacement at the edge of the sample divided by the sample height. This sample height is determined by adjusting the distance between the plates such that the normal force measured reaches 0.1 mN. The plate distance then is measured with an accuracy of 1 μm using the build-in distance measurement device of the viscometers. When necessary a moist chamber is used to prevent dehydration of the sample.

For the oscillatory experiments a sinusoidal strain is imposed on the sample,

$$\gamma(t) = \gamma_0 \sin(\omega t) \quad (3.1)$$

When steady state is reached and strain amplitude γ_0 is sufficiently small, the shear stress τ will also be sinusoidal, but with a phase shift δ due to the viscous behaviour.

$$\tau(t) = G_d \gamma_0 \sin(\omega t + \delta) \quad (3.2)$$

Both viscoelastic characteristics, phase shift $\delta(\omega, T)$ and dynamic modulus $G_d(\omega, T)$, are functions of the angular frequency ω and temperature T . In principle we are interested in these parameters at one temperature (e.g., 38°C for brain tissue) for a frequency range up to several kHz. However, the frequency range of the viscometer is limited to 16 Hz. To obtain information on the material behaviour at higher frequencies the Time/Temperature Superposition principle (TTS) can be employed [120]. A set of isothermal characteristics, such as the phase angle, δ , and dynamic modulus, G_d , are determined within the measurable frequency range at different temperatures. Next, these characteristics are shifted along the logarithmic frequency axis to an arbitrarily chosen reference characteristic of this set, to form one smooth curve: the master curve. This whole curve, then, is valid for the temperature at which the reference characteristic is measured (i.e., the reference temperature T_{ref}). In this manner, frequencies higher than the maximum allowed test frequency can be assessed by lowering the temperature below the reference temperature. The frequency range that can be obtained in this manner thus depends on the temperature range that is used and on the temperature sensitivity of the material parameters. The TTS principle can be applied for linear viscoelastic material behaviour only. Its application is valid when indeed a smooth master curve can be obtained from the isothermal characteristics²

Materials

Brain tissue Porcine brain tissue was harvested from six-months-old pigs obtained from a local slaughterhouse, immediately following sacrifice by electrical shock. During transportation and preparation, the brain material was wetted with a

²For more details on the applicability of the TTS principle the reader is referred to Ferry (1980) [51].

physiological saline solution to prevent dehydration. Samples were cut using a cork bore. The time span between sacrifice and testing was approximately four hours.

The limited sensitivity of the torque transducers requires a certain minimum diameter of the sample. Cylindrical samples of 12-mm diameter were needed to provide measurement results within the measuring range. Since it proved to be impossible to obtain a sample of this diameter, consisting purely of white or grey matter, a sample was prepared from tissue out of the thalamus of porcine brain. This tissue is located near the center of the brain. Visual inspection showed that this tissue consists of a homogeneous mixture of grey and white matter. To eliminate scattering of measurement data by anisotropy, all samples were cut in the same direction with their cylinder axis perpendicular to the sagittal plane. The sample heights varied between 1 and 2 *mm*.

Gelatin model material Edible bone gelatin, used within NATO as a tissue mimicking material, was prepared by dissolving gelatin powder in water at 50°C. This liquid mixture was cooled down to room temperature to become a solid that could be tested. In this paper gelatin was tested in two mass ratios, a 20% solution (1 part gelatin and 4 parts water), as prescribed by the NATO regulation [105] and a 4% solution.

The 20% gelatin was shaped to cylindrical 10-mm diameter samples of thickness 1 to 2 *mm*. The 4% gelatin proved to be difficult in handling and could not be shaped. For this reason the warm, liquid, gelatin mixture was poured directly between the plates of the viscometer and cooled down in-situ. After cooling down the sample height was determined as previously described under EXPERIMENTAL SETUP. By this method, 50-mm-diameter samples with a height between 1.5 and 2 mm were obtained. An advantage of this method is that the maximum plate diameter can be used for measuring, providing better reproducibility of measurements due to absence of centering inaccuracy.

Silicone gel Silicone dielectric gel from Dow Corning (Sylgard(Dielectric Gel 527 A&B) is a brain substitute material previously used in physical head models by Viano *et al.* [157] and Meaney *et al.* [92]. This gel consists of two components that were mixed together in a one-to-one ratio. The gel was cured between the plates of the viscometer for four hours at a temperature of 65 °C. After cooling it down to room temperature (25°C) the height was re-adjusted as to account for possible shrinkage during curing (see EXPERIMENTAL SETUP). The diameter of the samples thus became 50 *mm* and the height was on the order of 0.35 *mm*.

Experimental protocol

Linear strain regime As explained before, linear viscoelastic theory can be applied only for sufficiently small shear strains. The boundaries of this linear regime were examined by carrying out oscillatory shear experiments with constant frequency (1.6 *Hz*) but increasing strain amplitude (0.1 to 10%). The linear range was

determined using the criterion that the material behaves linearly if the measured material parameters G_d and δ are independent of the applied strain amplitude. Different reference temperatures were used for different materials. The properties of the brain tissue were determined at $38^\circ C$, thus resembling the animal's body temperature. The material properties of the gelatin were determined at $10^\circ C$, which is its recommended temperature for use [105]. The silicone gel was measured at $25^\circ C$, resembling the laboratory environmental temperature at which it can be used in a mechanical head model.

Frequency sweep After the determination of the linear regime, experiments were carried out at increasing frequencies ($0.1-16\ Hz$) with a chosen, constant strain amplitude in the linear range (frequency sweep). In this it was assumed that this chosen strain amplitude lies in linear range for the complete measuring frequency range. The experimental results of porcine brain tissue, gelatin and silicone gel are compared with each other.

Time/Temperature superposition Frequency sweeps at different, constant, temperatures were performed to expand the frequency range using TTS. The master curves for the brain tissue were composed of 7 isothermal characteristics determined at temperatures between 4 and $40^\circ C$. This temperature range is bounded by the phase transition of water at $0^\circ C$ and the permanent brain damage that can result due to, for example, the solidifying of proteins at $41^\circ C$ [58]. The master curve for silicone gel was composed of 9 isothermal characteristics. Temperatures between $-50^\circ C$ and $25^\circ C$ were used. The wide temperature range necessary for the silicone gel could not be met by the RFS. For this reason, the ARES was used for both materials. Differences in measurement results of both viscometers under the same conditions were within the experimental spread of one viscometer. For gelatin no master curves were determined, for reasons that will be explained further on. Finally, it was checked whether the measurements at different temperatures had influenced the material properties of the sample by repeating a test at room temperature. Table 3.1 provides an overview of the experimental conditions.

Table 3.1: Overview of experimental conditions. n : number of samples, ΔT : temperature range, MC: Moist chamber (yes/no), d : sample diameter.

| Material | n | $\Delta T [^\circ C]$ | $T_{ref} [^\circ C]$ | MC | d [mm] | Device |
|---------------|----|-----------------------|----------------------|----|--------|----------|
| Porcine brain | 4* | 4, 40 | 38 | y | 12 | RFS-ARES |
| Gelatine 4% | 7 | 10, 15 | 10 | y | 50 | RFS |
| Gelatine 20% | 4 | 10, 15 | 10 | y | 10 | RFS |
| Silicone gel | 2 | -50, 25 | 25 | n | 50 | RFS-ARES |

*Each sample taken from a different animal.

3.3 Results

Linear strain regime

The results of the four brain tissue samples are shown in Figure 3.1. For strain amplitudes larger than 1%, the brain tissue was considered to behave non-linearly. All model materials were found to show linear viscoelastic behaviour within the strain range tested (i.e., up to 10% strain). For this reason, it was decided to use a strain amplitude of 1% for both frequency sweep as well as TTS.

Frequency sweep

In Figure 3.2, the results of the frequency sweep are shown. The dynamic modulus of the porcine brain tissue increases with frequency. It can be seen that the results of three samples spread within 30% range of their average, while the result of the fourth sample is significantly higher. Averaged over all samples, the dynamic modulus increases from 500 Pa at 0.1 Hz to 665 Pa at 10 Hz. The phase angle of brain tissue

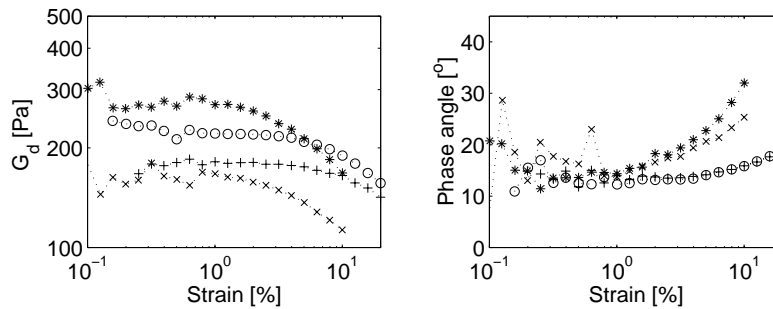


Figure 3.1: Dynamic modulus G_d (left) and phase angle δ (right) of four brain samples, versus strain amplitude at constant frequency $f = 1.6$ Hz, and temperature $T_{brain} = 38^\circ C$. Results of different samples denoted with different symbols.

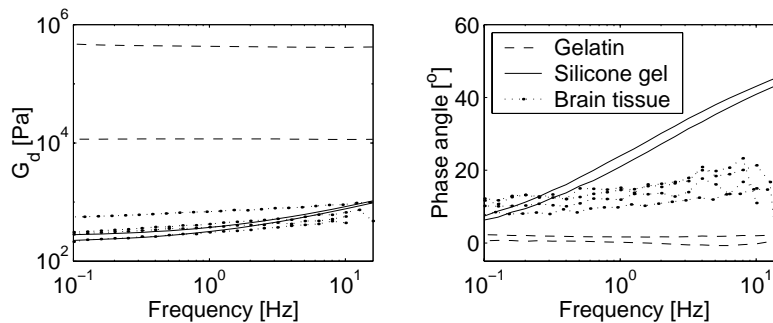


Figure 3.2: Dynamic modulus G_d (left) and phase angle δ (right) versus frequency f at constant strain amplitude 1%, $T_{brain} = 38^\circ C$, $T_{silicone} = 25^\circ C$.

increases from $10^\circ \pm 2.5^\circ$ at 0.1 Hz to $20^\circ \pm 5^\circ$ at 10 Hz . For frequencies higher than 10 Hz , strong deviations with respect to the previous trends at lower frequencies can be seen. Since these deviations even lead to negative phase angles, these are considered to be an experimental artefact. For this reason, results at frequencies higher than 10 Hz will not be used for application of TTS.

The dynamic modulus for silicone gel is in the range of the one for brain tissue. It starts at approximately 150 Pa at 0.1 Hz and increases to 1100 Pa at 16 Hz . The phase angle starts off at approximately 5° at 0.1 Hz and increases strongly with increasing frequency to 45° at 16 Hz . The dynamic moduli for the gelatin mixtures are significantly higher than the dynamic moduli for brain and silicone gel. The dynamic modulus for the 20% gelatin mixtures equals approximately 470 kPa and does not increase with frequency (maximum and minimum values within 7% range). The phase angle for the 20% gelatin mixture is less than 2 degrees. Decreasing the proportion of gelatin to 4% decreases the dynamic modulus to approximately 11.6 kPa , which is still higher than the moduli of brain tissue and silicone gel. The phase angle also decreases. It can be concluded that the gelatin behaves nearly perfectly elastic.

Time/Temperature Superposition

In the previous section it was shown that gelatin is too stiff and too less viscous to resemble the material behaviour of brain tissue. For this reason it was decided to exclude the gelatin from further investigation.

The master curves for brain tissue and silicone gel shifted to their reference temperatures, are shown in Figure 3.3. Overlapping parts of all isothermal curves matched well, so TTS was considered to be applicable.

The frequency range of the master curves for brain tissue, shown in Figure 3.3, ranges up to 1000 Hz . At 1000 Hz the dynamic modulus and the phase angle are about 2 kPa and 30° respectively. For the silicone gel the master curve ranges to 260 Hz . The dynamic modulus of the silicone gel increases more strongly for increasing frequency

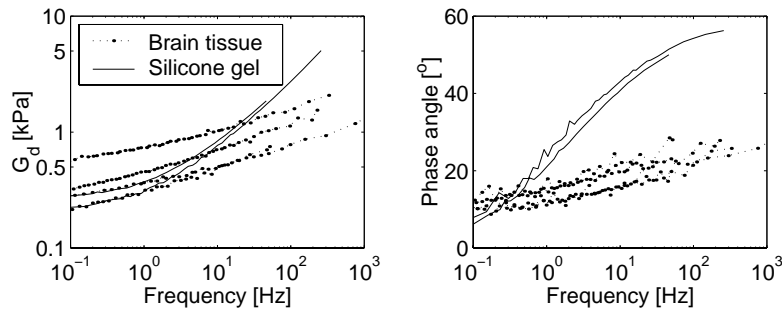


Figure 3.3: Master curves of 4 samples of porcine thalamus tissue ($T_{reference} = 38^\circ \text{C}$) and 2 samples of silicone gel ($T_{reference} = 25^\circ \text{C}$) obtained by oscillatory tests with $\gamma_0 = 1\%$. Dynamic modulus G_d (top) and phase angle δ (bottom) versus frequency.

than the one of brain tissue. At 260 Hz it reaches 5100 Pa whereas the average dynamic modulus for brain tissue equals 1250 Pa . The phase angle for the silicone gel also increases more progressively. At 260 Hz for example, the phase angle for the silicone gel reaches 56° whereas the one for brain tissue equals approximately 27° . The re-tests of silicone gel and brain tissue at their reference temperatures showed that the temperature changes did not permanently alter the material properties.

3.4 Discussion

Mechanical head models that include some anatomical structures, such as the brain, can be used for head injury assessment, for gaining insight into the response mechanisms within the head at impact loading or for validation purposes for numerical head models. An important component of such a model is the material that mimics the dynamical behaviour of brain tissue.

In this study, two brain mimicking materials and porcine brain tissue were subjected to small strain, oscillatory shear experiments. It was shown that both model materials behave linear viscoelastic for strains up to at least 10% while brain tissue behaves linearly to only 1%. In the linear strain range, the Time/Temperature Superposition principle could be applied for capturing the high frequency behaviour of the materials.

Brain Tissue

Master curves that span a frequency range to 1000 Hz could be obtained. Peters *et al.*, who investigated the validity of the TTS principle on white matter tissue of calf brains, obtained a frequency range to 1 MHz , by measuring between 6 and $38^\circ C$ [120]. Apart from different animal origin, no explanation for the different frequency range can be provided. These findings on the applicability of the principle are in contrast to findings of Arbogast *et al.* [14] who could not find any temperature dependency of the material behaviour of brain tissue within the temperature range mentioned above.

For the brain tissue both the dynamic modulus and the phase angle show an increasing tendency for increasing frequencies. Our results are within the range of the data reported in literature, shown in Figure 3.4. These are presented in terms of elastic (or storage) modulus G' and viscous (or loss) modulus G'' . They can be obtained from the dynamic modulus G_d and phase angle δ using [51],

$$G' = G_d \cos(\delta) \quad (3.3)$$

and

$$G'' = G_d \sin(\delta) \quad (3.4)$$

For reasons of clarity, data by Shuck and co-workers, who performed material characterisation on human cerebral brain tissue [135; 134], are not included in Figure 3.4. In a frequency range of 5 to 350 Hz , they found a storage modulus ranging from 7.6 kPa to 33.9 kPa and a loss modulus ranging from 2.8 kPa to 81.4 kPa

($\gamma_0 = 1.3\%$). These values are significantly higher than the ones shown in Figure 3.4. The reason for this is unknown, but differences that are expected to influence the material parameters, might exist in post-mortem time, amplitude of applied strain and different donors.

Model Materials

The applicability of the model materials in a mechanical head model is predominantly determined by the mimicking qualities of the model materials, but also by their experimental manageability. The latter includes factors such as aging, temperature sensitivity and ease of preparation, which are important in every day laboratory practice. Both considerations will be discussed.

For the Sylgard 527 A&B silicone gel a frequency range up to 260 Hz could be obtained by applying TTS in the chosen temperature range of 25 to $-50^\circ C$. It is believed that the frequency range can be expanded to higher frequencies, without any problems, by measuring at temperatures below $-50^\circ C$.

Our results correspond well with the findings of Arbogast *et al.* [6]. They presented the dynamic shear modulus of the same silicone gel for testing their high frequency shear device. Unfortunately they did not report the phase angle so this could not be compared with our data.

The dynamic modulus of silicone gel equals that of brain tissue in a range up to 10 Hz . For higher frequencies, up to 260 Hz , the silicone gel becomes stiffer than brain tissue. Thus, when applied in a head model at room temperature, strains in the silicone gel are expected to be lower than in real brain tissue, for those frequencies. Moreover, these high frequency strains will be damped stronger in the silicone gel than in brain tissue, since the phase angle and hence the loss modulus, of the gel is higher than that of brain tissue.

The experimental manageability of the silicone gel proved to be good. The effect of

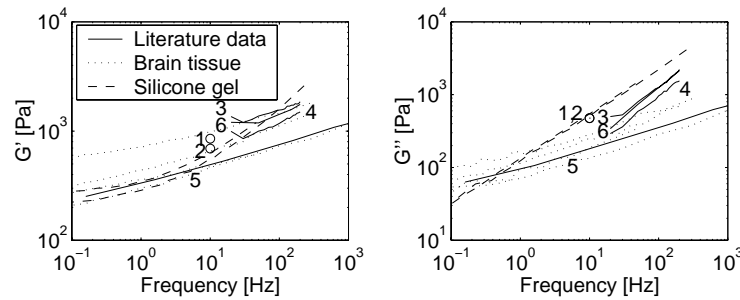


Figure 3.4: Storage modulus G' (left) and loss modulus G'' (right) of measured results (brain tissue ($n=4$) and silicone gel ($n=2$)), and literature data (numbered): 1. human white matter [50], 2. human cerebrum [91], 3. porcine brainstem ($\gamma_0 = 2.5\%$) [5], 4. porcine cerebrum ($\gamma_0 = 2.5\%$) [142], 5. calf cerebrum ($\gamma_0 = 1.0\%$) [120], 6. porcine cerebrum ($\gamma_0 = 2.5\%$) [143].

material aging is tested by repeating a frequency sweep test, at room temperature, after the material had been in the measuring device for three days at 25°C. The dynamic modulus showed an increase of approximately 10% over the complete frequency range. The phase angle showed a decrease of 2.5 degrees. Repeating the experiment one day after this, did not reveal additional differences. For this reason it can be concluded that the influence of material aging is low.

The dynamic modulus of the gelatin model material was decades higher than the modulus of brain tissue (a factor of 50 for the 4% gelatin solution and a factor of 2000 for the 20% solution). The phase angle remained almost zero (0-2°). Both quantities did not depend on frequency. This indicates that, within the frequency range tested (0.1-16 Hz), the gelatin behaves as a nearly perfect elastic solid that is too stiff for mimicking brain tissue. In theory, the stiffness of the gelatin can be lowered by using lower percentage mixtures than the 4% mixture. However, in practice this is not possible because of the high damage sensitivity of the material, causing it to break up at very low strains. Furthermore, the material behaviour of the gelatin was very sensitive to aging (parameters change within hours after preparation) and mechanical failure. For these reasons it can be concluded that gelatin is not suitable as a model material for brain tissue.

Accuracy analysis

The accuracy of the measurement is determined by the accuracy with which the shear can be applied on the oscillating plate, and the measuring accuracy of torque on the fixed plate. The rotation of the plates can be applied with discrete steps of $5 \cdot 10^{-6}$ rad [125]. With the diameters and thicknesses used, the relative discretisation error in the applied shear becomes 4% of the shear strain amplitude for the silicone gel. For brain tissue this is 0.15%. The torque can be measured with a relative error of 0.16% [125]. In translating the measured torque into the dynamic modulus, this relative error has to be increased with relative errors in the sample height, the applied strain and four times the relative error in the sample diameter [164]. In this manner the total relative error in the dynamic modulus was estimated to be 20% for the brain tissue and 5% for the silicone gel measurements.

In the experiments, the assumed pure shear deformation requires that the sample is in a stress-free state before loading. Indeed the samples are stress-free, immediately after they are mounted in between the plates (neglecting earth gravity). However, since they stick to the plates, depending on possible shrinkage during cooling down and/or curing, the stress-free state might be lost. By adjusting the plate distance before each measurement such that the normal force on the (cured) sample is close to zero, we tried to restore the stress-free state as much as possible. Finally, during curing of the gels, and by adhesion to the plates, the molecular structure, and thus the mechanical behaviour, of the gel near the plates might differ from that in the bulk material. As a consequence the measured material parameters would depend on sample thickness. A test using silicone gel with a sample thickness of 0.9 mm revealed that the difference with the 0.35-mm results presented in Figure 3.2, is smaller than the spread between the 0.35-mm results themselves. Thus the measured properties are believed to be bulk properties.

Limitations of current work

For determining the material behaviour of a model material to be used in a mechanical head model under real impact conditions, the material has to be investigated at finite strains and high frequencies. Typical frequencies are on the order of 1000 Hz , whereas studies on isolated axons indicate strains of about 15% to be responsible for injury [141]. In this paper the small strain behaviour was determined in the complete relevant frequency range using the Time/Temperature superposition theory. For determination of the large strain behaviour the TTS theory is not valid. Even if linear viscoelastic parameters, such as G_d and δ , are obtained from oscillatory strain measurements outside the linear range, they have no meaning, since the basic assumption of these experiments, that a sinusoidal strain input leads to a sinusoidal stress output, has been violated. For this reason, material properties in the 1% range cannot be extended into the 15% range, relevant for injury. Characterisation of the materials at large strains requires additional test methods such as stress or strain relaxation experiments. This will be subject of future work (Chapter 4).

Finally, this study is limited in that reasonable large brain samples had to be used which did not exist of white or grey matter only. For this reason, the reported material properties are to be considered as average properties of grey and white matter. Also effects of anisotropy, resulting from fibre structure, were averaged in this way.

3.5 Conclusions

It can be concluded that 4% and 20% edible bone gelatin mixtures are not suitable for application as a brain tissue model material in a mechanical head model. The dynamic modulus of Dow Corning Sylgard 527 A&B silicone dielectric gel is similar to that of porcine thalamus tissue for strains up to 1% at frequencies up to approximately 10 Hz . For higher strains brain tissue behaves non-linear while the silicone gel behaves linear for strains up to at least 10%. Above 10 Hz the dynamic modulus of the silicone gel increases much stronger with frequency than the one of brain tissue. At 1% strain, the phase angle of silicone gel is similar to that of brain tissue only up to 1 Hz . Above 1 Hz it increases more with frequency than that of brain tissue. Thus, silicone gel may be used in mechanical head models to obtain a qualitative impression of the behaviour of the brain tissue during accident conditions but strain levels in the gel will differ from those in the real brain.

3.6 Acknowledgments

The authors would like to acknowledge TNO Prins Maurits Laboratory and Ford Motor Company for their financial support of this research, N. Plasmans and R. Bours for conducting part of the experiments and B. de Wit of slaughterhouse 'de Wit Geldrop BV', for providing the porcine brain tissue.

Chapter 4

Large shear strain dynamic behaviour of brain tissue and silicone gel model material

This chapter contains a paper presented at the Stapp Car Crash Conference in Atlanta, GA, USA, November 2000¹ It is a continuation the material experiments presented in Chapter 3 in that the mechanical characterisation of brain tissue as well as the silicone gel material model for large shear strains is concerned. These results will be used for determination of a material model and material parameters in the following chapters.

¹Brands, D.W.A., Bovendeerd, P.H.M., Peters, G.W.M and J.S.H.M. Wismans (2000): "The large strain dynamic behaviour of in-vitro porcine brain tissue and a silicone gel model material", *The Stapp Journal*, 44, pp. 249-260.

Abstract

The large strain dynamic behaviour of brain tissue and silicone gel, a brain substitute material used in mechanical head models, was compared. The non-linear shear strain behaviour was characterised using stress relaxation experiments. Brain tissue showed significant shear softening for strains above 1% (approximately 30% softening for shear strains up to 20%) while the time relaxation behaviour was nearly strain independent. Silicone gel behaved as a linear viscoelastic solid for all strains tested (up to 50%) and frequencies up to 461 Hz . As a result, the large strain time dependent behaviour of both materials could be derived for frequencies up to 1000 Hz from small strain oscillatory experiments and application of Time Temperature Superpositioning. It was concluded that silicone gel material parameters are in the same range as those of brain tissue. Nevertheless the brain tissue response will not be captured exactly due to increased viscous damping at high frequencies and the absence of shear softening in the silicone gel. For trend studies and benchmarking of numerical models the gel can be a good model material.

4.1 Introduction

Mechanical head models that include anatomical structures such as the brain, can provide insight into the response mechanisms within the head at impact loading. Moreover, they can provide validation data for numerical head models. An important component of such detailed mechanical head model is the model material, mimicking the behaviour of real brain tissue in the relevant mechanical range. This range comprises strains up to 20%, the strain level associated with injury [141], and frequencies up to 1000 Hz , a frequency typical for traffic related impacts.

A model material previously used for mimicking the behaviour of brain tissue in physical head models is Dow Corning Sylgard 527 A&B dielectric silicone gel [71; 92; 157]. In a previous study we compared the small strain dynamic behaviour of the model material with that of porcine brain tissue [27] and with the small strain brain tissue results by other authors [5; 50; 91; 120; 142; 143]. It was concluded that for strains up to 1%, the dynamic behaviour of silicone gel resembles that of brain tissue for frequencies up to 260 Hz .

In this study, oscillatory shear experiments and stress relaxation experiments have been performed at finite strain levels on both silicone gel and porcine brain tissue, completing the material characterisation in the full relevant dynamic range.

4.2 Materials and methods

Experimental setup

Simple shear experiments have been performed on a rotational viscometer (Rheometrics ARES [125]). Samples were placed between 25-mm diameter flat parallel disks. A prescribed rotation was applied on the one plate, while the torque, T ,

was measured on the other plate that was fixed. For determining the sample height, the distance between the plates was lowered until the normal force measured reached $0.1mN$. The plate distance was then measured with an accuracy of $1\ \mu m$ using a build-in measurement device of the viscometer. Correct temperature conditions were obtained by controlled air temperature. Dehydration of the brain tissue samples was prevented by controlling humidity using a custom build moist chamber. To prevent slip between the brain tissue samples and the plates two methods of sample fixation were investigated. First a cyanoacrylate adhesive (Sicomet 85, Henkel, Germany) has been used to fixate the samples to the plates and second the coefficient of friction of the plates has been increased by fixing waterproof sandpaper (P220) to the plates using two-sided adhesive tape.

Data acquisition

If we assume that there is no material displacement perpendicular to the plate surfaces, the strain in the sample can be written as a function of time t and radius r as,

$$\gamma(r, t) = \frac{\theta(t)r}{H} = \frac{\gamma_R(t)r}{R}, \quad 0 < r < R \quad (4.1)$$

where θ represents plate rotation, H the sample height, $\gamma_R(t)$ the strain at the sample edge and R the sample radius. The total transient torque can be written as a function of the strain at the sample edge as,

$$T(t, \gamma_R) = 2\pi \int_0^R \tau(r, t)r^2 dr \quad (4.2)$$

For linear strain independent material behaviour, the integral can be solved exactly. By introduction of the shear modulus $G(t) = \tau(r, t)/\gamma(r, t)$, the modulus, $G_a(t)$, can be determined as a function of total transient torque and the strain at the plates edge,

$$G_a(t) = \frac{2T(t, \gamma_R(t))}{\pi R^3 \gamma_R(t)} \quad (4.3)$$

This modulus, which is obtained directly from the viscometer, represents the true material parameter, $G(t)$, for strains within the linear regime of the material only. For strains outside the linear range, $G_a(t)$ denotes an apparent modulus that represents some average modulus over the strain range present in the material.

All moduli and strains, presented in this paper, are apparent moduli, defined by equation (4.3), and strains at the sample edge unless stated otherwise.

Sample preparation

Brain Tissue Porcine brain tissue was harvested from six-months-old pigs obtained from a local slaughterhouse, immediately following sacrifice by electrical shock. During transportation, complete hemispheres were submerged in a physiological

saline solution to prevent dehydration. Sagittal slices were cut using a standard rotating-disk meat slicer (Bizerba GmbH & Co., Balingen, Germany). From these slices, 24-mm diameter cylindrical samples were cut using a cork bore. Samples were prepared from tissue located near the centre of the brain (thalamus region). Visual inspection showed that this tissue consists of a mixture of grey and white matter parts. To eliminate scattering of measurement data by anisotropy, all samples were cut in the same direction with their cylinder axis perpendicular to the sagittal plane. The sample heights varied between 2.3 and 3.6 mm. The time span between sacrifice and end of testing was approximately four hours. All samples were kept refrigerated at 4°C and submerged in a physiological saline solution until the actual experiment started.

Silicone gel Silicone dielectric gel from Dow Corning (Sylgard Dielectric Gel 527 A&B) is a brain substitute material previously used in physical head models [71; 92; 157]. This gel consists of two components that were mixed together in a one-to-one ratio. The gel was cured between the plates of the viscometer for four hours at a temperature of 65°C. After cooling it down to room temperature (25°C) the height was re-adjusted as to account for possible shrinkage during curing (see section 4.2). The diameter of the samples thus became 25 mm and the height was on the order of 1.3 mm.

Loading conditions

Two types of loading conditions have been used: oscillatory strain for characterising the linear behaviour of the materials and step strain with subsequent stress relaxation for the non-linear behaviour.

Oscillatory strain During the oscillatory experiments a sinusoidal strain is imposed on the sample,

$$\gamma(t) = \gamma_0 \sin(\omega t) \quad (4.4)$$

When steady state is reached and strain amplitude γ_0 is sufficiently small, the shear stress τ will also be sinusoidal, but with a phase shift δ due to the viscous behaviour,

$$\tau(t) = G_d \gamma_0 \sin(\omega t + \delta) \quad (4.5)$$

Both viscoelastic characteristics, phase shift, $\delta(\omega, t)$, and dynamic modulus, $G_d(\omega, T)$, are functions of the angular frequency, ω , and temperature, T . To obtain information on the material behaviour at higher frequencies than the maximum frequency of the viscometer, 16 Hz, the Time/Temperature Superposition principle (TTS) can be employed [27; 120]. A set of isothermal characteristics, such as the phase angle δ and dynamic modulus G_d , was determined within the, viscometer-limited, frequency range at different temperatures, ω_T . Next, the phase angle characteristic was shifted along the logarithmic frequency axis to an arbitrarily chosen reference characteristic

of this set, to form one smooth curve: the master curve. This master curve is valid for the temperature at which the reference characteristic is measured (i.e., the reference temperature T_{ref}). The amount of horizontal shift per isothermal characteristic was quantified by the horizontal shift factor, a_T , and the effective frequency for which a shifted result is valid, ω_{eff} , was obtained by,

$$\omega_{eff} = a_T \omega_T \quad (4.6)$$

Next, the horizontal shift factors obtained in this manner, were applied to the dynamic modulus, G_d . A small vertical shift, b_T , was then applied to the modulus to obtain a smooth dynamic modulus master curve. This vertical shift factor is commonly associated with density changes due to temperature changes and is usually on the order of 1 [21]. In this manner, frequencies higher than the maximum allowed test frequency can be assessed by lowering the temperature below the reference temperature. The TTS principle is valid when indeed a smooth master curve can be obtained from the isothermal characteristics [51].

Stress relaxation For investigating the non-linear strain behaviour of a material, oscillatory experiments can only be used when a material model is assumed, just as G_d and δ are linear viscoelastic material model parameters. Investigation of the non-linear strain behaviour of the material without making model assumptions can be achieved by performing stress-relaxation experiments.

During stress relaxation experiments, in principle, a step strain, γ_0 , is imposed on the sample. Since this is not possible in reality, stress relaxation was achieved by imposing a strain, γ_R , on the sample within 0.1 s and keeping it constant thereafter (see Figure 4.1). The resulting torque was measured and used to calculate the apparent shear modulus, $G_a(t, \gamma_R)$ by means of equation (4.3). The relaxation modulus thus obtained corresponds to,

$$G_a(t, \gamma_R(t)) = \tau(t, \gamma_R(t)) / \gamma_R(t) \quad (4.7)$$

It represents the real stress relaxation modulus (i.e. the relaxation modulus as if obtained from a true step strain) only when the strain is at constant value and inertia effects have faded away.

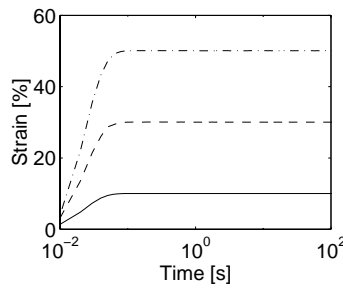


Figure 4.1: Example of strain history applied on silicone gel sample. indicating that a constant strain value was reached within 0.1 s.

During the brain tissue experiments it was observed that the relaxation curves for different strain values have a tendency to be parallel. This suggests that, the stress relaxation modulus can be separated into a strain and a time dependent part,

$$G_a(t, \gamma_R) = h_a(\gamma_R)G(t) \quad (4.8)$$

In this equation the time dependent behaviour, which is represented by $G(t)$, equals the linear viscoelastic modulus (which does not depend on strain). $h_a(\gamma_R)$ equals the damping function determined from the apparent modulus, G_a [87]. The damping function thus quantifies the effect of the strain applied on the shear modulus.

When time strain factorisation can be carried out, the material characterisation will be simplified considerably, since the time dependent behaviour can be obtained for high frequencies using the linear oscillatory experimental results. The validity of this time strain factorisation for brain tissue has been investigated by applying equation (4.8) on the experimental data. For each sample, a scaling function, $H(t, \gamma_R, \gamma_R^{ref})$, was defined as,

$$H(t, \gamma_R, \gamma_R^{ref}) = \frac{G_a(t, \gamma_R)}{G_a(t, \gamma_R^{ref})} \quad (4.9)$$

If factorisation is valid, the scaling function $H(t, \gamma_R, \gamma_R^{ref})$ will be independent of time and correspond to the damping function $h_a(\gamma_R)$ when γ_R^{ref} is chosen in the linear range of the material. The scaling function, $H(t, \gamma_R, \gamma_R^{ref})$, was time-averaged to $\bar{H}(\gamma_R, \gamma_R^{ref})$, and the large strain relaxation moduli, $G_a(t, \gamma_R)$ then were normalised to γ_R^{ref} using,

$$G_{norm}(t, \gamma_R^{ref}) = \frac{G_a(t, \gamma_R)}{\bar{H}(\gamma_R, \gamma_R^{ref})} \quad (4.10)$$

Experimental protocol

Linear strain regime: Oscillatory strain Silicone gel has been shown to behave linear for strains up to at least 10% at 16 Hz [27]. In this paper the behaviour of the silicone gel has been investigated up to 50% strain and higher frequencies. First, isothermal measurements at constant strain amplitudes of 1% and 20% but increasing frequencies (0.1 Hz to 32 Hz) were performed at temperatures ranging from 25 to -60°C (Dynamic Frequency Sweeps, DFS). Master curves were created from the isothermal DFS results using Time Temperature Superpositioning and shift-factors were determined. Next, oscillatory experiments with constant frequency, 16 Hz, but increasing strain amplitudes, up to 50% (Dynamic Strain Sweeps, DSS) were performed at 24, -40, -50 and -60°C. At each temperature, the linear range of the material was determined by checking for which strain values the material parameters were strain independent. Possible permanent effects of these low temperatures on the material properties were checked by repeating a measurement at 24°C after the low temperature measurements were completed. Effective frequencies for the DSS results

were obtained by using the horizontal shift-factors obtained from the TTS results, and $f=16 \text{ Hz}$ in equation (4.6).

Oscillatory strain experiments on brain tissue were performed to study the effects of the different adhesion methods on brain tissue by comparing the results obtained with adhesion methods with those obtained without adhesive methods in our previous study [27]. For brain tissue it has been shown that the linear range is on the order of 1% strain [27]. For this reason all master curves were constructed from isothermal characteristics at 1% strain and frequencies up to 16 Hz. Temperatures between 4°C and 38°C have been used. Low temperature measurements have been performed first to minimise the effect of sample ageing due to autolytic processes in the brain tissue.

Non-linear strain regime: Stress-relaxation Strain values ranging from 5% to 20% were applied on 4 samples of brain tissue and the apparent modulus was measured during 100 s. The temperature used equals 38°C. Two samples of silicone gel were tested at 24°C and at 10, 30 and 50% strain values to provide results for comparison with those of brain tissue. By testing two samples an indication of reproducibility of the measurement could be obtained. Given the ramp shape of the prescribed strain in Figure 4.1, it has been assumed that the measured shear modulus equals the stress relaxation modulus due to a step response for $t > 0.1 \text{ s}$. An overview of all experimental conditions is provided in Table 4.1.

Time-strain factorisation To compare the relaxation behaviour of the various samples more quantitatively, time dependent and strain depend behaviour were observed separately. First, scaling function, $H(t, \gamma_R, \gamma_R^{ref})$, was determined from the stress relaxation results using equation (4.9), and choosing $\gamma_R^{ref} = 5\%$ ($n=3$) and 6% ($n=1$). The value of H was evaluated for $t = 0.1$ to 9.6 s with time intervals of 0.5 s. Then these values were time averaged, as to obtain damping function values, $\bar{H}(\gamma_R, \gamma_R^{ref})$, from which the normalised relaxation moduli, $G_{norm}(t)$, were determined using equation (4.10).

Table 4.1: Overview of experimental conditions. n : number of samples, ΔT temperature range, MC: Moist camber (yes/no), d sample diameter, $\Delta\gamma$: strain range

| Material | Measurement type | n [-] | ΔT [°C] | T_{ref} [°C] | MC | d [mm] | $\Delta\gamma$ [%] |
|--------------|------------------|------------|--------------------|-------------------|----|-------------|-----------------------|
| Silicone gel | DSS | 1 | -60;24 | 24 | n | 25 | 1;50 |
| | DFS+TTS | 3 | -60;24 | 24 | n | 25 | 1;50 |
| | SR | 2 | 24 | 24 | n | 25 | 10&50 |
| Brain tissue | DFS+TTS | 5* | 4,38 | 38 | y | 24 | 1 |
| | SR | 4* | 38 | 38 | y | 24 | 5;20 |

DSS = Dynamic Strain Sweep, DFS+TTS = Dynamic Frequency Sweep and application of Time Temperature Superpositioning, SR = Stress Relaxation

* 2 adhesive fixed samples, 2 sandpaper fixed samples

4.3 Results

Oscillatory strain experiments

Silicone gel Figure 4.2 shows master curves of silicone gel obtained from dynamic frequency sweeps at 1 and 20% strain (three samples used), together with the horizontal shift factors a_T .

The dynamic modulus ranges from 258 Pa to 15.2 kPa at 0.16 and 1150 Hz respectively, while the average phase angle values vary from 9.4° to 57° at 0.16 and 417 Hz. Maximum differences with respect to the mean value, due to different samples, were 21% for the dynamic modulus and 15% for the phase angle, both at $f=0.16$ Hz. For dynamic modulus and phase angle respectively, these differences decrease to 7.2% and 2.8% at 50Hz and 0.4 and 0.26% at 260 Hz. Horizontal shift factors up to 28 were obtained at -60°C . Between the three samples, the horizontal shift factors coincided within 2%.

The results of the 16 Hz, Dynamic Strain Sweeps on silicone gel, performed at 24, -40, -50 and -60°C , are shown in Figure 4.3. The change in dynamic modulus over a strain range from 1 to 50% equals less than 1.6% for all temperatures except at -60°C . At this temperature the dynamic modulus increases 8.3% with respect to its minimum value. For strains up to 36% the difference remains within 5%. When increasing the strain from 1 to 50%, the change in phase angle is less than 2.3% for all temperatures. Repeating the 24°C measurement after the low temperature measurements gave maximum differences in dynamic modulus and phase angle of 1.35% and 0.58% respectively. The effective frequencies at which the results are valid were determined using the average shift factors, $a_{T,mean}$, from the master curves. They are shown in Table 4.2.

Brain tissue To estimate the effect of the fixation methods (adhesive and sandpaper) on small strain oscillatory results, master curves have been constructed and compared with those obtained without fixation in Figure 4.4. It can be seen

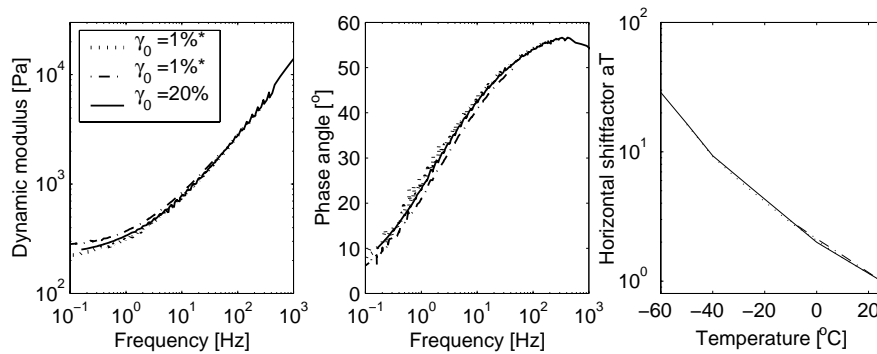


Figure 4.2: Master curves for Dow Corning Sylgard 527 A&B silicone gel ($T = 24^\circ\text{C}$ and 25°C [27]) at strain amplitudes from [27]. Dynamic modulus (left), phase angle (middle), horizontal shift factor, a_T (right).

that the dynamic moduli of the fixed samples lie between the non fixed ones for frequencies above 0.7 Hz. Fixed values tend to be in the lower regions of the non fixed range. The phase angle values of the fixed samples lie between the results obtained without fixation except for one sandpaper fixed sample.

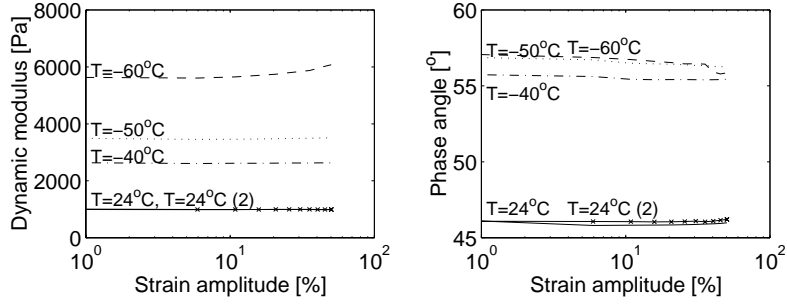


Figure 4.3: Determination of the linear strain range of silicone gel at several temperatures. Dynamic Strain Sweeps performed at 16 Hz and at 24°C, -40°C, -50°C and -60°C and repeated thereafter on 24°C (2). Dynamic modulus (left) and phase angle (right) versus strain amplitude.

Table 4.2: Shift factors $a_{T,mean} \pm \text{range}$ from Dynamic Frequency Sweep tests, at temperatures used in Dynamic Strain Sweep Experiments. Effective frequency, f_{eff} , calculated using average shift factor $a_{T,mean}$ and the DSS frequency of 16 Hz.

| T [°C] | n [-] | $a_T \pm \text{range}$ [-] | f_{eff} [Hz] |
|----------|---------|----------------------------|----------------|
| 24 | 3 | 1±0 | 16 |
| -40 | 2 | 9.3±0.1 | 149 |
| -50 | 2 | 16.4±0.2 | 262 |
| -60 | 1 | 28.8 | 461 |

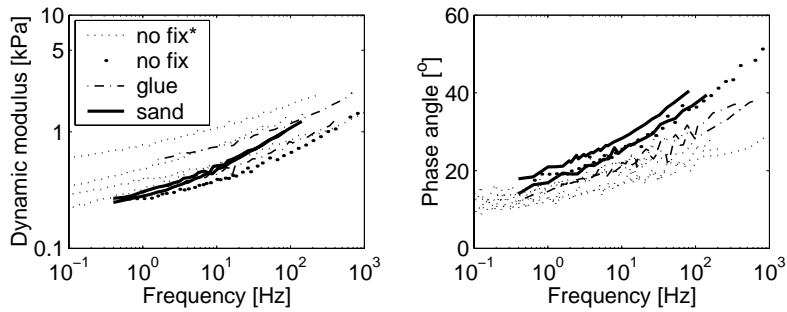


Figure 4.4: Master curves of porcine brain tissue to show the effect of fixation method (adhesive (glue), $n=2$ and sand paper (sand), $n=2$, no adhesion method (no fix), $n=1$) on small strain response ($\gamma_R = 1\%$, $T_{ref} = 38^\circ C$). Results presented in [27] ($n=4$), obtained without adhesion method, printed as reference (no fix*). Dynamic modulus (left) and phase angle (right) versus frequency.

Stress relaxation experiments

Silicone gel In Figure 4.5 the shear moduli of the silicone gel were determined from the strain history depicted in Figure 4.1 and application of equation (4.3). Note that the strain is not at constant value for times less than 0.1 s. Although also shear moduli were determined for times less than 0.1 s, only moduli obtained after 0.1 s were considered to be pure relaxation moduli. The average relaxation modulus of sample 1 obtained from measurements at three strain values (shown in Figure 4.5, upper plot), equals 357 ± 12.8 Pa and 216 ± 10.6 Pa at 0.1 and 100 s respectively (mean values standard deviation). When the strain is increased from 10% to 50% the time-averaged increase of the modulus of sample 1 equals 12.6% (t=0.1s to 100s). The shear modulus of sample 2 increases by 4.1% at the same strain range. The strain-averaged relaxation moduli of both samples differ by 3.8% with respect to their mutual average (Figure 4.5, right plot). With respect to time dependent behaviour it can be observed that both relaxation moduli reach a plateau value. Between 27 and 100 s the average modulus changes by 1 percent only.

Brain Tissue Stress-relaxation experiments were performed on four brain tissue samples. Strain values applied vary between 5 and 20%. In Figure 4.6 stress relaxation moduli of brain samples are shown. Results obtained with the silicone gel at $\gamma_R = 10\%$ were included for comparison. All brain tissue samples show shear strain softening for strains up to 20%, i.e. the relaxation modulus decreases as a function of strain applied. While shear strain softening seems consistent per sample, the associated change of relaxation modulus (approximately 35%) is less than the spread between relaxation moduli of different samples (approximately 90%). Also it can be observed that the relaxation modulus does not reach a plateau value after 100 s.

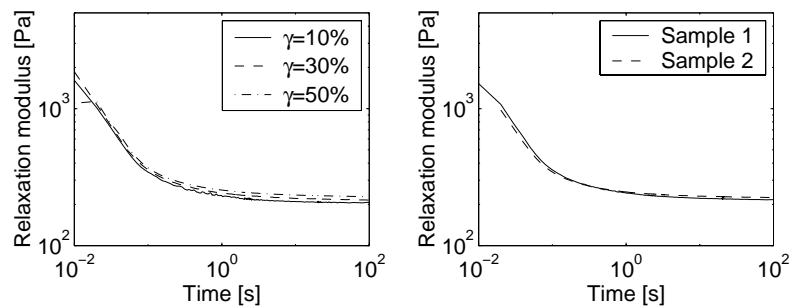


Figure 4.5: Stress relaxation results for one sample of silicone gel at three strain levels, indicating presence/absence of strain dependency (left) ($T = 24.3^\circ\text{C}$, $\gamma_R = 10, 30$ and 50%). Average shear moduli per sample, ($n=2$) obtained at 3 strain levels, indicating reproducibility (right). Moduli represent relaxation moduli for $t > 0.1$ s.

Time-strain factorisation The scaling function, $H(t, \gamma_R, \gamma_R^{ref})$, was determined by choosing $\gamma_R^{ref} = 5\%$ (samples G1, G2 and S1) and 6% (sample S2). The values of H , evaluated for $t = 0.1$ to 9.6 s with time intervals of 0.5 s, are shown in figure 4.7 . The scaling functions of sample G1 do not seem to depend on time (maximum change in time less than 3.4% with respect to the time-averaged value). Also the 10% result of the G2 sample, and the 20% result of sample S1 do not show a clear trend (maximum changes 4.1% and 12% respectively). The 20% result of sample G2 and the 16% and 20% results of the S2 sample show a decreasing trend in time (maximum changes 16% for G2 ($\gamma_R=20\%$) and 26% for S2 ($\gamma_R=20\%$), respectively). This trend is predominately present during the first 0.6 s. This means that if time-strain separation is applied according to equation (4.10), the maximum error in the time-dependent normalised relaxation modulus, $G_{norm}(t, \gamma_R^{ref})$, equals 26%. If we neglect the 0.1 s value of H , the largest error decreases to 13.8%. The effect of leaving out the 0.1 s results on the time averaged damping function values, \bar{H} , equals 1.1% at maximum. Time averaged damping function values, $\bar{H}(\gamma_R, \gamma_R^{ref})$, as well as normalised relaxation moduli, $G_{norm}(t, \gamma_R^{ref})$, are shown in Figure 4.8 . The results for sample G1 deviate from those of G2, S1 and S2. For the latter three samples the average shear softening at 20% strain is 30% \pm 6.8% (mean \pm standard deviation). The mean relaxation modulus varies from 367 \pm 130 Pa at 0.1 s to 173

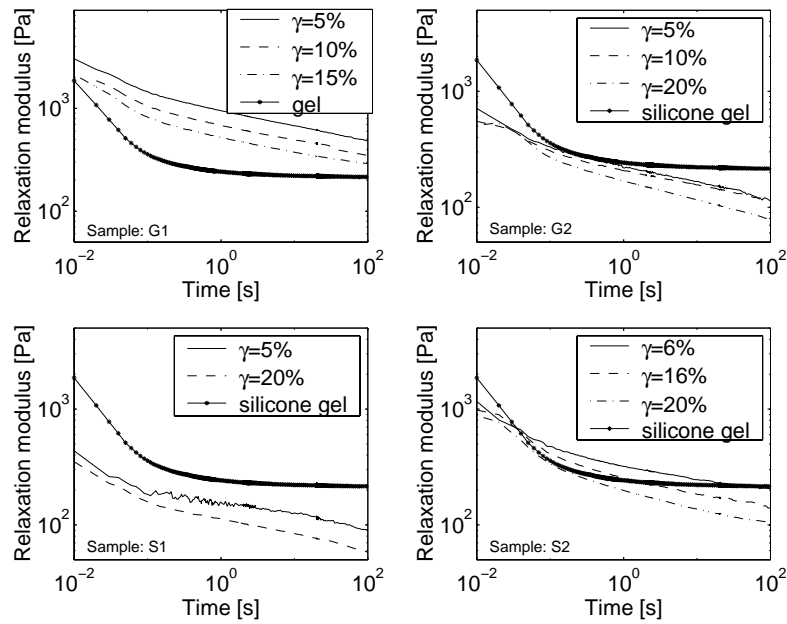


Figure 4.6: Stress relaxation results of porcine brain tissue ($n = 4$, $T = 38^\circ C$) compared with Sylgard 527 A&B silicone gel response (sample 1, $\gamma = 10\%$, $T = 24^\circ C$). Each figure shows a result of a single brain sample. G1 and G2: glued samples, S1 and S2: sand paper fixed samples. Moduli represent relaxation moduli for $t > 0.1$ s.

47.2 Pa at 10 s for these samples. The coefficient of variation (standard deviation normalised with mean value) remains within 35% for all times to 50 s.

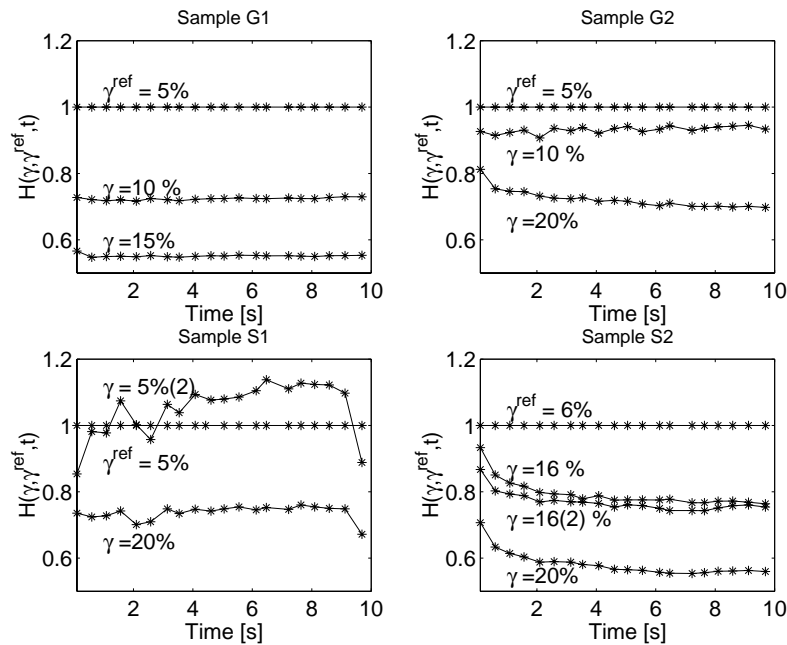


Figure 4.7: Time dependency of scaling function $H(t, \gamma_r, \gamma)$. Results of four samples shown in separate figures. Measurements marked (2) indicate repeated measurements.

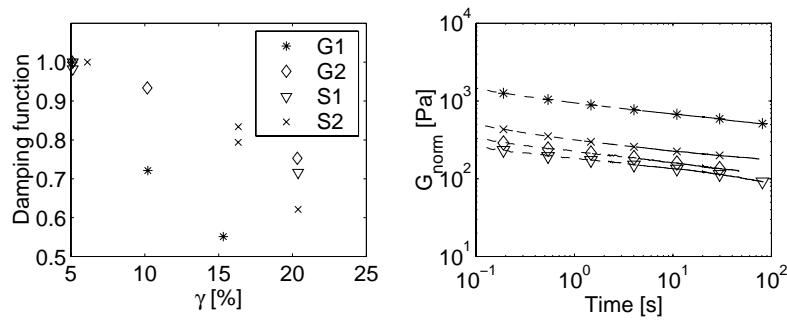


Figure 4.8: Overview relaxation moduli normalised to 5% (samples G1, G2 and S1) and 6% (sample S2) results (right) and damping functions of the four brain tissue samples tested, time averaged from 0.1 to 10 s (left). Double damping function values of S1 at 16% and S2 at 5%, indicate repeated measurements.

4.4 Discussion

The mechanical behaviour of brain tissue and silicone gel, a brain substitute material used previously in mechanical head models were compared in a strain and frequency range representing impact conditions. Oscillatory shear experiments were used to characterise the material within the linear range, the non-linear behaviour is characterised using shear stress relaxation experiments.

Silicone gel results

The results of the stress relaxation experiments at room temperature, show a 4.9% variation of shear modulus when strains varying from 10 to 50% were applied. To obtain an idea on the high frequency large strain behaviour of the silicone gel Dynamic Strain Sweeps were carried out at low temperatures. It was observed that increasing the strain from 1 to 50% leads a maximum variations of 8.1% and 2.3% for isothermal dynamic modulus and phase angle respectively. To assess the effective frequencies at which these low temperature results were valid, horizontal shift factors were determined from master curves that were obtained by applying TTS in the same temperature range as the DSS experiments. If we assume an increase of modulus by 8.3% due to a strain increase by 500% (from 1 to 50% strain) to be negligible, it can be concluded that Dow Corning Sylgard 527 A&B behaves as a linear viscoelastic solid for strains up to 50% and frequencies up to 461 Hz .

Repeatability/Reproducibility It has been shown that the room temperature material behaviour of the silicone gel was repeatable after low temperature, high strain, experiments (a maximum difference 1.4%).

The reproducibility of the stress relaxation experiments is checked by comparing the results obtained with two different samples, cured from two different batches. It was observed that differences were within 3.8%. Reproducing the TTS experiments with three different samples obtained from three different batches provided differences in horizontal shift factor values of less than 2%. Differences in dynamic modulus ranged from 20% to 0.2% for increasing frequencies. Differences in phase angle ranged from 15% to 0.2%. From these results it can be concluded that the reproducibility of the experiments was within 20%.

Comparison with literature Ivarsson *et al.* [71] performed a Dynamic Frequency Sweep on Dow Corning Sylgard 527 A&B silicone gel in a frequency range from 1 to 20 Hz ($\gamma_R = 0.65\%$, $T = 30^\circ C$, thickness, 3 mm). They found dynamic modulus values that were approximately 50% higher than ours. The phase angle was approximately 25% lower. A possible explanation for these differences might be different curing circumstances of the gel (temperature, time duration). Unfortunately no information was provided on the curing circumstances of the gel tested.

Brain Tissue results

Sample fixation When large strains were applied to the brain tissue, sample slip occurred when the standard smooth metal plates were used. The presence of sample slip could be observed best in stress relaxation experiments. When no slip precaution was taken, the measured time relaxation behaviour seemed to be dependent on the strain applied, i.e. strain-time factorisation was not valid anymore. It is believed that this effect is caused by sample slip since it was absent when either sandpaper or glue were used to fix the sample to the plate. It could be seen that the small strain results were in range of the results without slip precautions. This finding is supported by Arbogast *et al.* [4] who also did not find differences when a cyanoacrylate gel was applied in a dynamic frequency sweep experiment on porcine brain tissue. The large strain stress relaxation results did not reveal consistent differences between the fixation methods results. Both time relaxation behaviour as well as strain softening showed same tendencies. A drawback of using the adhesive, is the unknown adhesive thickness which could not be accounted for in the results. When sandpaper was used the thickness of paper and tape can easily be accounted for by zeroing the plate height with paper and tape attached to them. A drawback of sandpaper is that sample slipping might still be possible, but as indicated before it was believed that this was not the case in the results presented.

Adhesive fixed samples When comparing the damping functions and normalised moduli of the four brain tissue samples, the results of the G1 sample were found to deviate from the results of the other samples. This deviation might have been caused by a relatively thick glue layer present at G1, that could not be accounted for in the data processing. Since the glue behaves as a rigid solid when compared to the very compliant brain tissue, the real brain sample thickness will be lower than the measured plate distance. As a result the reported shear strain, γ_R , will be lower than the real strain at the samples edge (see equation (4.1)). For this reason the damping function values of sample G1, are valid at higher strains than shown in Figure 4.7. Furthermore the reported shear modulus will also be higher than in reality (see equation (4.3)) [164]. This is apparent in Figure 4.7. For this reason the results of sample G1 will not be considered in the further discussion.

Sandpaper For the sandpaper fixed samples, S1 and S2, measurement repeatability was investigated. When the 5% measurement of sample S1, was repeated, a 1.8% difference of the damping function was found. For sample S2 the 16% measurement was repeated after the 20% strain measurement and a 5.0% difference in damping function was found. Further more the damping function value of the repeated measurement were higher than the value at 20% strain, indicating that the shear softening observed cannot be caused by structural sample damage due to the high strains applied.

Time-strain factorisation In the constant strain part (i.e. after $t=0.1$ s) of the log-log relaxation plots, the curves for different strain values have a tendency to be

parallel. This suggests that the stress relaxation modulus can be separated into a strain and a time dependent part. It was estimated that the maximum error made by assuming time-strain factorisation to be valid is on the order of 26% and 13% if the 0.1s result is omitted. However, no final conclusions on the applicability of strain time factorisation could be drawn yet, since the number of samples is too low to illustrate statistical significance. Our findings are supported by findings of Prange *et al.* [122], who concluded that time-strain factorisation could be performed on their measurement results.

With respect to the stress dependent behaviour it was noted that all brain tissue sample tested exhibit shear softening when strains up to 20% were applied. The average shear softening equals 30% (n=3). The spread between samples given by the coefficient of variation equals 23%. The presence of shear softening was also found by Prange *et al.* [122]. Arbogast *et al.* [7] presented shear moduli at $t=60$ s for grey and white matter. These data corresponded to an average shear softening of approximately 30% when 5% strain was taken as reference strain, as done in this paper.

The spread of the normalised relaxation moduli, characterising the time dependent behaviour, equals 35% (coefficient of variation, n=3). It was also observed that the relaxation modulus does not reach a plateau value after 100 s. This is not uncommon for biological tissues; Fung for instance investigated the creep behaviour of muscle tissue under tension (i.e. he applied a constant stress and measured the resulting strain) and did not find a plateau value even after one day [53].

Comparison brain tissue and silicone gel

Stress-relaxation The large strain behaviour of both materials is compared in the stress relaxation results depicted in Figure 4.6. The relaxation modulus of the silicone gel lies within the spread of the brain sample results. Nevertheless two differences can be seen. First, strain dependent shear softening, found in brain tissue, is absent in the silicone gel results. Second, the time dependent relaxation behaviour differs. The modulus of silicone gel shows a plateau value whereas the brain tissue does not. Also the silicone gel relaxation modulus decreases faster than the one of brain tissue.

High frequency behaviour For assessing the large strain, high frequency behaviour of the brain tissue, use can be made of the fact that time-strain factorisation seems to be valid. This implicates that the large strain viscous behaviour can be derived completely from small strain oscillatory experiments. This is also true for silicone gel, since the material behaviour of the silicone gel proved to be independent of strain for strain values of at least 50%. For obtaining insight in the high frequency behaviour of brain tissue and silicone gel in the linear strain range, it has been shown before that Time Temperature Superpositioning can be applied [27][120]. A summary of the small strain results is provided in Figure 4.9 which contains all silicone gel data, brain tissue data and data obtained from [27].

It can be concluded that, at 0.1 Hz, the phase angle of silicone gel lies at the lower boundary of the brain tissue samples range. It stays within range for frequencies

between 0.1 and 1 Hz . For frequencies exceeding 1 Hz , the phase angle becomes higher than the one of brain tissue. For the reasons mentioned above, it can be concluded that also at finite strains, more viscous damping will be present in the silicone gel response.

The small strain dynamic modulus of the silicone gel is higher than the modulus of brain tissue for frequencies above 25 Hz . Due to the shear softening behaviour of the brain tissue, it can be expected that for large strains the modulus will be overestimated even more by the silicone gel. Furthermore the non-linear strain behaviour of brain tissue, in principle, might lead to multiple dynamic states during a certain excitation, while this will not be the case in the linear silicone gel (see e.g. [106]).

Methods

Strain field the large strain experiments were conducted on a rotational viscometer. As a result a non-homogeneous strain field will be present between the plates. The shear strain increases linearly from zero at the centre of the plate, to a maximum value at the plate edge. As long as the material behaves linearly elastic, as for the silicone gel, the computed relaxation modulus represents the true material property. For the large strain relaxation experiments on the brain tissue, the computed modulus represents some average over the strain range imposed on the material. Correction for non-homogeneous strain fields during stress-relaxation experiments is possible without assuming a specific type of constitutive equation [138]. However the application of this correction requires measurements at smaller strain intervals than presented here.

Inertia effects In deriving material behaviour from the experimental data it is assumed that inertia effects are absent in the samples. For the Dynamic Frequency experiments, this was checked using theory found in [21]. The torque measured, which involves inertia to some extent, will be called T_i . The torque to be expected from quasi-static theory, i.e. without inertia effects, will be called T_{qs} . It can be shown

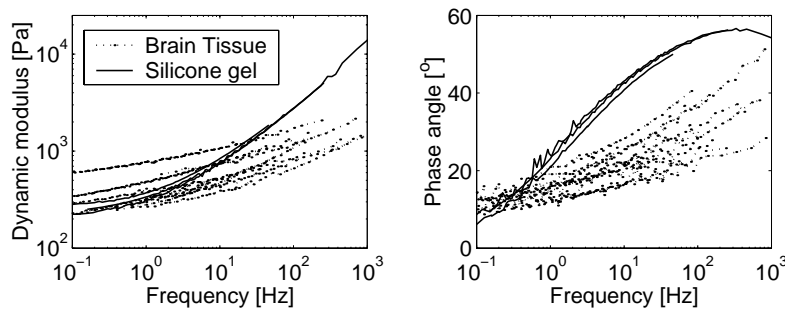


Figure 4.9: Comparison of small strain ($\gamma = 1\%$) master curves for porcine brain tissue ($n=9$) and silicone gel ($n=3$). Dynamic modulus (left) and phase angle (right).

that,

$$T_i = \frac{h\alpha}{\sin(h\alpha)} T_{qs} \quad \text{where} \quad \alpha = \sqrt{\frac{\omega^2 \rho}{G_d}} \quad (4.11)$$

and ω is the angular frequency, ρ the mass density, G_d the dynamic modulus and h the sample height. Checking in Figure 4.4 at the most suspicious result, i.e. when the actual frequency used in the experiment is at maximum and the dynamic modulus is at minimum (i.e. at $\omega = 100$ rad/s, $f = 16$ Hz), reveals moduli varying between 400 and 1200 Pa (approximately). Applying a mass density of 1000 kg/m (estimate) and thickness varying from 2.3 mm to 3.6 mm, provides errors ranging from 2.2% to 5.4% in the torque measured. For the stress relaxation experiments the inertia effects at 0.1 s are estimated by assuming a frequency of 10 Hz in equation (4.11). The maximum overestimation of the torque then equals 2.9%.

Limitations of current research

In-vitro versus in-vivo The main limitation of this kind of research is the fact that *in-vitro* brain tissue was used. Changes between living tissue and post-mortem tissue will occur due to absence of e.g. pressurization of the vascular network inside the brain tissue. With current test methodology it is impossible to assess the effect of these changes on the mechanical behaviour. Furthermore, the mechanical properties of brain tissue will change after death due to autolytic processes. Although inevitable, this effect can be reduced by proper sample handling. In this research we minimised these effects by minimising time between sacrifice and end of the experiments. Furthermore the samples were stored refrigerated, submerged in a physiological solution. And finally, in the TTS measurements the low temperature measurements were performed first. Peters *et al.* [120] showed that repeating a DFS at $\gamma_R = 1\%$, 110 minutes after the start of the TTS experiments, provided differences less than 10% in both dynamic modulus and phase angle.

Statistical significance The results presented, are obtained using a very limited amount of samples. This is especially true for the brain tissue samples where a large spread in measurement results could be observed. For this reason it has been chosen to present the results as is, i.e. without performing statistical post processing on the data. The results should therefore be interpreted in terms of trends rather than absolute values.

Measurement accuracy In determining the damping functions of brain tissue, a strain value of 5% was chosen as reference strain. To obtain the true damping function, $h(\gamma)$, γ_R^{ref} should be chosen in the linear range of the material. For brain tissue this means below 1% strain [27]. Unfortunately, in our relaxation experiments, the torque signal displayed too much measurement noise for strains below 5%, attributed to the fact that the signal was close to the lower measurement limit of the viscometer.

When large shear strains are applied upon a body, the resulting stress will not be a shear stress only, but a normal force will be present also. However, since a constant plate distance was used the experiment is still a simple shear test (with a shear strain depending on the radius). It proved to be impossible to determine the normal force during the large strain experiments. Since the normal force level was within the noise level of our normal force transducer in our viscometer (0.1 mN). For this reason the use of a more accurate rheometer is recommended for future research.

4.5 Conclusions

In this study, the large strain behaviour of Dow Corning Sylgard 527 A&B silicone gel was compared with the one of porcine brain tissue. The non-linear behaviour was characterised using stress relaxation experiments. It was shown that silicone gel behaves as a linear viscoelastic solid for strains up to 50% and frequencies up to 461 Hz (less than 8% strain stiffening). Brain tissue exhibits shear softening (30% at 20% strain) and it seems that the time dependent behaviour of brain tissue does not depend on the strain level. This implicates that the large strain time dependent behaviour of both materials can be derived completely from small strain oscillatory experiments and application of the Time Temperature Superpositioning Theory. From these it has been shown that, for frequencies above 1 Hz , the phase angle of silicone gel increases stronger with frequency than the phase angle of brain tissue. For this reason it is believed that silicone gel will not predict the response of brain tissue exactly in a physical head model. This is due to increased viscous material damping at high frequencies and absence of shear softening in the silicone gel. However, for trend studies and benchmarking of numerical models the gel can be a good alternative.

4.6 Acknowledgments

The authors would like to thank TNO Prins Maurits Laboratory and Ford Motor company for their financial support to this research and B. de Wit of abattoir de Wit Geldrop BV, for providing the porcine brain tissue.

Chapter 5

A non-linear viscoelastic material model for brain tissue

A non-linear viscoelastic material model for describing the dynamical behaviour of brain tissue is presented. The model is based on a generalised Maxwell model. A multiplicative decomposition of the deformation gradient tensor into an elastic and an inelastic part has been applied. The inelastic, time dependent behavior is described with a simple Newtonian law that acts on the deviatoric stress contribution only. The elastic part is modelled by a, non-linear, second-order Mooney-Rivlin model¹. In both inelastic and elastic parts deviatoric and volumetric stress contributions are separated. A rotation invariant strain update law for the inelastic right Cauchy-Green deformation tensor is derived using kinematics only. For time integration, the improved Euler method (Heun's method) is used in order to obtain adequate accuracy at time steps commonly used in explicit impact simulations. Finally, the biofidelity of the model has been tested by simulation of the stress relaxation experiments presented in Chapter 4.

¹Parts on strain dependent behaviour are also presented in: Brands, D.W.A, Bovendeerd, P.H.M., and G.W.M. Peters (2000): "Finite shear behaviour of brain tissue under impact loading", *ASME-WAM, Conf. on Crashworthiness, Occupant Protection and Biomechanics in Transportation Systems*, AMD-Vol. 246/BED- 49, pp.175-188.

5.1 Introduction

In the two previous chapters the mechanical behaviour of brain tissue under shear strain loading has been determined experimentally for frequencies up to 1000 Hz and strains up to 20%. It has been shown that for small strains the material behaves like a linear viscoelastic solid. In stress relaxation experiments, it was observed that the material exhibits shear softening. i.e. decreasing shear stiffness as a function of strain applied. Furthermore, the time dependent behaviour seems to be independent of the strain applied. In this chapter, a non-linear viscoelastic material model is presented that can describe the phenomena observed experimentally. First a rather general formulation of the model is given after which constitutive choices are made. Relevant material parameters are identified and fitted to experimental data. Next, the numerical solution of the equations in the time domain will be treated. Finally the model will be tested by simulating the stress relaxation experiments presented in previous section.

5.2 General formulation of the model

The basic idea behind the constitutive modeling is a generalised multi-mode Maxwell model for a solid, in which the Cauchy stress is additively composed in an elastic part, σ_0 , and one or more viscoelastic parts, σ_i (Figure 5.1). First, theory valid for a single mode will be presented. Then, the extension to a multi-mode model will be presented.

5.2.1 Multiplicative strain decomposition

For an arbitrary material element in a loaded configuration, C_t , the local actual deformation with respect to a predefined reference state, C_0 , is determined by the deformation gradient tensor \mathbf{F} (see Figure 5.2). The supposition is made that the

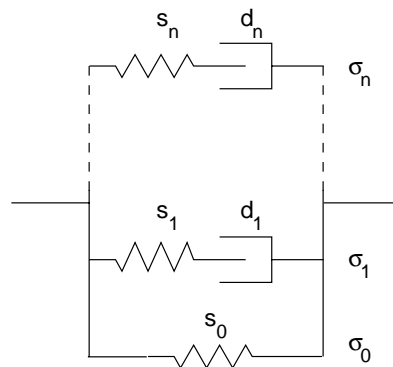


Figure 5.1: A spring-dashpot model as a mechanical analog of the constitutive model. S_0 to S_n are (non-linear) springs, d_1 to d_n are (linear) dashpots.

deformation gradient tensor can be split multiplicatively into an elastic part, F_e , and an inelastic part, F_p (as is done in e.g. [81]),

$$F = F_e \cdot F_p \tag{5.1}$$

The inelastic contribution refers to the deformation (with respect to the reference state), of the relaxed stress-free configuration, C_p , which is determined as a fictitious state that would be recovered instantaneously when all loads were removed from the material element considered. The velocity gradient tensor, $L = \dot{F} \cdot F^{-1}$, can be decomposed additively into an elastic part, L_e and an inelastic part, L_p ,

$$L = L_e + L_p \tag{5.2}$$

in which,

$$L_e = \dot{F}_e \cdot F_e^{-1} \text{ and } L_p = F_e \cdot \dot{F}_p \cdot F_p^{-1} \cdot F_e^{-1} \tag{5.3}$$

Both parts of the velocity gradient tensor can be decomposed additively as,

$$L = D + \Omega \tag{5.4}$$

in which $D = \frac{1}{2}(L + L^c)$ represents the symmetric rate of deformation tensor (A^c denotes the conjugate of tensor A) and $\Omega = \frac{1}{2}(L - L^c)$, the skew-symmetric spin tensor. Application of this decomposition to the elastic part, L_e , yields,

$$D_e = \frac{1}{2}(L_e + L_e^c) \text{ and } \Omega_e = \frac{1}{2}(L_e - L_e^c) \tag{5.5}$$

The inelastic part of the velocity gradient tensor, L_p , can be decomposed likewise into D_p and Ω_p . However, this decomposition does not provide a unique fictitious stress free state, C_p , since rigid-body rotation can be assigned to F_p as well as to F_e . Uniqueness is achieved by requiring that the inelastic deformation occurs spin free [81], i.e.

$$\Omega_p = 0 \tag{5.6}$$

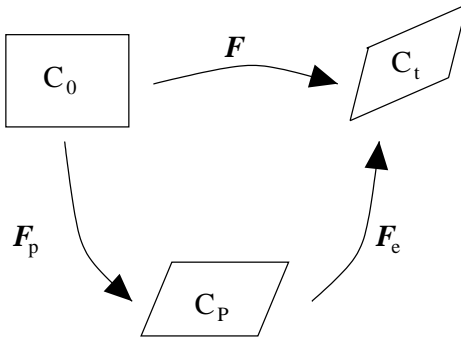


Figure 5.2: Graphical representation of the multiplicative decomposition of the deformation gradient tensor F . A inelastic part F_p transforms the reference state C_0 to the, fictitious, stress free state C_p while the elastic part F_e transforms the stress free state, C_p , to the deformed state C_t .

Deformation update For numerical implementation of the model, it is necessary to describe the time evolution of the elastic and inelastic contributions to the complete deformation. For this reason an evolution law will be derived based on kinematics only. The inelastic right Cauchy-Green tensor, C_p , is defined as,

$$C_p = \mathbf{F}_p^c \cdot \mathbf{F}_p = \mathbf{F}^c \cdot \mathbf{B}_e^{-1} \cdot \mathbf{F} \quad (5.7)$$

in which B_e represents the, objective, elastic Finger tensor. Taking its time derivative yields,

$$\dot{C}_p = -\mathbf{F}^c \cdot \mathbf{B}_e^{-1} \cdot [\dot{\mathbf{B}}_e - \mathbf{B}_e \cdot \mathbf{F}^{-c} \cdot \dot{\mathbf{F}}^c - \dot{\mathbf{F}} \cdot \mathbf{F}^{-1} \cdot \mathbf{B}_e] \cdot \mathbf{B}_e^{-1} \cdot \mathbf{F} \quad (5.8)$$

Application of the definition $L = \dot{\mathbf{F}} \cdot \mathbf{F} = \mathbf{\Omega} + \mathbf{D}$, and the assumption of spin free inelastic deformation, $\mathbf{\Omega} = \mathbf{\Omega}_e$, $\mathbf{\Omega}_p = \mathbf{0}$, provides,

$$\dot{C}_p = -\mathbf{F}^c \cdot \mathbf{B}_e^{-1} \cdot [\overset{\circ}{\mathbf{B}}_e - \mathbf{B}_e \cdot \mathbf{D} - \mathbf{D} \cdot \mathbf{B}_e] \cdot \mathbf{B}_e^{-1} \cdot \mathbf{F} \quad (5.9)$$

in which, $\overset{\circ}{\mathbf{B}}_e$ equals the objective Jaumann rate of B_e .

$$\overset{\circ}{\mathbf{B}}_e = \dot{\mathbf{B}}_e - \mathbf{\Omega}_e \cdot \mathbf{B}_e - \mathbf{B}_e \cdot \mathbf{\Omega}_e^c \quad (5.10)$$

After some rewriting the invariant evolution equation is derived as,

$$\dot{C}_p = 2\mathbf{C}_p \cdot \mathbf{F}^{-1} \cdot \mathbf{D}_p \cdot \mathbf{F} \quad (5.11)$$

This evolution equation is insensitive for large rigid-body rotations and therefore will be used for updating C_p numerically in the time integration procedure.

5.2.2 Constitutive assumptions

Brain tissue behaves like a nearly incompressible solid. Therefore, the Cauchy stress is split into a deviatoric part, $\sigma^d = \sigma - \frac{1}{3}\text{trace}(\sigma)\mathbf{I}$, and a volumetric part, σ^v , that depends on hydrostatic compression only,

$$\sigma = \sigma^d + \sigma^v \quad (5.12)$$

Inelastic behaviour The time dependent behaviour of a viscoelastic mode, is governed by the inelastic rate of deformation, D_p , and modelled as simple Newtonian with viscosity, η_s ,

$$D_p = \frac{\sigma^d}{2\eta_s} \quad (5.13)$$

Elastic behaviour The elastic behaviour is modelled using an isotropic hyperelastic formulation. In such formulation, the Cauchy stress is derived from a strain energy density function (SED), $W(B_e)$. For isotropic materials this function can be written in rotation invariant quantities of the elastic Finger tensor $I_{1,2,3}$,

$$W(B_e) = W(I_1, I_2, I_3) \quad (5.14)$$

with,

$$\begin{aligned} I_1 &= \text{trace}(\mathbf{B}_e) \\ I_2 &= \frac{1}{2} [\text{trace}(\mathbf{B}_e)^2 - \text{trace}(\mathbf{B}_e^2)] \\ I_3 &= \det(\mathbf{B}_e) \end{aligned} \quad (5.15)$$

For obtaining a consistent separation of deviatoric and volumetric parts in the Cauchy stress tensor, the SED is formulated in a separated isochoric part, \bar{W} and a volumetric part, W_v ,

$$W = \bar{W}(\bar{I}_1, \bar{I}_2) + W_v(I_3) \quad (5.16)$$

In this equation, $\bar{I}_{1,2} = I_{1,2}(\bar{\mathbf{B}}_e)$ with $\bar{\mathbf{B}}_e$, the isochoric elastic Finger tensor,

$$\bar{\mathbf{B}}_e = J_e^{-2/3} \mathbf{B}_e \quad (5.17)$$

in which, $J_e = \det(\mathbf{F}_e)$, represents the normalised volume of the elastic part of the deformation. The resulting Cauchy stress can be written as,

$$\boldsymbol{\sigma} = \frac{2}{\sqrt{I_3}} \left[\frac{\partial \bar{W}}{\partial \bar{I}_1} \bar{\mathbf{B}}_e^d - \frac{\partial \bar{W}}{\partial \bar{I}_2} (\bar{\mathbf{B}}_e^{-1})^d \right] + 2\sqrt{I_3} \frac{\partial W_v}{\partial I_3} \mathbf{I} \quad (5.18)$$

in which $\bar{\mathbf{B}}_e^d$ equals the deviatoric part of the isochoric elastic Finger tensor. Note that the first part of the stress, in the square brackets, is completely deviatoric whereas the second part occurs by the hydrostatic deformation only.

SED equation (5.16) can be rewritten as a general series approximation,

$$W = \sum_{i+j=1}^N C_{ij}(t) (\bar{I}_1 - 3)^i (\bar{I}_2 - 3)^j + \sum_{k=1}^M C_k(t) (I_3 - 1)^k \quad (5.19)$$

The parameters N and M determine the general character of the material behaviour. For simple shear, it has been shown in Chapter 4 that brain tissue exhibits shear softening. For this reason it is required that $N > 1$. The simplest choice then becomes $N = 2$, thus obtaining a second-order Mooney-Rivlin SED. Miller *et al.* [96] successfully fitted results of unconfined compression experiments with brain tissue with of $N = 2$ and $i \neq j$. In [29], we did show that shear softening during simple shear could be predicted well using negative second-order constants. The isochoric part of the SED then becomes,

$$\bar{W} = C_{10}(\bar{I}_1 - 3) + C_{01}(\bar{I}_2 - 3) + C_{20}(\bar{I}_1 - 3)^2 + C_{02}(\bar{I}_2 - 3)^2 \quad (5.20)$$

This yields the deviatoric part of the Cauchy stress tensor,

$$\begin{aligned} \boldsymbol{\sigma}^d &= \frac{2}{J_e} \{C_{10} + 2C_{20}(\bar{I}_1 - 3)\} \bar{\mathbf{B}}_e^d \\ &\quad - \frac{2}{J_e} \{C_{01} + 2C_{02}(\bar{I}_2 - 3)\} (\bar{\mathbf{B}}_e^{-1})^d \end{aligned} \quad (5.21)$$

Only few literature data on linear viscoelastic hydrostatic behaviour of brain tissue is present. Furthermore it is shown in Chapter 2 that significant damping due

to hydrostatic deformation occurs at high frequencies only. For this reason, the volumetric part of the stress is modelled as simple as possible as,

$$\boldsymbol{\sigma}^v = K(J_e - 1)\mathbf{I} \quad (5.22)$$

with K being the bulk modulus.

Note that, as the Cauchy stress is expressed in terms of (invariants of) the elastic Finger tensor, conservation of objectivity is guaranteed when indeed the spin is attributed to the elastic deformation, as done here. Furthermore, since a true hyper elastic material law is used for the Cauchy stress, the elastic part of the deformation will cause no energy dissipation at repeated loading and unloading of the elastic part of the deformation. So the inelastic part completely controls energy dissipation, as required.

5.2.3 Multi-mode description

The theory presented is extended to a multi-mode model by applying the strain decomposition in each mode i separately. For each mode, the modal strain decomposition will be applied in constitutive equations (5.21) and (5.22) to provide the viscoelastic modal stress contribution σ_i . The elastic contribution, σ_0 is determined by substituting the total Finger tensor, \mathbf{B} , for \mathbf{B}_e in equations (5.21) and (5.22). Finally the complete Cauchy stress can be obtained by simply adding all modal stress contributions,

$$\boldsymbol{\sigma} = \boldsymbol{\sigma}_0 + \sum_{i=1}^n \boldsymbol{\sigma}_i \quad (5.23)$$

5.3 Determination of brain tissue material parameters

The experimentally found time-strain separability of the shear stress behaviour will be used to determine the material parameters for brain tissue. The time dependent behaviour is determined using small strain oscillatory experiment data while the strain dependent behaviour is obtained from large strain stress relaxation experiments.

The material data shows a large spread caused by measurement noise as well as biological variation of the various samples used. However trends observed were present for all samples. To eliminate the spread by biological variation, material parameters will only be fitted on experimental data of the single sample that has been used in both small strain oscillatory experiments as well as large strain stress relaxation experiments (sample G2 in Chapter 4). The bulk behaviour was not determined in current experiments and will be determined from literature data on ultrasound experiments [45; 61; 83].

5.3.1 Small strain experiments: Multi-mode Maxwell model

For small shear strains, the non-linear viscoelastic constitutive equations used reduce to a multimode Maxwell model. The Maxwell model can be presented in terms of storage modulus, G' and loss modulus, G'' ,

$$G' = G_0 + \sum_{i=1}^n G_i \frac{\lambda_i^2 \omega^2}{1 + \lambda_i^2 \omega^2} \tag{5.24}$$

$$G'' = \sum_{i=1}^n G_i \frac{\lambda_i \omega}{1 + \lambda_i^2 \omega^2}$$

in which i indicates the contribution of the separate modes, while n is the number of modes used. For a given number of modes, the optimal sets of relaxation times, λ_i and shear moduli G_i are determined from linear viscoelastic data obtained from small strain oscillatory tests, using a Levenbergh-Marquardt fit algorithm [170]. The equilibrium mode, G_0 , cannot be obtained from the oscillatory data since the lowest frequency used is too large, as can be seen by the absence of a plateau value for G' on the lower frequency range in Figure 5.3. For this reason, G_0 was determined from the stress relaxation experiments (refer to page 73).

The experimental data as well as the fit obtained with a four mode Maxwell model are shown in Figure 5.3. The figure shows that the material behaviour is not fitted well at low frequencies in that G' is underestimated. A possible explanation will be provided in the discussion in section 5.5.3.

Relation with non-linear model

The relation between the linear Maxwell relaxation moduli G_i and the non-linear model parameters $C_{10,i}$ and $C_{01,i}$ can be found by linearising constitutive equation (5.21) for simple shear. This results in,

$$(C_{10,i} + C_{01,i}) = 0.5G_i \tag{5.25}$$

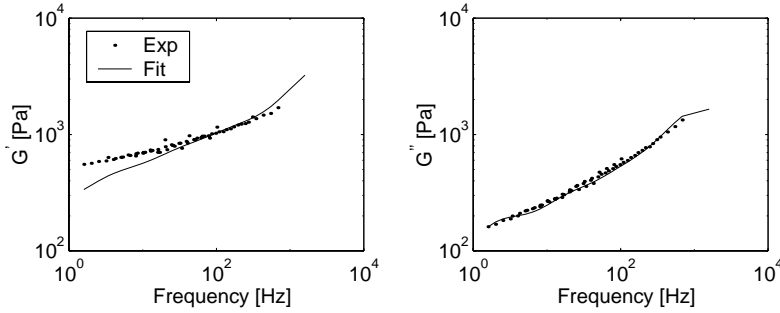


Figure 5.3: Storage and loss modulus G' and G'' from sample G2 in Chapter 4 together with 4 mode Maxwell fit. During fits, G_0 set to value obtained from Stress Relaxation experiments.

With respect to the inelastic behaviour it is assumed that the inelastic part of the deformation is governed by linear Newtonian behaviour. Viscosity, $\eta_{s,i}$ now can be found using,

$$\eta_{s,i} = G_i \lambda_i \quad (5.26)$$

5.3.2 Large strain stress relaxation experiments

The large strain shear behaviour of porcine brain tissue was characterised using a rotational plate-plate viscometer. The strain field present between the plates is non-homogeneous. As a result, apparent material parameters were measured, i.e. parameters valid for some average strain present between the plates. A correction method by Soskey and Winter [138] will be used to obtain the true material parameter, $G(t, \gamma_R)$. The approach is valid for stress relaxation experiments in a rotational plate-plate viscometer.

Method

Based on kinematics only, the true relaxation modulus, $G(t, \gamma_R)$, can be obtained from the experimentally determined apparent modulus, $G_a(t, \gamma_R)$, via,

$$G(t, \gamma_R) = G_a(t, \gamma_R) \left(1 + \frac{\partial \ln G_a(t, \gamma_R)}{4 \partial \ln \gamma_R} \right) \quad (5.27)$$

In Chapter 4 the relaxation modulus was successfully factorised into a time dependent part, the linear relaxation modulus, $G(t)$, and a strain dependent part, $h(\gamma)$, the so-called damping function. Applying this to equation (5.27) leads to,

$$G(t, \gamma_R) = h_a(\gamma_R) \left(1 + \frac{\partial \ln h_a(\gamma_R)}{4 \partial \ln \gamma_R} \right) G(t) \quad (5.28)$$

with $h_a(\gamma_R)$, the apparent damping function that is obtained directly from the stress relaxation data. Thus, when time strain separation is valid, only the apparent damping function needs to be corrected to obtain the real relaxation modulus.

Damping function

For simple shear the damping function of a hyper elastic material can be written as,

$$h(\gamma) = \frac{\frac{\tau(\gamma)}{\gamma}}{\lim_{\gamma_0 \rightarrow 0} \frac{\tau(\gamma_0)}{\gamma_0}} = \frac{2 \left(\frac{\partial W(\gamma)}{\partial I_1} + \frac{\partial W(\gamma)}{\partial I_2} \right)}{\lim_{\gamma_0 \rightarrow 0} 2 \left(\frac{\partial W(\gamma_0)}{\partial I_1} + \frac{\partial W(\gamma_0)}{\partial I_2} \right)} \quad (5.29)$$

with, γ the shear strain, $\tau(\gamma)$ the shear stress, I_1 and I_2 the first and second invariant of the Finger tensor \mathbf{B} , and $W(\gamma)$ the hyper-elastic strain energy density function for simple shear. Substituting SED equation (5.20) into equation (5.29) while applying Finger tensor \mathbf{B} for simple shear, and $I_1 = I_2 = \gamma^2 + 3$, gives,

$$h(\gamma) = 1 + 2\gamma^2 f_{nls} \quad \text{and} \quad f_{nls} = \frac{C_{02} + C_{20}}{C_{01} + C_{10}} \quad (5.30)$$

in which f_{nls} will be referred to as non-linear shear parameter. This function is fitted to the experimentally found damping functions, $\overline{H}(\gamma_R, \gamma_R^{ref})$, obtained in Chapter 4, using a Nelder-Mead simplex (direct search) method [89]. This fit is used to correct the data using equation (5.27) and equation (5.30) has been fitted again to the corrected data to obtain the true non-linear shear parameter, f_{nls} . The quality of the fitted data is quantified by the average error of the fit at each experimental data point and the standard deviation of the error.

Fit results

To obtain realistic fits for the damping function, (i.e. $\lim_{\gamma \rightarrow 0} h(\gamma) = 1$), the damping function value at 5% strain is assumed to be valid at 1% strain also. The left plot in Figure 5.4 shows the damping function, fitted on the experimental data of sample G2. The non-linear shear parameter, f_{nls} , equals -2.99. The mean fit error \pm standard deviation equals $3.0 \cdot 10^{-3} \pm 8.0 \cdot 10^{-3}$. The corrected experimental results in the right plot in Figure 5.4, show that the shear softening of sample G2 equals 37.1% at 20.3% strain. Fitting the second-order Mooney-Rivlin model to the corrected data provides $f_{nls} = -4.49$. The mean error equals $3.0 \cdot 10^{-3} \pm 8.6 \cdot 10^{-3}$, i.e. approximately 1% of the experimental values.

Determination equilibrium mode

As mentioned in section 5.3.1, the small strain equilibrium mode, G_0 , is determined from the stress relaxation results. It will be defined as the small strain relaxation modulus at $t = 0.5$ s, since the behaviour of brain tissue at later moments in time is not of interest in impact situations. Since the smallest strain used in the stress relaxation experiments, 5%, is outside the linear range of the material behaviour (refer to Chapter 3) the small strain modulus is obtained by rewriting equation (4.8)

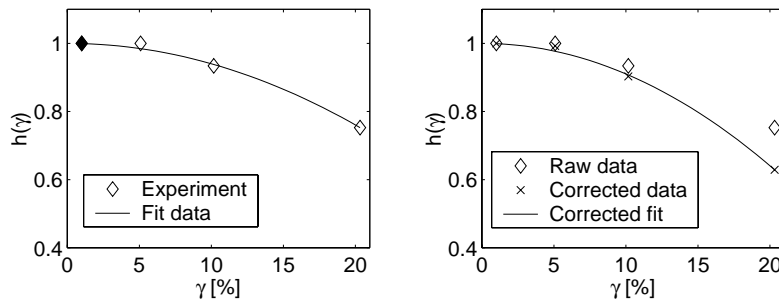


Figure 5.4: Correction for non-homogeneous strain field using second-order Mooney-Rivlin on results of sample G2 in [28]. Left: Fit results on uncorrected experimental data (filled diamond denotes copied 5% result). Right: Corrected data using 2nd order Mooney-Rivlin model.

as,

$$G(t) = \frac{G_a(t, \gamma = 5\%)}{h_a(\gamma = 5\%)} \quad (5.31)$$

with $h_a(\gamma = 5\%)$ obtained from equation (5.30) and $f_{nls} = -2.99$. This results in $G_0 = 255 \text{ Pa}$.

Relation with non-linear model

It is assumed that the experimentally determined non-linear shear parameter, f_{nls} , can be applied on the elastic part of every mode, i.e.,

$$\frac{C_{20,i} + C_{02,i}}{C_{10,i} + C_{01,i}} = f_{nls} \quad \text{for } i = 1 \text{ to } n \quad (5.32)$$

Note that applying this constant ratio for each mode, reduces the number of material parameters, but introduces a difference with the description of the stress in the experimental results. The value of the experimentally determined damping function is determined by the complete shear strain whereas the non-linear behaviour in the material model, is governed by the elastic part of the deformation. So time-strain separability is not guaranteed in the model.

To ultimately determine the material parameters $C_{10,i}$, $C_{01,i}$, $C_{20,i}$ and $C_{02,i}$, the ratios $f_{1,i} = \frac{C_{10,i}}{C_{01,i}}$ and $f_{2,i} = \frac{C_{20,i}}{C_{02,i}}$ have to be known. It is not possible to determine these from results of shear experiments. Miller and Chinzei [96] fitted a second-order Mooney-Rivlin model to results of low velocity, unconfined compression experiments on porcine brain tissue using $f_1 = f_2 = 1$. In the present study it is assumed that $f_{1,i} = f_{2,i} = 1$ for all modes $i = 0$ to n .

5.3.3 Bulk behaviour: Ultrasonic experiments

The hydrostatic behaviour was chosen to be purely elastic. As a consequence, the hydrostatic pressure will be attributed to the elastic stress part σ_0^v only,

$$K_0 = K \quad \text{and} \quad K_i = 0, \quad i = 1 \text{ to } n \quad (5.33)$$

From ultrasonic experiments, the velocity of dilatational waves in brain tissue, c_p , is known to be approximately 1550 m/s [45; 61; 83]. Using linear elastic theory, and knowing that the material is nearly incompressible (i.e. $K \gg G_i$), the bulk modulus is determined as,

$$K = c_p^2 \rho \quad (5.34)$$

in which mass density, ρ , equals approximately 1040 kg/m^3 for brain tissue. This provides a bulk modulus of 2.5 GPa .

Table 5.1 provides an overview of all material parameters fitted.

5.4 Numerical implementation

The material model is implemented in a Finite Element Code (MADYMO). First it is explained how time integration is performed in the existing code. Then the stress update routine utilising a predictor-corrector scheme, will be presented. Finally the accuracy of the model is investigated.

5.4.1 Time integration in MADYMO

The general outline of the MADYMO FEM integration scheme is presented in Figure 5.5 [147]. Nodal displacements at the next time step, $u(t+\Delta t)$ are predicted starting from the displacements at the current moment in time, $u(t)$. The integration cycle consists of four steps. In the first step deformation gradient tensors, $F(t)$, at the element integration point are computed from the nodal displacements, $u(t)$. The second step deals with the computation of the stresses at the element integration points, $\sigma(t)$. From these stresses, the internal nodal forces at the current time, $f_{int}(t)$, are obtained in the third step. Finally nodal accelerations at time, t are calculated by applying the momentum equilibrium equations. From these accelerations the nodal displacements

Table 5.1: Material parameters obtained from fitting the non-linear material model on brain tissue shear data (sample G2 in Chapter 4)

| Mode i | Maxwell parameters | | Non-linear parameters | | | Bulk modulus |
|-----------|--------------------|------------------|-----------------------|----------------|----------------|--------------|
| | G_i [Pa] | λ_i [ms] | f_{nls} [-] | f_1 [-] | f_2 [-] | K [GPa] |
| 0 | 255.3* | ∞ | -4.49 | 1 ⁺ | 1 ⁺ | 2.5 |
| 1 | 269.08 | 70.1 | -4.49 | 1 ⁺ | 1 ⁺ | 0 |
| 2 | 322.63 | 7.62 | -4.49 | 1 ⁺ | 1 ⁺ | 0 |
| 3 | 426.96 | 1.42 | -4.49 | 1 ⁺ | 1 ⁺ | 0 |
| 4 | 3299.4 | 0.122 | -4.49 | 1 ⁺ | 1 ⁺ | 0 |

* G_0 obtained from stress relaxation data using equation (5.31)

+ Constants chosen arbitrarily, could not be determined from shear experiments

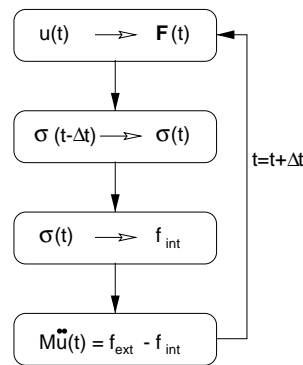


Figure 5.5: General layout MADYMO FEM time integration scheme, conform [147].

on the next moment in time, $u(t + \Delta t)$, are determined using an (explicit) Central Difference integration scheme. Then the complete sequence can start again for the next time increment.

5.4.2 Stress computation

The stress computation scheme needed for calculation of the Cauchy stress at present time, $\sigma(t)$, (step two in Figure 5.5), is provided in Figure 5.6. The following quantities should be known at the start of the current time, t : $\mathbf{F}(t - \Delta t)$, $\mathbf{C}_{p,i}(t - \Delta t)$, and $\sigma_i^d(t - \Delta t)$, stored in the previous time step and $\mathbf{F}(t)$, computed from the displacements, $u(t)$, computed from the momentum equilibrium equations at previous time step. This is generally true. However, the deformation and stress state at the start of the simulation should be specified. It is assumed that there is no initial deformation, i.e. $\mathbf{F}(0) = \mathbf{F}_{e,i}(0) = \mathbf{C}_{p,i}(0) = \mathbf{I}$, and no initial stress, $\sigma(0) = \mathbf{0}$.

The next steps in Figure 5.6 are straightforward, except for step 4. To determine $\mathbf{C}_{p,i}(t)$, an explicit time integration scheme, the so-called improved Euler method or Heun's method, is used. Explicit time integration is chosen because modelling the transient material behaviour during impacts requires many small time steps.

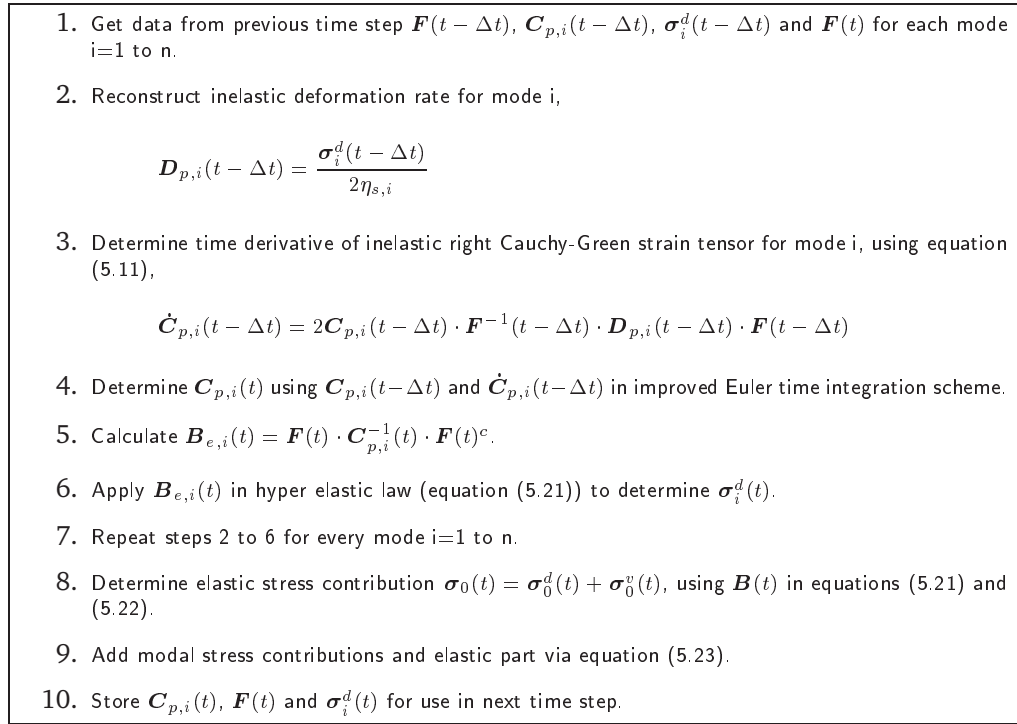


Figure 5.6: Stress computation scheme for determining the Cauchy stress at the current moment in time, $\sigma(t)$, using the non-linear viscoelastic material model (the second box in the general time integration scheme in Figure 5.5). n denotes the number of viscoelastic modes.

First an estimation of the inelastic right Cauchy-Green strain, $\tilde{C}_{p,i}(t)$, is made by using the Euler forward method,

$$\tilde{C}_{p,i}(t) = C_{p,i}(t - \Delta t) + \dot{C}_{p,i}(t - \Delta t)\Delta t \quad (5.35)$$

in which $\dot{C}_{p,i}(t - \Delta t)$ was obtained in step 3 using evolution equation (5.11). The predicted tensor, $\tilde{C}_{p,i}(t)$, is used in steps 5, 6, 2 and 3 in Figure 5.6 to determine a prediction of the deformation rate $\tilde{\dot{C}}_{p,i}(t)$. The predicted $\tilde{C}_{p,i}(t)$ then is corrected by applying the trapezoidal rule,

$$C_{p,i}(t) = C_{p,i}(t - \Delta t) + \frac{1}{2} \left(\dot{C}_{p,i}(t - \Delta t) + \tilde{\dot{C}}_{p,i}(t) \right) \Delta t \quad (5.36)$$

5.4.3 Accuracy of the time integration scheme

In this section it is investigated whether the accuracy of the improved Euler method is sufficient for modelling nearly incompressible materials, such as brain tissue, at time steps commonly used in impact simulations ($\Delta t = O(10^{-6})$ s). To do so, the stress update scheme of Figure 5.6 is implemented in MATLAB 5.3 [89]. Simple shear ($\gamma_0 = 20\%$) is applied step wise at $t = 0.5$ s and kept constant thereafter. A single mode model is used with shear modulus $G_1 = 2(C_{10} + C_{01}) = 1000$ Pa, $C_{20} = C_{02} = 0$, bulk modulus, $K_1 = 1$ GPa and time constant $\lambda_1 = 1$ s. In this section only results interesting for the accuracy analysis are shown. A complete overview of numerical and analytical results can be found in Appendix A.

The upper left plot in Figure 5.7 shows the computed shear stress versus time. The initial stress equals approximately 200 Pa and decreases in time. The slope of the semi-logarithmic plot equals -1 corresponding with the time constant applied. Two types of error appear in the stress results. The first type of error acts on the relaxation behaviour of the shear stress. The time history of the relative error in the shear stress, $\Delta E_{rel}(t)$, is defined as,

$$\Delta E_{rel}(t) = \frac{|\sigma_{num}(t) - \sigma_{th}(t)|}{\sigma_{th}(t)} \quad (5.37)$$

in which $\sigma_{num}(t)$ and $\sigma_{th}(t)$ represent the numerical and theoretical obtained shear stress histories respectively. The upper right plot in Figure 5.7 shows that the relative error, ΔE_{rel} decreases to approximately 1% when a time step of 0.01 s or less is used. The second error appears in the volumetric stress. Since simple shear is an isochoric deformation, the volumetric stress should be zero. It decreases quadratically with decreasing time step, as shown in the lower plot in Figure 5.7.

Discussion

The error in the volumetric stress is determined by the limited accuracy of the integration method used. For brain tissue, this error becomes relevant since the bulk modulus is approximately 10^6 times higher than the shear modulus. The residual volumetric stress at $\Delta t = 10^{-6}$ s, typical in automotive impact simulations, is determined by extrapolating the results in the lower plot Figure 5.7 and equals 10^{-5}

Pa . This error is on the order of 10^{-7} times the initial shear stress and is considered to be sufficiently small.

The error during stress relaxation is determined by ratio time step over time constant used. In the present simulation the time constant, λ , was set to 1 s . Taking a time step of 0.01 s yielded an error of 1%. This implies that the time step has to be chosen such that $\Delta t/\lambda < 0.01$ for accurate shear stress results. The smallest relaxation time for brain tissue equals $1.2 \cdot 10^{-4}\text{ s}$ (refer to Table 5.1 on page 75). This means that accurate solutions are indeed obtained when a time step of 10^{-6} s , common in impact simulations, is used.

An issue not discussed on is the objectivity of the stress formulation. Although this should be trivial, Nusholtz and Shi (1998) showed that in a commercially available explicit FE package, objectivity of the stress results during large rotations was not guaranteed to that date [113]. When undeformed solid elements were rotated by 4 revolutions, an artificial normal stress on the order of 9 GPa appeared (linear elastic material behaviour, $E = 200\text{ GPa}$ and $\nu = 0.3$). Applying this rotation provided a maximum error on the order of 10^{-7} Pa for the model presented in this section. This indicates correct objective behaviour. Different loading types such as cyclic loading and unloading, did not lead to different error causes than the ones discussed for the simple shear simulation in this section. For more information on these simulations the reader is referred to appendix A.

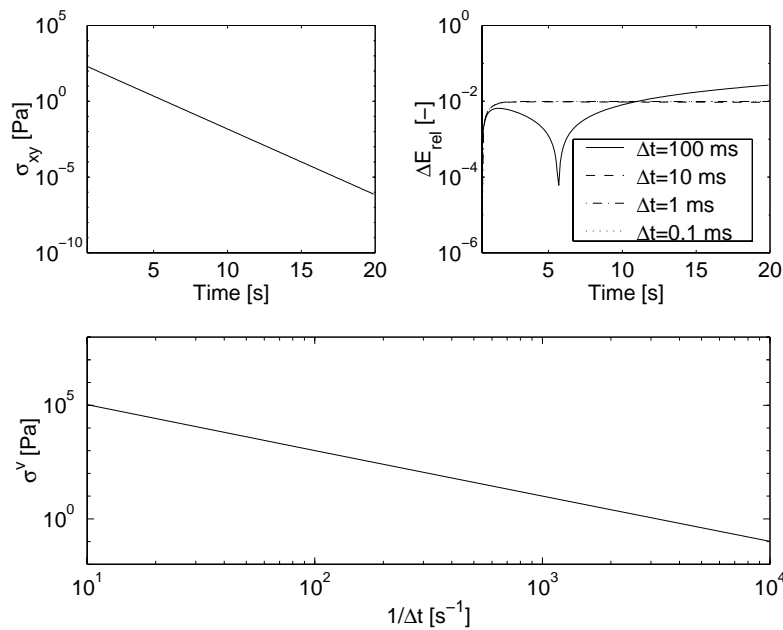


Figure 5.7: Results of simple shear stress relaxation simulation. Top left: Shear stress versus time. Top right: Relative error histories (ΔE_{rel} in equation (5.37)) in shear stress for various time steps. Bottom: Residual volumetric stress versus reciprocal time step.

5.5 Simulation of stress relaxation experiments

The time dependent behaviour of the material model is obtained from small strain experiments only, while all information on strain dependent behaviour comes from the constant strain phase of large strain stress relaxation experiments. In this section it is investigated whether the model predicts the stress relaxation experiments, presented in Chapter 4, including the transient phase.

5.5.1 Model description

A three-dimensional FE model of the rheometer experiments has been developed. Brain tissue constitutive behaviour is modelled using the material parameters in Table 5.1. The geometry of the brain sample is modelled by a quarter cylinder only with diameter 25 mm and thickness 2 mm, to reduce CPU time. Symmetry boundary conditions are applied on the cross-sectional planes. The lower plane is rotated according to the experimentally obtained rotation history obtaining the strain histories, reprinted in Figure 5.8, which are valid at the sample edge. The upper-plane is rigidly supported and the resulting torque along the axis of rotation is determined. The apparent stress is calculated from the resulting torque in the same manner as in the experimental results (refer to equation 4.3) for comparison.

Spatial discretisation is obtained using cubic elements with linear interpolation functions. To prevent mesh locking, likely to occur due to the nearly incompressible material behaviour, reduced spatial integration is used. Seven element layers are used in thickness direction whereas approximately twelve elements are used in radial direction. The time step used is determined via the Courant criterion (refer to equation 2.30) and equals $1.66 \cdot 10^{-7}$ s. This is approximately 10^{-3} times the smallest time constant and should provide accurate solutions.

5.5.2 Results

In Figure 5.8 the apparent shear stresses, experimentally obtained at 5, 10 and 20% maximum edge strain, are plotted together with the numerical results. The model peak stress values are over estimated by 12 to 23% during the transient part of the loading ($t < 0.1$ s) (ΔE_{peak} in Table 5.2). Then, during the subsequent relaxation phase, the stress decay is faster than in reality. The numerical results even drop

Table 5.2: Overview of the maximum relative differences between numerical results and experimental results. ΔE_{peak} : difference between peak values during transient loading part, ΔE_{relax} : maximum negative difference during relaxation, $\Delta E_{t=0.5s}$: difference at $t = 0.5$ s.

| Max. strain γ_0 [-] | ΔE_{peak} [%] | ΔE_{relax} [%] | $\Delta E_{t=0.5s}$ [%] |
|----------------------------|-----------------------|------------------------|-------------------------|
| 0.05 | 19.5 | 0.4 | 3.8 |
| 0.1 | 22.8 | 0.9 | 6.5 |
| 0.2 | 12.2 | 2.3 | 5.1 |

below the experimental results providing a maximum difference of 2.3% at 5% strain (ΔE_{relax} in Table 5.2). At the end of the simulation, at $t = 0.5$ s, no relaxation is present any more in the numerical stresses which are higher than the experimental results at that time by 4% at 10% strain ($\Delta E_{t=0.5s}$ in Table 5.2).

5.5.3 Discussion and conclusions

Stress relaxation experiments have been simulated including the transient loading part at times less than approximately 0.1 s. It could be observed that the model correctly predicts the overall behaviour of the brain tissue, i.e. the presence of shear softening and the stress relaxation. Nevertheless differences between experimental data and numerical results are present.

Relaxation behaviour During the transient phase of the loading, the model predicts higher stresses than found experimentally. Then, during subsequent relaxation, the stresses are described within 6% accuracy. However, after 0.1 s the predicted stresses decay faster and tends to reach a plateau value which is not present in the experimental results. Two causes can be found for this. Firstly, the equilibrium mode was fitted to the 0.5 s value. As a result there will be no relaxation from that moment of time on. Secondly, when the modal contributions to the relaxation behaviour are studied, it can be seen that the behaviour from 0.2 to 0.5 s is governed by a single mode only. This can be improved by using more modes in the model.

Peak values The differences in peak values during transient loading might be caused by the fact that the linear material parameters and non-linear parameters are derived from separate sets of experiments. The linear parameters were determined from a master curve constructed from several dynamic frequency sweep experiments at various temperatures (DFS). Subsequently, stress relaxation experiments (SR) were carried out from which the non-linear behaviour was taken as well as the small strain

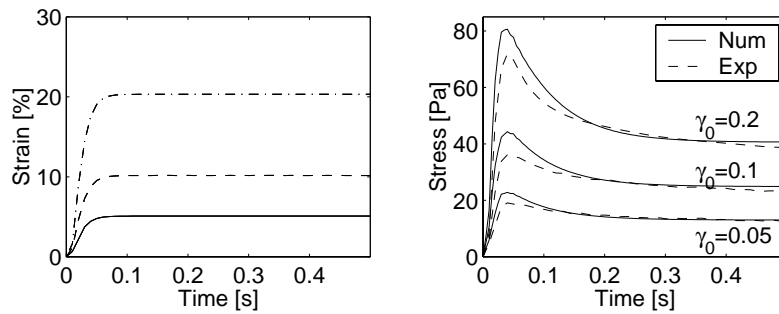


Figure 5.8: Simulation results of stress relaxation experiment at three strain levels versus experimental results (apparent stresses sample G2 in Chapter 4). Left: sample edge shear strain histories, Right: apparent shear stresses, Num = MADYMO result, Exp = Experiment.

equilibrium mode. In the process of performing these experiments, experimental data will be influenced by factors as material ageing and differences in humidity conditions, which always exist between separate experiments. A clue for the presence of such differences can be found by observing the trends of the errors while predicting DFS and SR experiments. The trends in the errors in the SR experiments are strain independent, i.e. overestimated initial stress followed by better prediction of long term behaviour. For this reason trends in the error in the DFS experiment should resemble those of the SR experiments, i.e. overestimated moduli at high frequencies and about correct ones at low frequencies. The opposite however is true, low frequency values of the elastic modulus are underestimated while high frequency values are approximately correct (refer to Figure 5.3). This indicates that the general stiffness of the brain tissue was higher during the DFS experiments than in the SR experiments.

Finally it should be mentioned that the time-strain separability, assumed in the derivation of the material parameters, has never been validated for times less than 0.1 s (i.e. frequencies above 10 Hz). Darvish and Crandall recently presented experimental results that indicate that for frequencies above 27 Hz , also time dependent non-linearities might be present in brain tissue [39].

5.6 Conclusion

In this chapter a non-linear viscoelastic material model for the large strain shear behavior of brain tissue in impact conditions has been presented. The inelastic, time dependent behavior is described with a simple Newtonian law that acts on the deviatoric stress contribution only. Based on the experimental data in Chapters 3 and 4, the deviatoric elastic part is modelled by a non-linear, second-order Mooney-Rivlin model. Since this experimental data did not provide information on potential anisotropic behaviour present in brain tissue [8; 123] isotropic material behaviour is assumed. However, anisotropic behaviour can be included in strain energy density equation (5.20). The hydrostatic part is assumed to be linear elastic. The model has been implemented in an explicit Finite Element code. Care has been taken that the numerical accuracy of the model suffices for predicting the behaviour of a nearly incompressible material such as brain tissue at large strains and large rotations expected during impact by using the improved Euler integration scheme for time integration of the inelastic deformation.

Material parameters have been determined from simple shear experiments presented in Chapters 3 and 4. In elaborating these parameters, time-strain separability was assumed to be valid. Linear parameters were determined from small strain oscillatory experiments, whereas the strain dependent non-linearity was determined from stress relaxation experiments. It was found that the strain dependent behaviour could be fitted well when negative second-order parameters, C_{20} and C_{02} were used. As a result negative stiffness can occur at strains exceeding the strain range for which the model has been fitted on. When the model is used during a transient simulation, this has to be kept in mind.

The ratios $\frac{C_{10}}{C_{01}}$ and $\frac{C_{20}}{C_{02}}$ could not be determined from the experimental data. This is a result of the fact that the first and second invariant of the elastic Finger tensor are equal to each other in simple shear. In principle, these ratios can be determined from unconfined compression experiments, available from literature [96]. However, a large spread exists between the experimental results obtained from different samples and also between various literature sources (refer to Figure 3.4 in Chapter 3). For this reason no efforts have been made in fitting the material parameters of our sample to the literature data. Instead the ratios $\frac{C_{10}}{C_{01}}$ and $\frac{C_{20}}{C_{02}}$ were set to 1 as done in [96].

The material model has been tested by simulation of brain tissue stress relaxation experiments including the transient part of the shear strain. It was found that during this transient part, the model over-predicts the stress values. In the constant strain phase, the strain dependent behaviour of brain tissue is described quite well although differences were present in relaxation behaviour. It is expected that these results can be improved by putting more effort in fitting material parameters.

It can be concluded that the present model and its current parameters, capture the most important features of the material behaviour, i.e. shear softening for strains up to 20% and viscoelastic material behaviour.

Chapter 6

FE modelling of transient rotation of a simple physical head model

The objective of this chapter is to investigate errors related to material modelling and spatial discretisation in an explicit Finite Element code during traffic related impacts. A silicone gel filled cylindrical cup was subjected to a transient rotational acceleration. Two variants of the model exist, an open cup, allowing large strains at modest impact conditions, and a closed cup, mimicking the closed geometry of a real head. In both geometries gel response was measured using optical markers. The open cup experiments could be simulated very well using the material model developed in Chapter 5 in which hydrostatic and deviatoric parts of the strain were separated in the stress formulation. The error in angular marker displacements was less than 22%. The closed cup trajectories were overestimated by 62% but the time history looks realistic. Increasing the mesh density from 28 to 56 elements per cup diameter yields changes of displacements of 4% only. This supports the rule of thumb derived in Chapter 2, that 24 elements per maximum wave length are needed for accurate modelling. Without decoupling the hydrostatic and deviatoric parts of the stress, the stiffness at finite shear strain was overestimated severely, especially in the closed cup simulation. This illustrates the dangers of extrapolating small strain theory to finite deformations, especially with nearly incompressible material behaviour.

6.1 Introduction

Physical, i.e. mechanical, head models, that contain deformable representations of substructures of the head can be used for gaining insight in strain levels occurring in the dynamic response of the head during impact [71; 90; 93; 141]. However, physical models can also be used for investigating the accuracy of Finite Element Models used in impact simulations.

Finite Element models of the head, potentially suffer from two kinds of errors. The first kind of errors, mathematical modelling errors, arise by assumptions made in translating the reality to a mathematical description of that reality in terms of a set of differential equations. These errors are caused by assumptions about material behaviour, boundary conditions, geometry etc. The second kind of errors, numerical errors, are introduced by the numerical method used for solving the mathematical differential equations; in this case the Finite Element Method. Numerical errors are caused by the spatial and temporal discretisation needed to translate the mathematical model to a numerical model. Examples of numerical errors are numerical dispersion and spurious reflections investigated in Chapter 2 for small strains.

In this chapter, the capability of an explicit Finite Element code to predict transient brain response during a traffic related impact will be investigated. Emphasis will be given to numerical errors introduced by the spatial discretisation, and mathematical errors caused by material modelling assumptions, in particular the effect of separating the deviatoric and volumetric deformation in the stress formulation presented in Chapter 5.

During impacts at which brain injury occurs, strain levels of approximately 20% can be expected (refer to Chapters 3 and 4). At such deformation levels, validation of numerical models using analytical solutions is impossible. For this reason a physical model is developed with emphasis on straightforward translation to a mathematical model rather than for prediction of a real head impact response. This has been achieved by using a simple geometry, well characterised brain tissue model material and known boundary conditions. The model was subjected to a known, transient rotational acceleration and the mechanical response of the brain model material was measured. In this manner, errors that arise from translating the physical model to a mathematical model are eliminated as much as possible. The experiments have been simulated with a Finite Element model that includes that material model developed in previous chapter. The influence of mesh density on the response is investigated by varying the mesh density. The effect of decoupling the deviatoric and volumetric parts of the deformation in the stress formulation was investigated by repeating the simulations with a linear viscoelastic material model that does not use such decoupling.

6.2 Experimental model

6.2.1 Experimental setup

The dynamical response in a traffic related impact will be dominated by shear wave phenomena instead of pressure waves (see Chapter 2). For this reason, a rotational acceleration is applied to a cylindrical, silicone gel filled cup by means of a spring driven loading device. The rotation of the cup as well as the deformation of the gel within the cup is determined by marker tracking using a high speed video camera. The marker images thus obtained are post-processed in order to obtain marker tracks in real world coordinates. The setup, shown schematically in Figure 6.1, can be divided in three parts: the actual physical model, the spring driven loading device and the deformation recording section, consisting of camera and post processing unit. They will be discussed in this order.

Physical model The physical model consists of a silicone gel filled cylindrical polymethylmetacrylate (PMMA) cup. Two geometry variants were tested. In the first one, the cup is left open to create a stress free top surface of the gel. Simulation of the open cup experiments will provide insight into the model performance at large strains. In the second geometry variant, the top surface is closed by a transparent cover. This closed cup will provide insight in the model performance at isochoric deformations. For practical reasons, the cup dimensions are chosen smaller than real human head dimensions. The cup inner diameter was set to 70 mm and its depth equals 26 mm.

The cup is filled with Dow Corning Sylgard 527 A&B silicone gel that serves as brain tissue model material. This material resembles brain tissue reasonable well under both shearing and compression loading (see Chapters 3 and 4). The material shows linear viscoelastic material behaviour at large shear strains (refer to Chapter

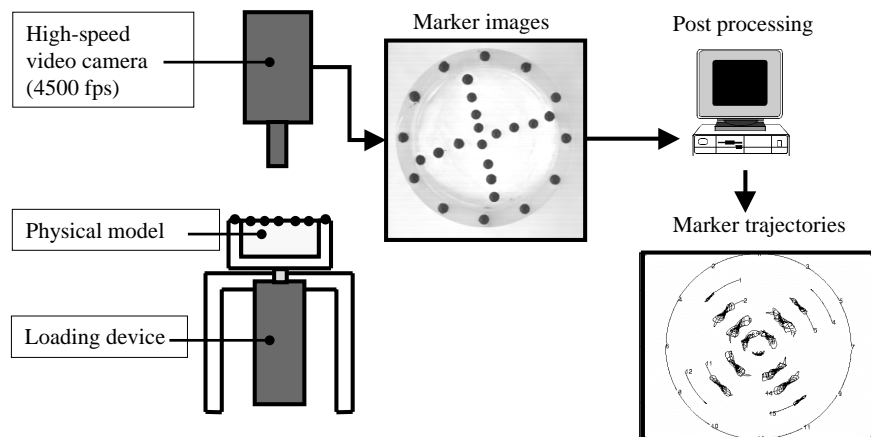


Figure 6.1: Schematic overview of the experimental setup.

4). Ultrasonic experiments on the silicone gel indicate that the P-wave propagation velocity in silicone gel equals $1048 \pm 43 \text{ m/s}$ [139] compared to 1550 m/s in brain tissue [45; 83]. From this it can be derived that the bulk modulus of the gel equals approximately 1 GPa , which is about half the bulk modulus of brain tissue. An additional advantage of this gel is that it sticks to the PMMA walls (and cover) of the (closed) cup, thus providing a well defined, no-slip, boundary condition. The A and B components of the gel were mixed in a one-to-one mass ratio and left hardening in the cup for at least two weeks before experiments commenced.

Loading device The cup is rotated along its axis of symmetry by a spring, connected to the cup via a ratchet wheel. The maximum rotation angle over which the cup is accelerated is set to 2.2 rad . When the cup reaches its end of motion range it hits the support frame and is stopped abruptly. The design of the spring driven loading device is such that strain and strain rate levels associated with injury can be reached. Strain levels ranging from 15% to 21% have been associated with the occurrence of axonal injury [10; 141] whereas 19% natural strain (i.e. 21% stretch) has been associated with the breakdown of the blood brain barrier [131]. The strain rate associated with injury is unknown but is estimated as follows. Animal data revealed that, at a change of angular velocity, $\Delta\omega = 150 \text{ rad/s}$, an angular acceleration, $\dot{\omega}$, of $1.5 \cdot 10^4 \text{ rad/s}^2$ could be associated with the occurrence of Diffuse Axonal Injury [141]. From these experiments, a typical time duration for the impact can be estimated using, $T_{\text{impact}} = \frac{\Delta\omega}{\dot{\omega}} = 10 \text{ ms}$. If it is assumed that indeed strain values of 15 to 21% occurred during these impacts and that a constant strain rate was present, a lower bound estimate of the typical strain rate becomes, $\dot{\gamma} = \frac{\gamma_{\text{max}}}{T_{\text{impact}}} = 15 \text{ to } 21 \text{ s}^{-1}$.

Deformation recording Histories of both gel deformation and cup rotation were determined using marker tracking. 4-mm diameter markers were perforated out of a slide of black plastic material and placed in the gel (gel markers) and on the cup edge (cup markers) (refer to Figure 6.2). The mass density of the markers is less than that of the gel. For the open cup the gel markers were placed on top of the silicone gel while for the closed cup, the gel markers were placed at half cup height in a plane parallel to the top plane. During the experiment all marker positions were recorded

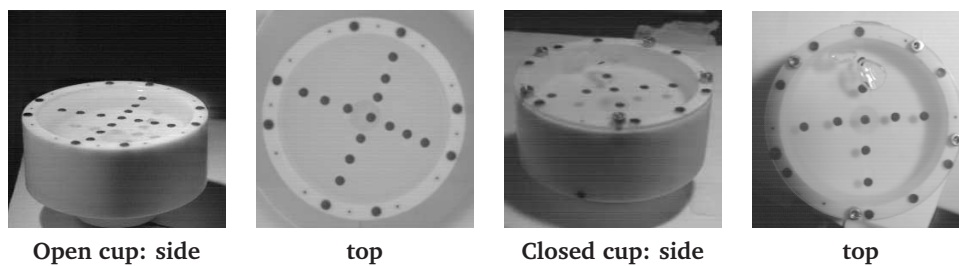


Figure 6.2: Side and top view of the cylindrical model. Left two pictures: open cup. Right two pictures: closed cup. Note that cup markers are placed on top of cup edge whereas gel markers are placed on top (open cup) or in the center plane (closed cup).

at 4500 frames per second by a high-speed video camera (Kodak Ektrapro ES Motion Analyser) at a resolution of 256X256, 8-bit gray-scale pixels. The optical axis of the camera was positioned as to approximately coincide with the axis of rotation of the cup (refer to Figure 6.1). Special lighting equipment utilizing infrared filters has been used to reduce object heating and reflections have been eliminated by the use of diffuse lighting.

The markers were tracked using the MATLAB Image Processing Toolbox [89]. Marker positions in pixels were computed from contour plots of the images using a circle fit method based on a least square approximation. The image coordinates were converted to real world coordinates using a linear transformation according to,

$$\underline{x}_{mm} = \underline{T} \cdot \underline{x}_{pix} \quad (6.1)$$

in which \underline{x}_{mm} denotes real world marker coordinates in mm , \underline{x}_{pix} the image coordinates in pixels and \underline{T} a 2×2 transformation matrix. To determine the transformation matrix, the positions of the cup markers were determined beforehand using an X-Y measuring device. The initial coordinates of the cup markers in pixels were determined from the first recorded frame. The components of the transformation matrix were determined using a least square approximation using MATLAB [89]. The Cartesian coordinates thus obtained were converted to polar coordinates. To do this, the rotation point was determined using the fact that the trajectories of the cup markers should be a (part of a) circle. First, the initial and end position of every cup marker was determined. Then, the bisectors perpendicular to the lines connecting initial and end position of each cup marker were determined. These perpendicular bisectors should cross in the rotational point.

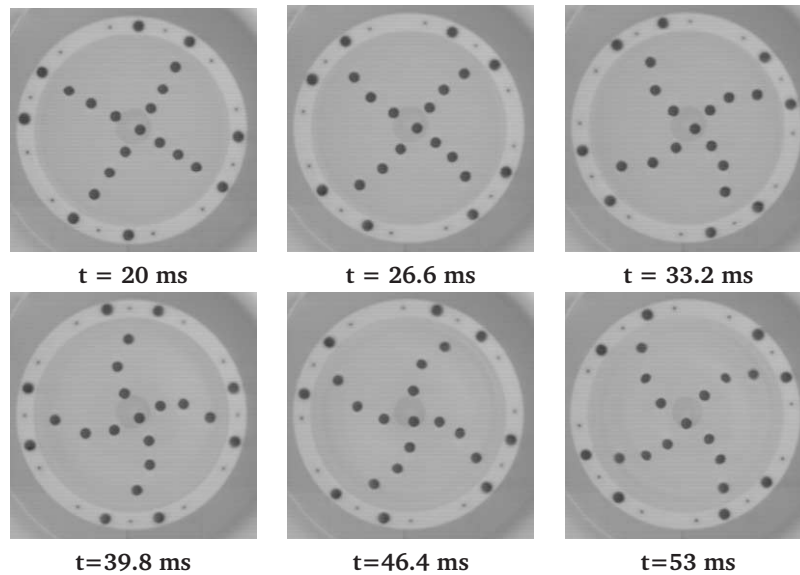


Figure 6.3: Sequence of frames starting at $t = 20$ ms (upper left) to 53 ms (lower right). Cup rotation is clock wise.

In this manner, the rotation point has been determined for each couple of cup markers with approximately perpendicular bisectors. The average value has been taken as the best estimate of the real rotation point.

6.2.2 Experimental results

Open cup Figure 6.3 shows a sequence of frames of the open cup during the acceleration part of the loading. In these pictures, the markers can clearly be distinguished. From the positions of the cup markers, rotation and angular velocity for the cup have been determined as a function of time. They are shown in the upper left plots in Figure 6.4. The angular velocity of the cup increases during the first 53 ms to a value of 90 rad/s approximately. At 53 ms, the cup is stopped at its end of motion range at 2.2 rad. The deformation of the gel will be studied until that moment in time only since this part of the loading was designed to reproduce a typical impact load. The upper right plot of Figure 6.4 shows marker trajectories of three selected markers in the gel as well as the trajectories of the markers on the cup. It can be seen that the rotation of the cup is axisymmetric, as expected. In the lower left plot the rotation of the gel markers, relative to a cup-fixed co-rotating coordinate system, is shown. It can be seen that the markers lag behind in motion with respect to the cup. Also it can be seen that the relative marker rotation increases for increasing radial

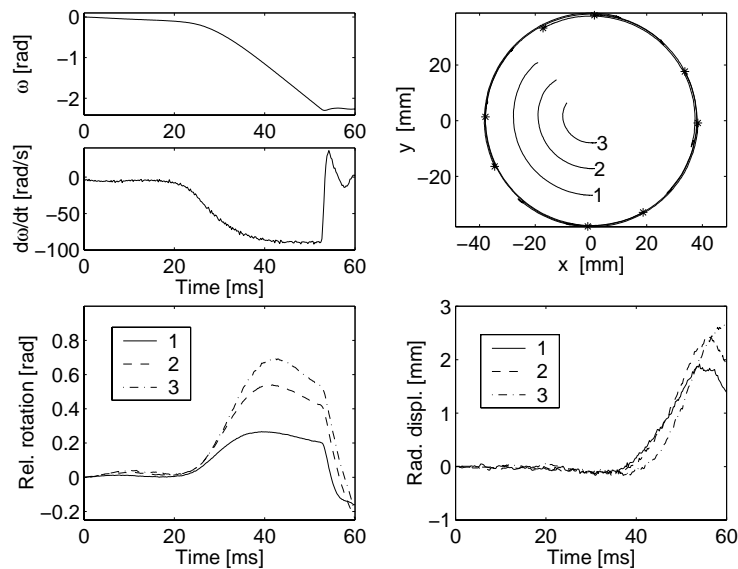


Figure 6.4: Results of open cup experiment. Top left: cup rotation and angular velocity. Top right: Marker trajectories: initial positions of gel markers numbered 1 to 3, initial positions of cup markers labeled *. Bottom left: Circumferential displacements of gel markers relative to cup circumferential displacement. Bottom right: Radial displacements of gel markers.

distance from the edge of the cup. This is expected since there is decreasing influence of edge boundary conditions towards the centre. Peak relative rotation occurs first at about 40 ms at marker 1 close to the cylinder edge and occurs a few ms later in marker displacements 2 and 3. The lower right plot of Figure 6.4 shows that maximal radial gel marker displacements are on the order of 2 mm . The accuracy of the radial measurements is determined by observing the radial displacements of the cup markers. For the open cup it was observed that the radial position of the cup markers is constant within 0.3 mm . For this reason it can be concluded that the radial deformation gel marker displacements are significant. They are related to the three-dimensional deformation present during this experiment as shown in Figure 6.5.

Closed cup Figure 6.6 shows the experimental results of the closed cup. It can be seen that the applied load is similar to the one applied on the open cup. The maximum relative rotations equal 0.12 and 0.24 rad for markers 1 and 2. The radial displacements of the markers are on the order of 0.1 mm while the radial displacements of the cup markers are on the order of 0.5 mm . For this reason no conclusions can be drawn on the exact radial displacements of the gel markers.

6.2.3 Discussion on experiment

Accuracy of the experiment The accuracy of the experiment is determined by two factors. The first factor is the accuracy of the measurement system used. This is determined by the resolution used in combination with marker size. Since the cup image fills the complete field of view, 256 pixels cover approximately 80 mm . Thus, the typical pixel size equals $256/80 = 0.3$ mm . As a result, a marker diameter will be covered by 12 pixels. The accuracy by which marker positions are obtained is roughly estimated as pixel size over number of pixels per marker and equals 0.03 mm . This corresponds with the noise level seen in the lower right plot of Figure 6.6.

A second factor determining the accuracy are errors induced by performing the experiment itself. In this case, the loading spring is released manually. As a result, a small translational motion of the cup with respect to the camera can be present. Furthermore the optical axis of the camera is not positioned exactly perpendicular to the marker plane. The magnitude of these inaccuracies has been estimated by observing the change in radial position of the cup markers which was on the order of 0.3 and 0.5 mm for the open and closed cup experiment respectively.



Figure 6.5: Side view of open cup experiment showing the three-dimensional deformation field present. Time history from left to right.

Impact loading conditions The gel response during the experiment, in terms of strain and strain rate, should be representative for impact conditions. For estimating the strain levels in the experiment, it is assumed that the marker motion is two-dimensional in the image plane recorded by the high-speed camera. A lower bound for the shear strain, $\gamma(t)$, occurring in this plane can be found using,

$$\gamma(t) = \frac{(R_0 + \Delta R) \sin \Delta \phi(t)}{R_{cup} - (R_0 + \Delta R) \cos \Delta \phi(t)} \quad (6.2)$$

in which R_0 , R_{cup} , and ΔR represent the initial radial position of the marker, the cup radius and the change of marker radial position respectively while $\Delta \phi(t)$ is the angular marker displacement relative to the cup (refer to Figure 6.7). This strain represents a shear strain that would occur at the edge of the cup. When simple shear is assumed the maximum principal strain, $\lambda(t)$, can be determined as,

$$\lambda(t) = \left[1 + \frac{\gamma(t)^2}{2} + \gamma(t) \sqrt{1 + \frac{\gamma(t)^2}{4}} \right]^{\frac{1}{2}} - 1 \quad (6.3)$$

The principal strain histories thus obtained are shown in Figure 6.7. For the open cup the maximum principal strain values range from 10% to 49% while for the closed cup experiments strain values of 9% and 15% were found. The maximum strain rate values were determined using numerical differentiation and equal 45 s^{-1} for the

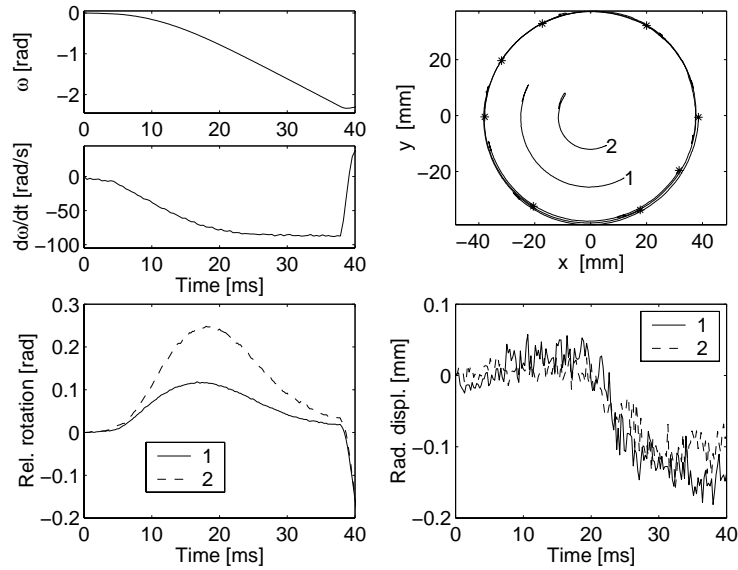


Figure 6.6: Experimental results of closed cup experiment. Top left: cup rotation and angular velocity. Top right: Marker trajectories: initial positions of gel markers numbered 1 and 2, initial positions of cup markers labeled *. Bottom left: Relative circumferential displacements of gel markers. Bottom right: Radial displacements of gel markers.

open cup and 20 s^{-1} for the closed cup. Although these values are rough estimates, it is concluded that both maximum strain values as well as strain rate values in the physical model are within the impact range estimated in section 6.2.1 (i.e. strain values of 15% to 21% and strain rate values of 15 s^{-1} to 21 s^{-1}).

6.3 Numerical model

The experiments, described in previous section, have been simulated in MADYMO. The material model presented in Chapter 5 was used to describe the material behaviour of the silicone gel.

6.3.1 Methods

Mathematical model In the mathematical model it is assumed that no slip occurs between the gel and the cup and that the cup and its cover behave rigidly. For this reason the cylindrical geometry of the gel is modelled only. For the closed cup, radial and axial motion of all outer surfaces are suppressed while circumferential motion is prescribed according to the experimentally obtained rotation history in Figure 6.6. For the open cup, the same boundary conditions hold except for the upper surface, which is considered stress free while the other outer surfaces are subjected to the rotation history in Figure 6.4.

The silicone gel used behaves like a linear viscoelastic solid for strains up to 50% and frequencies up to 461 Hz (refer to Chapters 3 and 4). For this reason, a linear four-mode Maxwell model has been fitted to the experimental data using the method already presented in Chapter 5. The fitted relaxation times, λ_i , and shear moduli, G_i , are shown in Table 6.1. Figure 6.8 shows that the model fits the experimental data well. The bulk modulus applied has been determined from ultrasonic data, as $K = c_p^2 \rho$ where $c_p = 1048 \text{ m/s}$ [139] and mass density $\rho = 970 \text{ kg/m}^3$ (refer to the theory in Section 2.2, Chapter 2).

These material parameters have been applied in the material model presented in Chapter 5 in which the non-linear material behaviour was disabled ($f_{nls} = 0$) and

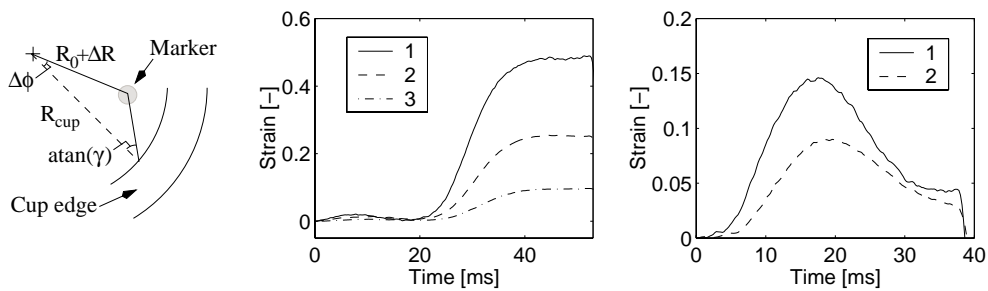


Figure 6.7: Left: Graphical representation of strain computation. Middle and Right: Estimated maximum principal strain histories. Middle: Open cup, Right: Closed cup.

again it was assumed that $c_{10,i} = c_{01,i} = \frac{1}{2}G_i$. The model will be referred to as REF material model in this Chapter.

To investigate the influence of the degree of coupling between hydrostatic and deviatoric stress, the simulations of open and closed cup were also performed using the linear viscoelastic material model already present in MADYMO (LINVIS) [148]. In this model, which will be referred to as the CPL material model from now on, correct large deformation behaviour has been achieved by linearly coupling the Green-Lagrange strain, $\mathbf{E} = \frac{1}{2}(\mathbf{F}^c \cdot \mathbf{F} - \mathbf{I})$, to the Second Piola-Kirchoff stress tensor, \mathbf{S} , according to,

$$\mathbf{S} = K \text{trace}(\mathbf{E}) \mathbf{I} + 2 \int_{-\infty}^t G(t - \tau) \dot{\mathbf{E}}^d d\tau \quad (6.4)$$

in which, for small deformations, K resembles the bulk modulus and $G(t)$ a time dependent relaxation modulus. The Cauchy stress then is obtained using,

$$\boldsymbol{\sigma} = \frac{1}{\det(\mathbf{F})} \mathbf{F} \cdot \mathbf{S} \cdot \mathbf{F}^c \quad (6.5)$$

Numerical implementation Spatial discretisation of the mathematical model has been achieved using brick elements with linear interpolation functions and reduced

Table 6.1: Four-mode Maxwell parameters for Sylgard 527 A&B silicone gel fitted to oscillatory data presented in Chapter 4.

| Mode i | Maxwell parameters | | Bulk modulus K [GPa] |
|-----------|--------------------|-----------------------|-------------------------|
| | G_i [Pa] | λ_i [ms] | |
| 0 | 216.41 | ∞ | 1.065 |
| 1 | 122.32 | 309.8 | - |
| 2 | 378.79 | 24.71 | - |
| 3 | 1717.2 | 2.156 | - |
| 4 | 27599 | $9.743 \cdot 10^{-2}$ | - |

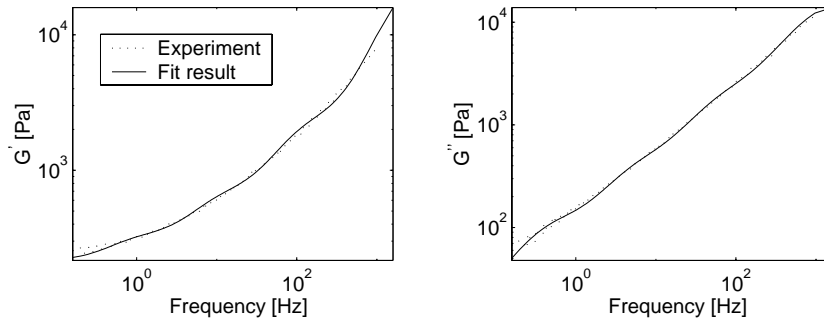


Figure 6.8: Storage and loss modulus G' and G'' of Sylgard 527 A%B silicone gel together with 4 mode Maxwell fit. Fitted material parameters are shown in Table 6.1.

integration. The element size is based on the error analysis in Chapter 2. Approximately 24 elements per maximum wave length in the model have to be used to reduce errors due to numerical dispersion to less than 1%. If we assume that the maximum wavelength present equals the diameter of the cup, the lower bound for the mesh density equals at least 24 elements over the diameter. In this case 28 elements over the diameter have been used. To keep the initial element shape close to cubic, twelve element layers have been used over the cup height. To investigate the effect of spatial discretisation on the numerical results, the simulation of the open cup experiments has been repeated with both a more coarse and a more refined mesh. The coarse mesh has been created by merging eight elements of the reference mesh into a single, larger element. Mesh refinement has been achieved by splitting every element in the reference mesh into eight new elements. To reduce computational time using this finest mesh, a quarter cylinder was modelled only while symmetry conditions were applied on the cutting planes. The meshes are shown in Figure 6.9.

Post processing Nodes have been selected with radial distances as close as possible to the distances determined experimentally. Trajectories in the x-y plane were determined and are presented in polar coordinates for comparison with the experimental results.

6.3.2 Numerical results: REF material model

Reference mesh open model Figure 6.10 shows the time histories of nodal displacements in polar coordinates corresponding to the marker displacements of markers 1, 2 and 3 in the open cup (see Figure 6.4). The experimental results are plotted in the figure for comparison. It can be seen that the model predicts

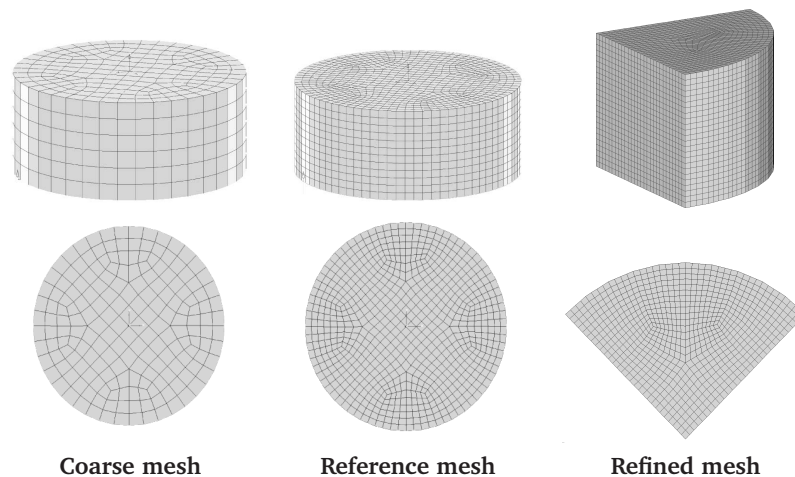


Figure 6.9: Meshes used for modelling open and closed cup. Refined mesh consists of quarter mesh only with symmetry boundary conditions applied on cutting planes.

the marker trajectories quite well. The general shape of the curves is the same for both experiment and simulation. The numerical model however, overestimates the relative rotation of the markers by 17%, 14% and 24% for markers 1, 2 and 3, respectively. The time history of the radial displacement shows that the numerical results are within range of the experimental ones. The radial displacements remain approximately zero until 30 *ms*. After this, they increase to 2 *mm* approximately.

Reference mesh closed model The experimental closed cup results are compared with the numerical reference mesh results in Figure 6.11. The numerical model overpredicts the amplitude of the angular rotation by 62% and 46% for marker 1 and 2, respectively. The predicted radial displacements are on the order of 0.1 *mm* and are in the same order of magnitude as the experimental results. However, the reliability of the radial displacements from the experiment was low (refer to page 89).

Mesh density variation The simulations of the open cup have been repeated with two different mesh densities. The results in Figure 6.12 show that the trends in all results remain the same. The average maximum value of the angular displacements

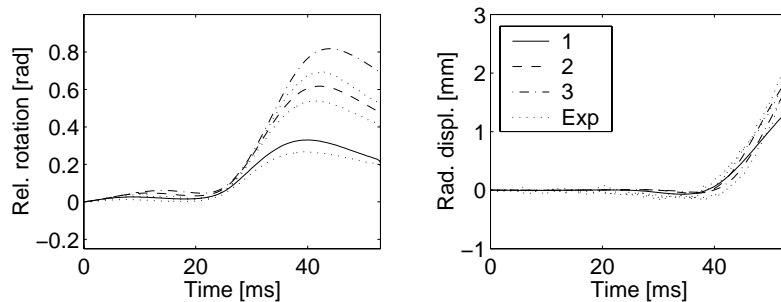


Figure 6.10: Marker trajectories obtained with reference mesh and REF material model versus experimental results open cup (dotted line). Left: Angular displacements relative to cup. Right: Radial displacements.

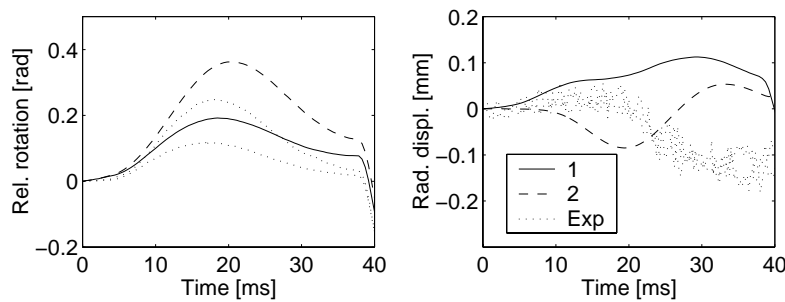


Figure 6.11: Marker trajectories obtained with reference mesh and REF material model versus experimental results closed cup (dotted line). Left: Angular displacements relative to cup. Right: Radial displacements.

increases by 10.8% when refining the mesh from coarse to reference mesh. Further refinement provides an increase of peak values by 4.0%. The moment of time on which these maxima are reached also increases with mesh density (4.1% (1.7 ms) and 1.0% (0.44 ms) respectively). The radial displacements show a decreasing trend when the mesh density is increased.

6.3.3 Numerical results: CPL material model

Figure 6.13 shows time histories of nodal displacements in polar coordinates as obtained with the CPL material model. The results of the open cup simulation in the upper plots show that relative marker rotations are under-estimated by 28%, 32% and 32% for markers 1,2 and 3, respectively. Also the time history of the marker rotations deviates from the experimental results in that the oscillations appear with shorter time duration. As a result, the peak values appear earlier in time than the experimental values. The radial displacements in the upper right plot are overestimated 4 mm and appear also ahead of the experimental values. The lower plots show the results of the closed cup simulation with the CPL material model. The marker displacements are very small in both angular as well as radial direction. Only a very small oscillation can be seen that does not resemble the experimental time history at all. This means that the gel displays a nearly rigid-body motion when the closed cup is simulated. This phenomenon is independent of mesh density used.

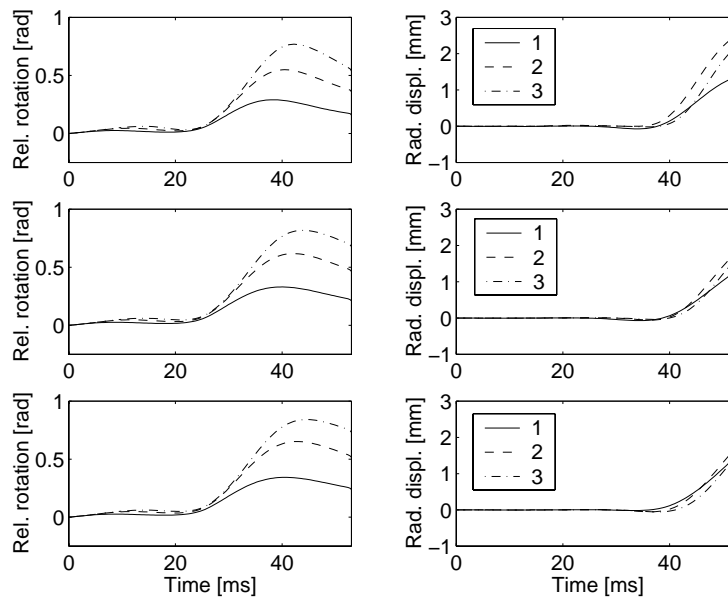


Figure 6.12: Effect of mesh density on the response of the open cup simulation with REF material model. Left: Angular displacements relative to cup. Right: Radial displacements. Top row: Coarse mesh. Middle row: Reference mesh. Lower row: Finest mesh.

6.4 Discussion

The open cup experiments could be simulated quite well with the REF material model. The time history of the marker angular displacements could be reproduced with 22% accuracy. This difference may be caused by errors in the choice of the material parameter values. The values used were determined on a different gel specimen than the one used in this experiment. The experimental data of three different samples in Chapter 4 differed by approximately 0.2 to 20% depending on the frequency used. The effect of this spread has been investigated by performing an additional simulation with material parameters increased by 10%. The results obtained with the reference mesh are shown in Figure 6.14. It can be observed that the model with increased parameters provides good predictions of the experimentally determined marker displacements. Maximum numerical errors in angular rotation equal 8.9%, 0.23% and 2.5% for marker 1,2 and 3 respectively.

The closed cup simulation results with REF material model also show overestimated experimental angular displacements but correct trends in time history. A possible explanation for this overestimation is again the uncertainty in the material parameters. However, the fact that the overestimation in this isochoric deformation state is more pronounced than in the open cup simulations suggests a second hypothesis.

In the REF material model, the hydrostatic behaviour is decoupled from the deviatoric

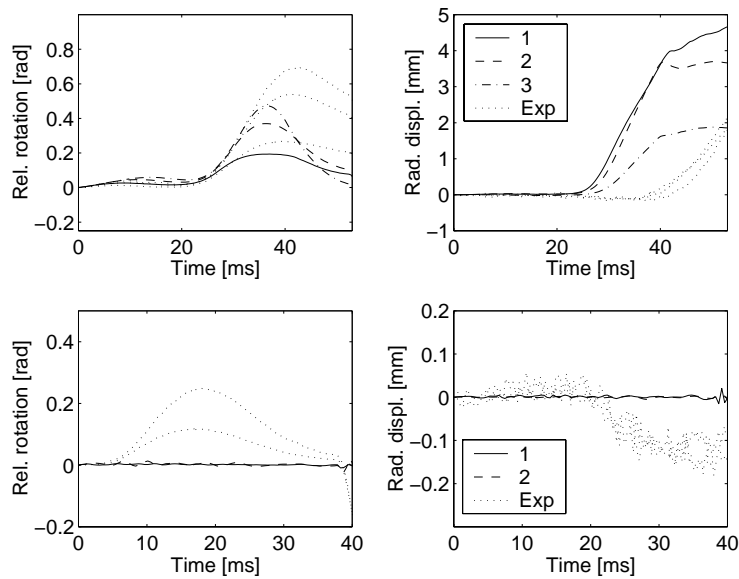


Figure 6.13: Marker trajectories obtained with reference mesh and CPL material model versus experimental results (dotted line). Top: Open cup results. Bottom: Closed cup results. Left: Angular displacements relative to cup. Right: Radial displacements.

part of the Cauchy stress (refer to equations (5.21) and (5.22) in Chapter 5). Furthermore the deviatoric stress depends on the deviatoric part of the isochoric deformation only. As a result, the shear behaviour of the model is independent of the hydrostatic deformation. If, in reality, some coupling between shear and hydrostatic deformation is present, implementation of this coupling in the material model will lead to reduced displacements in the simulation results. This will be more pronounced in the closed cup simulation than in the open cup simulation. However, the presence of this partial coupling could not be validated in the present material experiments and remains to be investigated. This can be done by determining the normal force history during a simple shear experiment or by applying a different deformation, for example an unconfined compression.

Mesh density Increasing the mesh density using the REF material model, revealed differences in amplitude of the marker displacements on the order of 4%. The time history behaviour, i.e. the 'shape' of the time history, did not change. This indicates that the results of the reference mesh can be used to indicate where and when peak strain or stress values occur. Although it is unclear whether the results of the finest mesh used were not mesh-size independent yet, no further mesh refinement has been performed since this would yield excessive computational times.

Effect of decoupled hydrostatic and deviatoric stress The importance of decoupling the hydrostatic strain from the deviatoric stress was clearly illustrated by the results with the CPL material model. The open cup simulation showed underestimation of the strain response, whereas in the closed cup simulation virtually no strains were present at all. The reason for this behaviour will be illustrated using an example.

In absence of time dependent behaviour ($G(t) = G$), the constitutive equation (6.4) reduces to,

$$S = (K - \frac{2}{3}G)\text{trace}(E)I + 2GE \quad (6.6)$$

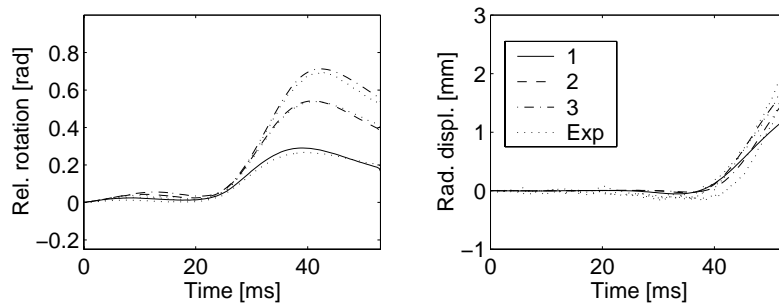


Figure 6.14: Marker trajectories obtained with reference mesh, REF material model and 10% increased material parameters, versus experimental results (dotted line). Left: Angular displacements relative to cup. Right: Radial displacements.

which in fact represents Hooke's law for linear elastic materials in which the infinitesimal strain measure ε is replaced by the Green-Lagrange strain E . Let us assume that the deformation patterns in the closed cup resemble that of isochoric simple shear. The resulting shear stress component of the Cauchy stress, τ , then depends on both shear modulus, G , and bulk modulus, K ,

$$\tau = G \left(\gamma + \frac{2}{3} \gamma^3 \right) + \frac{1}{2} K \gamma^3 \quad (6.7)$$

Due to the nearly incompressible material behaviour ($G = 1000 \text{ Pa}$ and $K = 10^9 \text{ Pa}$ approximately, refer to Table 6.1), the last term in equation (6.7), related to the bulk modulus, will dominate the shear behaviour already for very small strains: for $\gamma = 1\%$ this term will be a factor of 50 larger than the first term, related to the shear modulus. This behaviour does not correspond with the behaviour observed experimentally.

6.5 Conclusions

A simple physical model was used to create a response in silicone gel model material resembling that of brain tissue in a traffic related impact. Two variants were used, an open cup and a closed cup. In both geometries gel responses resembling brain tissue impact response could be obtained. Maximum principal strain values of 49% and 15% occurred during open and closed cup experiments, respectively. These are in the order of the 20% strain threshold above which tissue damage was induced in animal experiments. The strain rates obtained in the experiments (45 s^{-1} and 20 s^{-1} for open and closed experiment, respectively) are also of correct magnitude compared to the 20 s^{-1} value estimated to be present in a real head during impact.

The open cup experiments could be simulated very well using the material model developed in Chapter 5. Maximum errors in angular marker displacements were less than 22% and reduced to 8.9% when the material properties were increased within the experimental range shown in Chapter 4 (10% increase). The closed cup trajectories were overestimated by 62% but time history looked realistic. A possible explanation might be the assumed decoupling between shear and hydrostatic deformation in the constitutive formulation (refer to section 6.4). Increasing the mesh density from 28 to 56 elements per cup diameter yielded changes of displacements of 4% only but did not alter the nature of the time history. This supports the rule of thumb derived in Chapter 2, that 24 elements per maximum wave length are needed for accurate modelling.

The closed cup simulations showed that without decoupling the hydrostatic and deviatoric parts of the stress, the stiffness at finite shear strain was severely overestimated. This effect was largest for the closed cup simulation. This illustrates the importance of correct constitutive modelling when dealing with nearly incompressible behaviour, especially when applying such material model in a head model which also consists of a more or less closed geometry. The presence of this effect in a real head model will therefore be studied in the next chapter.

Chapter 7

Effects of constitutive modelling on brain response in a 3-D FE head model

It is investigated how the choice of brain constitutive model affects the dynamic response of brain tissue in a three-dimensional head model. Three brain models are used: the model presented in Chapter 5 with and without shear softening included, and the standard linear multi-mode viscoelastic material model present in MADYMO 5.4.1. In the latter model, the deviatoric and hydrostatic response is not decoupled, in contrast to the first two model variants. The head model is subjected to a transient eccentric rotation in the sagittal plane and the brain response is investigated in quantities, commonly associated with injury. It was found that large strains occur at modest impact conditions. This is most likely caused by the values for the shear moduli applied in the model. These are at least a factor of ten lower than the ones used in head models in literature but comparable to material data in recent literature and own experiments. Shear softening influences the strain and stress levels but not the spatial distribution. The pressure response was of quasi-static nature and did not depend on non-linear material behaviour. Decoupling of deviatoric and hydrostatic deformation in the constitutive model was found to be necessary for correct prediction of brain response in head modelling.

7.1 Introduction

In previous chapters a non-linear viscoelastic material model capable of describing the material behaviour of brain tissue under simple shear conditions was presented. The model is capable of describing the shear softening observed for strains up to 20%. Physical model simulations in the previous chapter pointed out that the model is capable of accurately predicting the dynamical response of a nearly incompressible linear viscoelastic material under impact conditions. It was found that decoupling of the deviatoric and volumetric deformation in the stress tensor was crucial for the good performance under isochoric deformations.

In the present chapter, the constitutive model is applied in a three-dimensional head model, subjected to rotational acceleration history in posterior-anterior direction. To investigate the effect of shear softening as well as decoupling of volumetric and deviatoric deformation, brain tissue's constitutive description is changed accordingly. The effect of the various modelling approaches will be analysed by comparing predicted local brain responses, expressed in quantities associated with injury in literature.

7.2 Numerical model

The head model used was originally developed in the implicit Finite Element Code MARC [88] by Claessens [36] and has been evaluated using intracranial pressure responses obtained from a cadaver experiment by Nahum [37; 104]. This model was transferred to the explicit Finite Element Code LS-DYNA3D [86] for use in an accident reconstruction study [154]. In that study improvements with respect to element size and shape were carried out. Furthermore, the anatomical detail of the model was increased by including a more realistic geometry near the skull base and falx cerebri and by including an element layer between cerebri and skull to model the dura mater. In the present study, the model is transformed to MADYMO 5.4.1 format [146]. All material descriptions were retained except for the constitutive model and model parameters of the brain tissue. In the next sections the model will be presented briefly. More detailed information about the model can be found in the work of Claessens [36; 37] and Verhoeve [154].

Geometry The geometry of the model is based on the Visible Human data set [153] which consists of MRI (Magnetic Resonance Imaging) and CT (Computed Tomography) transversal images of a male person. Head length (195 *mm*), width (155 *mm*) and height (225 *mm*) have been scaled to 50th percentile measures according to Pheasant [119]. The anatomical structures, included in the model, are shown in Figure 7.1. They are grouped in three components; the cranium, the meningeal layers and CSF, and the brain tissue. Table 7.1 provides information on each component and constitutive models used. All substructures in the head model are assumed to be rigidly connected to each other. The brain is tied to the skull via a layer of compliant elements and the motion of brain tissue through the foramen

magnum is suppressed. The head is meshed in one continuous mesh consisting of 8-node brick elements. Spatial integration is achieved using one integration point per element only (reduced integration). Hourglass control is used to suppress the zero energy deformation modes that exist for reduced integrated brick elements [148].

Constitutive assumptions In this study we will not model a direct contact impact. For this reason the cranium is assumed to be rigid. The meningeal layers were modelled as in the original model by Claessens [36; 37], i.e. linear elastic material model with material parameters taken from Ruan *et al.* [126] (refer to Table 7.2). The brain tissue is modelled using a four mode viscoelastic material model. Three modelling variants have been investigated:

1. REF: In the reference simulation, the brain tissue is modelled using the newly developed material model with linear material parameters, i.e. shear softening is not included.
2. SOF: Like REF but with shear softening added.

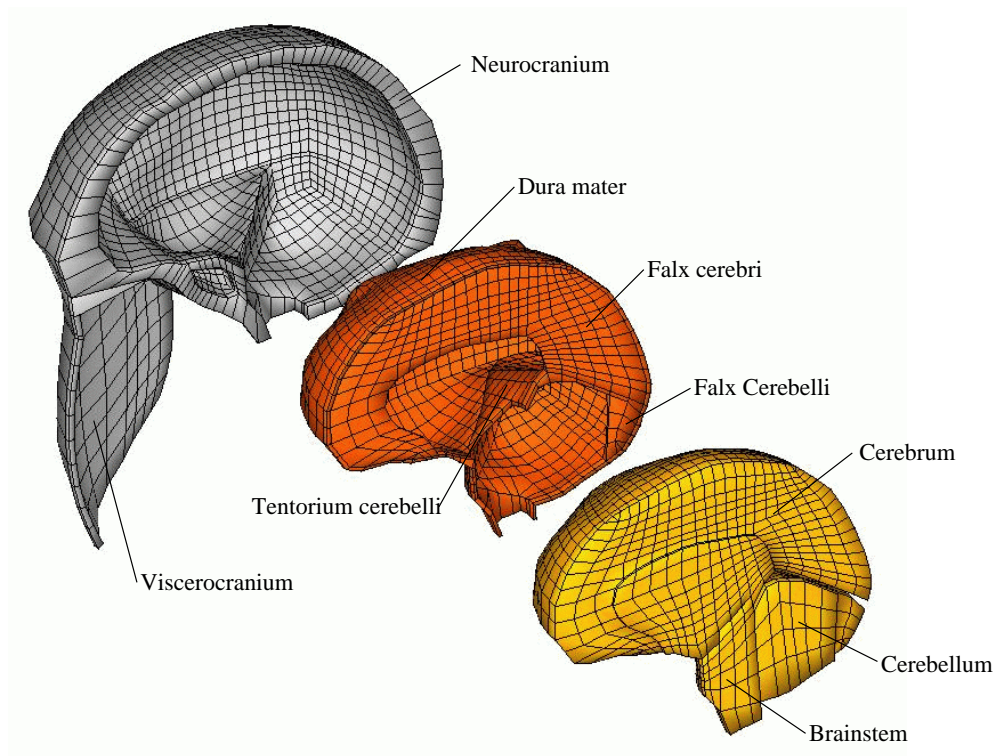


Figure 7.1: Overview of the head model [154]. The right half of the head model is shown with the brain, the meningeal layers (dura mater with falx and tentorium) and the skull separated. In the model, these structures are connected to each other, resulting in a continuous Finite Element mesh.

3. CPL: The linear viscoelastic material model as present in MADYMO version 5.4.1 has been used (LINVIS). This model linearly couples the second Piola-Kirchoff stress tensor to the Green-Lagrange strain and includes viscous behaviour using an integral form. As a result deviatoric and hydrostatic part of the deformation are not decoupled. (Refer to the Discussion section of Chapter 6 for more details).

Comparing the REF and SOF results provides insight into the effect of shear softening on the dynamic response of brain tissue. Comparing the REF and CPL results shows the importance of decoupling the deviatoric and hydrostatic parts of the deformation in the stress formulation in a realistic head geometry.

The decoupled non-linear viscoelastic material model used in the SOF simulation, is a slightly adapted version of the model presented in Chapter 5. The latter model, was capable of predicting the shear softening observed within the experimental strain range (up to 20% shear strain). However, for strain levels outside the experimental strain range, negative shear stiffness can occur. To prevent numerical problems associated with negative stiffness, an extra deviatoric stress was added to the deviatoric stress part of the original model. The stress formulation was chosen such that its effect on the response is minimal within the experimental strain range while negative stiffness is prevented for shear strains beyond that range. However, this extra stress will cause shear stiffening to occur for strains beyond the experimental range. For this reason extra care has to be taken in interpreting results at strains outside the experimental range. The complete theory on the model adaptation is presented in Appendix B.

Table 7.1: Configuration of the head model used; presentation of the structures included, the number and type of elements used, and constitutive models used.

| Anatomical structure | No. of elements | Constitutive model |
|-----------------------------------|-----------------|--------------------|
| Cranium (skull) | 3212 | Rigid |
| viscerocranium (facial bones) | 188 | |
| neurocranium | 3024 | |
| Meningeal layers & CSF | 3188 | Linear elastic |
| Dura mater | 2536 | |
| - falx cerebri | 448 | |
| - falx cerebelli | 18 | |
| - tentorium cerebelli | 186 | |
| Brain tissue | 7692 | Viscoelastic* |
| cerebrum/corpus callosum | 6758 | |
| cerebellum | 732 | |
| brainstem | 202 | |

* Three variants are used:

REF: decoupled-linear viscoelastic: no shear softening

SOF: decoupled non-linear viscoelastic: shear softening.

CPL: linear viscoelastic, coupled deviatoric / hydrostatic behaviour

Brain tissue material parameters are taken from Chapter 5. Except for the non-linear parameter, f_{nls} which has been fitted again to eliminate the small effect within the experimental range caused by the model adaptation (refer to Appendix B). They are shown in Table 7.2.

Loading conditions An eccentric rotation in posterior-anterior direction has been applied to the model using a time history obtained from [11]. The axis of rotation is positioned at 155 mm below the anatomical origin of the model which is located in the ear hole projected to the sagittal plane. The eccentricity resembles a typical neck length [49; 144]. The rotational acceleration time history consists of two sine functions shown in Figure 7.2, where the initial acceleration portion equals twice the amplitude and half the duration of the subsequent deceleration portion. The total rotational pulse duration was set to 30 ms whereas the maximum angular velocity was set to 5 s⁻¹ as to obtain strain values inside the brain tissue within the range of the material characterization experiments in Chapter 4, i.e. 20% shear strain

Table 7.2: Material properties used for the anatomical components in the three-dimensional head model.

| Structure | Shear modulus $G_i, i = 0 - n$ [Pa] | Time constants $\lambda_i, i = 0 - n$ [ms] | Bulk modulus K [GPa] | Non linear par. f_{nls} [-] | Mass density [$\frac{kg}{m^3}$] |
|-----------------|---|--|---------------------------|----------------------------------|--------------------------------------|
| Cranium (skull) | ∞ | - | ∞ | - | 2070 |
| Meninges & CSF | $1.086 \cdot 10^6$ | - | 0.105 | - | 1130 |
| Brain tissue | | | | | |
| REF, CPL | 255, 269, 323 427, 3299 | $\infty, 70.1, 7.63$ 1.41, 0.12 | 2.5 | 0 | 1040 |
| SOF | 255, 269, 323 427, 3299 | $\infty, 70.1, 7.63$ 1.41, 0.12 | 2.5 | -5.5553 | 1040 |

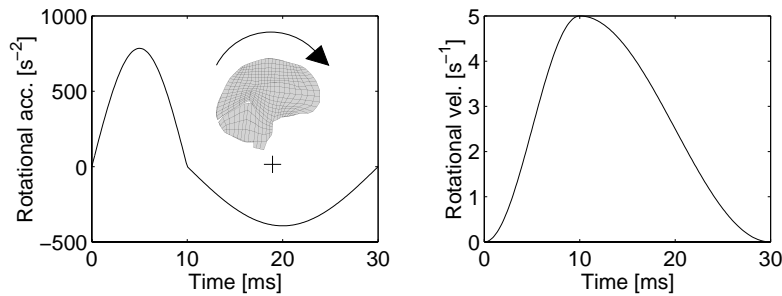


Figure 7.2: Angular rotation history used according to [11]. Left: Angular acceleration and schematic indicating direction of acceleration. Right: Angular velocity. Time duration set to 30 ms and maximum angular velocity to 5 s⁻¹.

corresponding to a Von Mises strain of approximately 0.22. This results in a maximum head rotation angle of 0.075 rad.

Time discretisation The MADYMO Finite Element module uses the conditionally stable Central Difference Method for time integration, as is common in explicit Finite Element codes. The maximum time step for obtaining a stable solution is determined by the Courant criterion which depends on mesh size and wave propagation velocity. In Chapter 2 is shown that application of the maximum time step provides the most accurate solution. In the present simulations this maximum time step is multiplied by 0.85 and kept constant during the complete simulation. This yields a time step of $4 \cdot 10^{-4}$ ms, which results in 75000 time increments to simulate the full 30 ms impact.

Post processing The effect of the various brain tissue modelling approaches on the dynamical brain response will be investigated in terms of parameters associated with injury. In Chapter 1 (Table 1.1) it has been shown that shear strain, maximum principal strain, Von Mises stress and pressure have been identified by various authors as potential causes for brain injury. These parameters can be described by the following three quantities,

- Von Mises, or effective, strain, $E_{VM} = \sqrt{\frac{3}{2}\text{trace}(\mathbf{E}^d \cdot \mathbf{E}^d)}$: This rotation invariant strain measure depends on the deviatoric Green-Lagrange strain, \mathbf{E}^d , only and is a measure of distortional deformation. As such, it provides information on shear deformation present in the brain tissue. Furthermore, this measure closely resembles the maximum principal strain due to the nearly incompressible nature of the brain tissue.
- Von Mises stress, $\sigma_{VM} = \sqrt{\frac{3}{2}\text{trace}(\boldsymbol{\sigma}^d \cdot \boldsymbol{\sigma}^d)}$: As viscoelastic material behaviour is assumed, the stress measure depends both on strain and strain rate quantities. Differences between Von Mises stress and Von Mises strain distributions therefore reflect the contribution of strain rate effects.
- Pressure, $p = -\frac{1}{3}\text{trace}(\boldsymbol{\sigma})$: Apart from being a potential injury cause, this quantity has been used in many studies [37; 72; 128; 129; 168], for evaluating head models against cadaver experiments by Nahum [104].

For each element in the brain mesh, maximum values appearing during the impact time history are determined and shown in contour plots of various para-sagittal cross-sections. Areas of interest will be determined and the time history of the quantities in these areas will be plotted.

7.3 Results

All simulations are performed on a Silicone Graphics Origin computer, with a 180 MHz, IP 27, R10.000 processor. The computational time equals approximately 10 hours and 30 minutes for all model variants.

7.3.1 Reference model: REF

Figure 7.3 shows contour plots of the maximum Von Mises strain and stress values during the impact in various para-sagittal cross-sections in the brain. The Von Mises strain ranges up to about 0.3 while the Von Mises stress ranges up to approximately 400 Pa. Both stresses and strains show similar, concentric, contour patterns with minimum values concentrated in the center of the cerebri. Maximum values appear at the upper part of the cerebral cortex (cross-sections 2 and 3 in Figure 7.3), in the mid-brain section (cross-section 1) and superior to the tentorium cerebelli (cross-sections 3 and 4). Another concentration of maximum values is found in the concave region near the temporal lobes. These will not be taken into account in the next discussion since it is believed that this maximum is severely influenced by bad element quality in that region.

The Von Mises stress and Von Mises strain histories in two elements, located in the superior cerebral cortex region (C) and in the mid-brain (M) are plotted in Figure 7.4. Both Von Mises strain and Von Mises stress time histories show the same tendencies. The mid-brain time histories of both stresses and strains lag behind the time histories in the cortical region. In turn, the cortical time histories lag behind the input rotational acceleration pulse in Figure 7.2. In both regions the strain time history lags behind the stress time history. Finally, superior cortex stress and strain values approach to zero at about 20 to 25 ms, while midbrain stress and strain levels

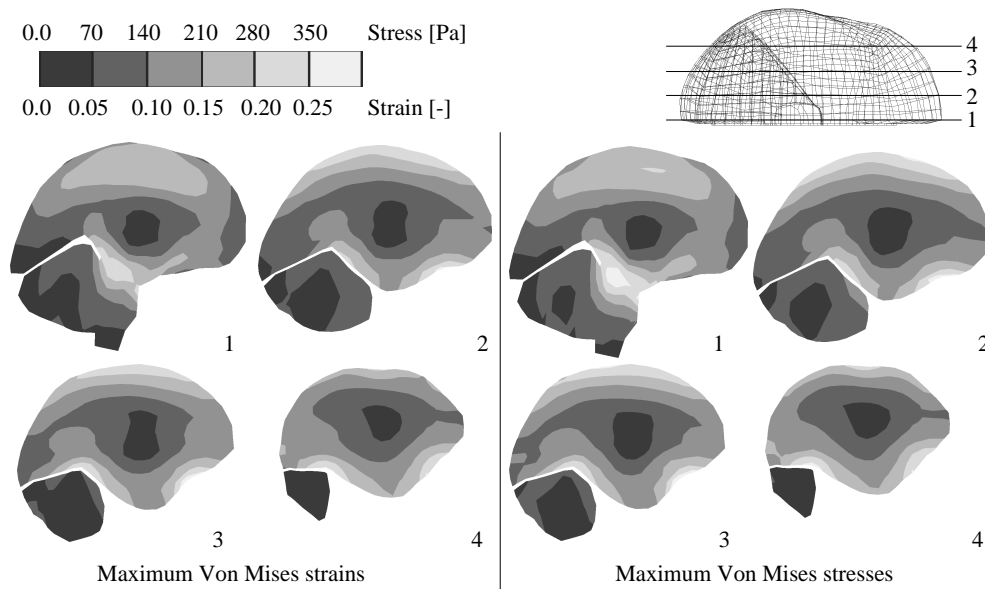


Figure 7.3: Para-sagittal cross-sections (1 to 4) showing Von Mises strains (left) and stresses (right) in the brain section of the three-dimensional head model in reference simulation (REF). Maximum values appearing during complete impact time history are shown.

remain relatively high.

The pressure response of the REF model is shown in Figure 7.5. The upper contour plot, in the left part of Figure 7.5, shows the pressure distribution at $t = 5 \text{ ms}$, which is at maximum positive angular acceleration. Positive pressures arise in the posterior region while negative pressures are present in anterior region. The lower plot is taken during maximum deceleration of the head, at $t = 20 \text{ ms}$. It can be seen that pressures in anterior and posterior region changed sign while absolute values are lower than during acceleration. In both plots the spatial pressure gradient in A-P direction is nearly a constant. This is also true for other moments in time not shown in Figure 7.5.

To study the pressure time history, two elements were selected located on posterior (P) and anterior (A) regions (see left plot of Figure 7.5). The pressure time histories in both P and A element are plotted in the right part of the figure. As seen in the contour plots, the pressures differ in sign. Their time behaviour follows the rotational acceleration input history of Figure 7.2. The largest pressure difference between P and A element occurs at 5.0 ms and equals 27.8 kPa .

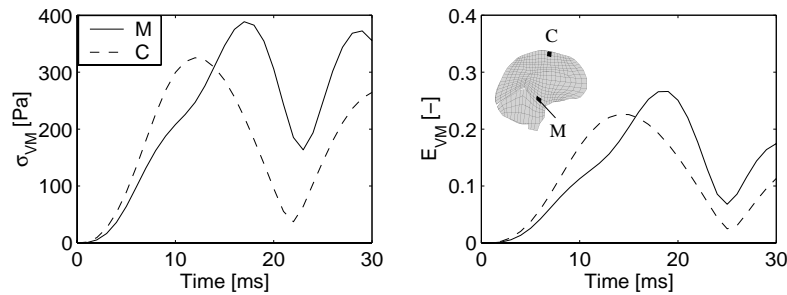


Figure 7.4: Time histories of Von Mises stress (left) and Von Mises strain (right) in two elements located in Mid-brain region (M) and superior cerebral Cortex region (C).

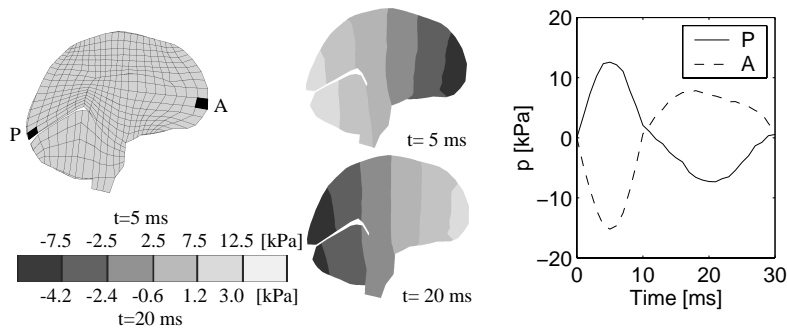


Figure 7.5: Pressure response of the brain in reference simulation (REF). Right: Time history of pressure in two elements at posterior (P) and anterior (A) region. Center: Pressure contour plots with different scaling at $t = 5 \text{ ms}$ and $t = 20 \text{ ms}$.

7.3.2 Model variants: cpl and sof

Figures 7.6 and 7.7 show contour plots of maximum values of Von Mises strains and stresses for all model variants. The SOF variant provides approximately the same spatial distribution of maximum Von Mises stresses and strains than the REF model. However, maximum strain values increase by approximately 21% whereas maximum Von Mises stresses tend to decrease by 11%.

The CPL variant clearly provides completely different stress and strain patterns than the REF model. Strain levels are lower by a factor of 10 and the concentric patterns present in REF and SOF are less evident. The Von Mises stresses are higher by

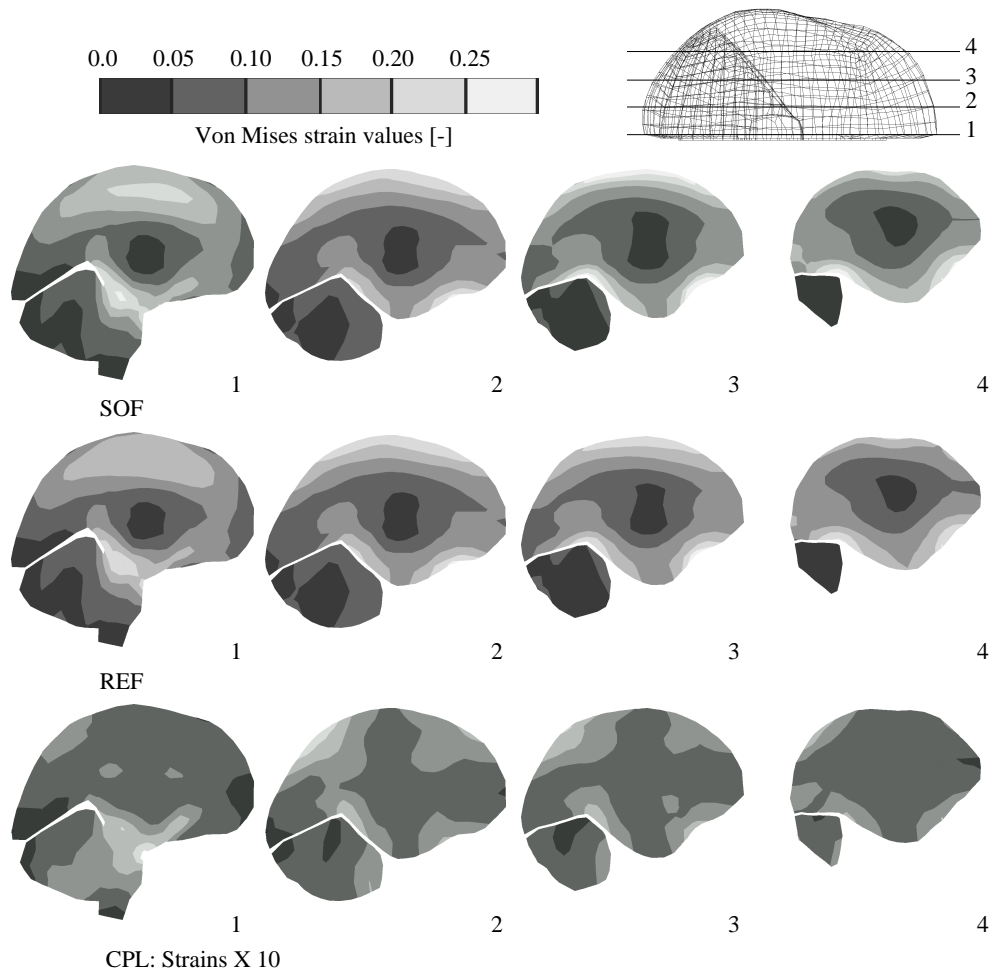


Figure 7.6: Para-sagittal cross-sections (1 to 4) showing maximum values of the Von Mises strains in the brain section of the three-dimensional head model. Top row, SOF: shear softening. Middle row, REF: reference simulation. Lower row, CPL: coupled hydrostatic part (strains $\times 10$).

approximately a factor of five but the concentric pattern remains present.

The Von Mises stress and Von Mises strain time histories for the element located in the mid-brain region selected previously (M) are shown in Figure 7.8. The left plot shows that the maximum strain level increases in the SOF simulation whereas it occurs later in time. The stress history in the right plot, shows that shear softening leads to decreasing maximum stresses which again appear later in time than in the REF simulation.

The results of the CPL variant differ strongly from the reference results. The Von Mises strain values remain close to zero during the complete simulation while the

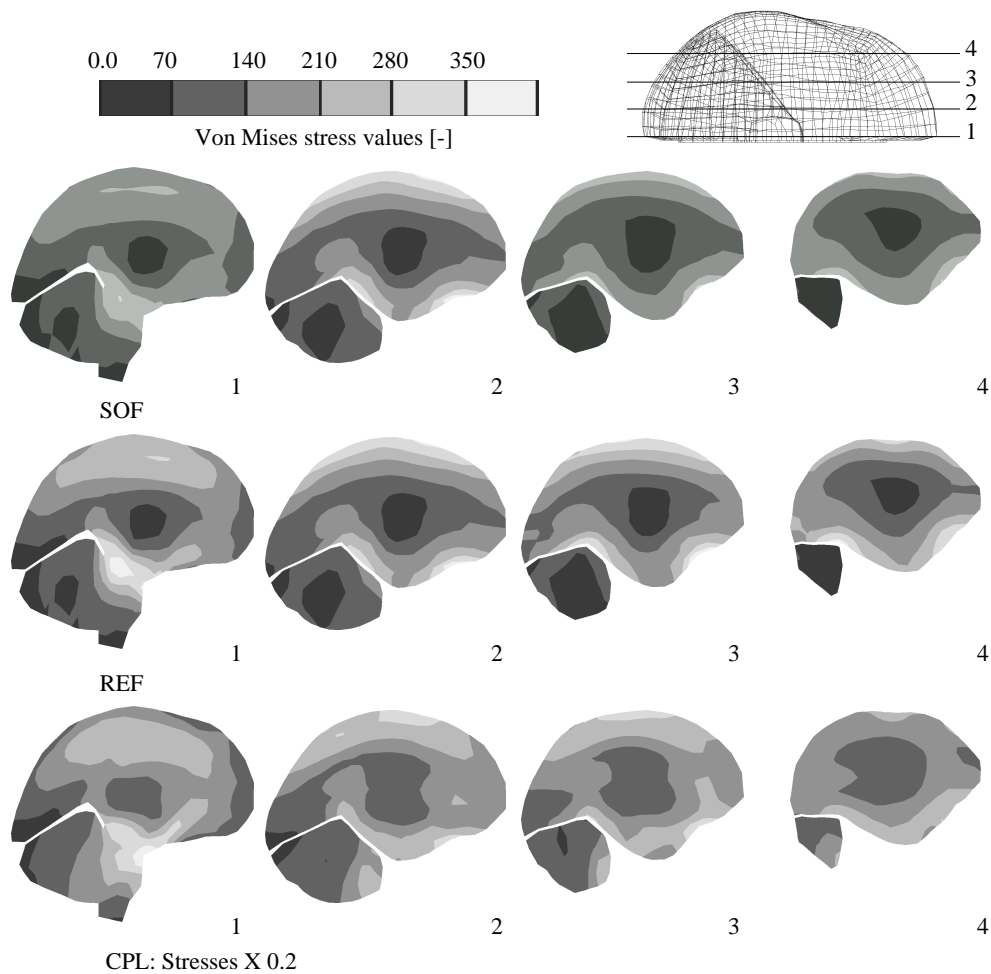


Figure 7.7: Para-sagittal cross-sections (1 to 4) showing maximum values of the Von Mises stresses in the brain section of the three-dimensional head model. Top row, SOF: shear softening. Middle row, REF: reference simulation. Lower row, CPL: coupled hydrostatic part (stress $\times 0.2$).

stress shows high peaks. Furthermore higher frequencies seem to be present in both stress and strain histories.

The spatial pressure response shows constant gradients for all model variants and is therefore not plotted. The pressure time history of elements located in anterior (p_A) and posterior region (p_P) is shown in Figure 7.9 as well as the pressure difference, $\Delta p = p_P - p_A$. Since the spatial pressure gradient is a constant in posterior-anterior direction, the pressure difference over head length provides a measure for the pressure gradient. The effect of shear softening on the pressure response is negligible (maximum difference 0.3 Pa). The element pressure histories of the CPL model variant differ completely from the reference model; the time history does not follow the input angular acceleration any more. Instead the pressure shows an oscillatory history that remains mainly negative for both posterior and anterior element. However, the A-P pressure difference in the CPL model equals the one obtained with REF variant within 2 kPa.

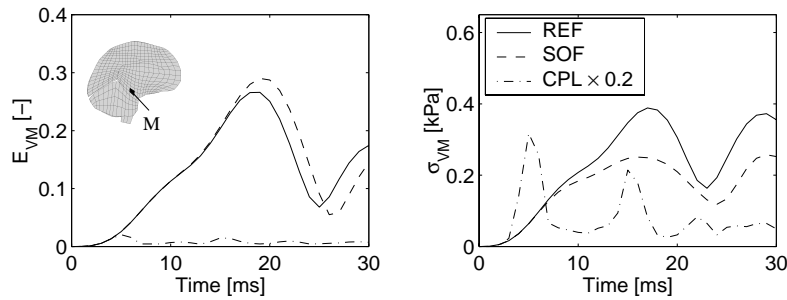


Figure 7.8: Effect of brain tissue modelling variants, Von Mises strain (left) and Von Mises stress (right) histories of element in mid-brain region (M). Note: $\sigma_{VM} \times 0.2$ at CPL result.

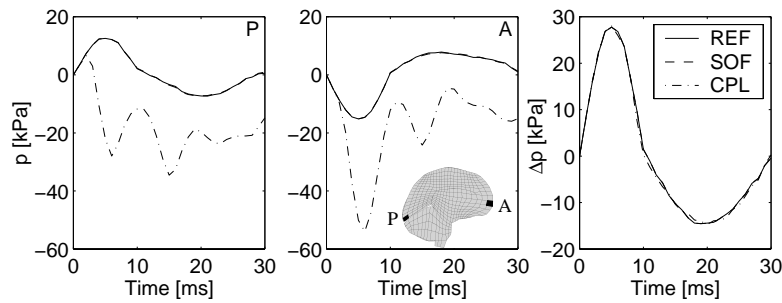


Figure 7.9: Pressure time histories of elements located in posterior (P) (left) and anterior (A) region (center) as well as pressure difference: $\Delta p = p_P - p_A$ (right) to illustrate the effect of brain tissue modelling variants.

7.4 Discussion

In this chapter three modelling variants of the constitutive behaviour of brain tissue are applied in an existing Finite Element head model. The effects on the response caused by shear softening and by the decoupling of hydrostatic and deviatoric deformation in the brain tissue material model have been investigated. Other model assumptions such as geometry and constitutive behaviour of different parts of the head were left unaltered. As such the conclusions presented hold within the current head model. Extrapolation to reality depends on the quality of the other model assumptions which were not subject of research in this chapter.

7.4.1 Numerical model accuracy

The accuracy of the Finite Element procedure used, is determined by time-step and the mesh density. In Chapter 2 it is shown that maximum accuracy is reached when the time step is chosen close to the required step for stability. For this reason the maximum allowable time step in MADYMO was used. The mesh density will be characterized by the number of elements over the head diameter. For the brain section in the model 20, 22 and 22 elements are used in anterior-posterior, superior-inferior and lateral direction respectively. In Chapter 6 it was concluded that typically 28 elements over the diameter are needed for accurate prediction of the dynamical response of a physical model. As a result, the computed solutions will not be at maximum accuracy. This is especially true since the required mesh density was obtained in a homogeneous model, without substructures of different stiffness and mass density as is the case in the head model. However, for practical reasons the use of a higher mesh density has been omitted. Furthermore, it was shown in Chapter 6 that a coarse mesh (11 elements per diameter) did not alter the nature of the response. For this reason it is believed that the response predicted by the model will reflect trends due to different material modelling correctly.

In the head model, linear (constant strain) elements with reduced integration and lumped mass matrixes are used. Although computational effective, these elements allow zero energy modes or hourglass modes to be present which can be suppressed by adding a small stiffness capable of stopping the formation of the anomalous modes but having negligible effect on the stable global modes. No details on the hourglass suppression method in MADYMO were found, but examples of suppression methods can be found in [52] and [78]. During the simulations in this chapter, the hourglass suppression routine contributed less than 4.5% to the total internal energy of the model.

7.4.2 Reference model response

The level of the angular velocity used, is chosen as to obtain strains within the range for which the material properties measured are valid (20% maximum engineering shear strain). The resulting maximum acceleration equals 750 rad/s^2 and the angular velocity equals 5 rad/s . This is lower than typically used in other model

studies. Bandak & Eppinger (1995) applied the same time history with maximum rotational velocity set to 35 rad/s and found principal strains on the order of 0.1 [11]. Application of this loading history on the present REF model leads to maximum principal strains and Von Mises strains exceeding 1.0. Zhang *et al* (2001) modelled a direct impact and found maximum shear strains on the order of 0.06 [167]. Unfortunately no acceleration histories were provided.

To explain the discrepancy between present findings and those in literature, the levels of shear moduli used will be investigated. The material parameters used in present model were obtained from the brain material data in Chapter 4. This data was within range of that found in recent literature. However, older literature data suggests that the shear modulus of brain tissue is much higher. The shear moduli used in head models in literature are often based on this older data and are at least a factor of ten higher than those used here [11; 37; 72; 99; 167; 169].

To illustrate the effect of higher shear moduli in present model, a simulation was performed using a single mode linear variant of the new material model. Material parameters for brain tissue as used by Zhang *et al*. [167] were taken: $G_0 = 7.1 \text{ kPa}$, $G_1 = 30.4 \text{ kPa}$, $\lambda_1 = 1.43 \text{ ms}$ and $K = 2.19 \text{ GPa}$. The time duration and maximum angular velocity were set to the average values used by Bandak & Eppinger [11]; 20 ms and 25 rad/s respectively. This results in a maximum angular acceleration of 6000 rad/s^2 . The maximum Von Mises strains equal approximately 0.15, which is within the expected range especially since the moduli used here were on the lower bound of those found in literature. For this reason it can be concluded that the discrepancy in strain levels between the present model and those in literature, most likely originates from the shear moduli used.

Pressure response In Chapter 2 it was analytically estimated that the frequencies present in traffic related impacts are too low for pressure waves to exist inside brain tissue. This has been verified using the simulation results in this chapter. The contour plots show that the pressure distribution over the brain displays a nearly constant gradient. The posterior-anterior pressure difference qualitatively follows the linear acceleration time history of the head. This indicates a quasi-static pressure response. In that case, the pressure difference at a certain moment in time, $\Delta p(t)$, can be estimated from the balance of momentum as,

$$\Delta p(t) = \rho \ddot{x}(t)l \quad (7.1)$$

in which $\ddot{x}(t)$ equals the linear acceleration, ρ the mass density and l a typical length measure. The linear acceleration can be estimated from the product of the angular acceleration and the neck length (155 mm), while the head length (195 mm) serves as typical length measure, l . Inserting the maximum angular acceleration 750 s^{-2} , at $t = 5 \text{ ms}$, provides an estimated Δp of 24 kPa which agrees qualitatively with the maximum value in Figure 7.9, $\Delta p = 28 \text{ kPa}$.

The pressure difference is independent of the material behaviour assumed in both numerical results and quasi-static theory. Furthermore, it was shown in Chapter 2 that the pressure distribution poses the least demands on numerical accuracy due to its high wave propagation velocity. For these reasons it can be concluded that pressure

difference is not a critical measure for testing the quality of both material model and numerical model during traffic related impacts.

7.4.3 Variation of material models

Shear softening The contour plots in Figures 7.6 and 7.7 reveal that the shear softening does not alter the overall pattern of the stress and strain field present in the head, however the level of stress and strain quantities is changed. The histograms in Figure 7.10 show the distribution of maximum Von Mises stress and strain values for all elements inside the brain. The left plot shows that, due to shear softening, higher Von Mises strains occur in favor of strains in the region of 0.12 to 0.2. The Von Mises stress distribution, shown in the right plot, shifts to lower values despite the larger strains. Also the time history of stresses and strains shown in Figure 7.9 changes in level but not in shape. The pressure response was not significantly changed by application of the shear softening. This is as expected since shear softening acts on the deviatoric part of the stress only.

Coupling deviatoric and hydrostatic parts The decoupling of deviatoric and hydrostatic parts of the stress has large influence on spatial and temporal stress and strain distribution. As seen in Figure 7.10, the coupled LINVIS model present in MADYMO 5.4.1 provided low strains with high stresses. This trend agrees with the results of the physical model simulations in Chapter 6. In that chapter it was concluded that stresses were over predicted when an isochoric deformation was enforced. It can be concluded that, even when surrounded by a relatively compressible modelled skull-brain interface, coupling of deviatoric and hydrostatic deformation parts in the stress formulation leads to severe overestimation of the stress while the strain is underestimated.

The pressures in posterior and anterior brain region showed large differences with

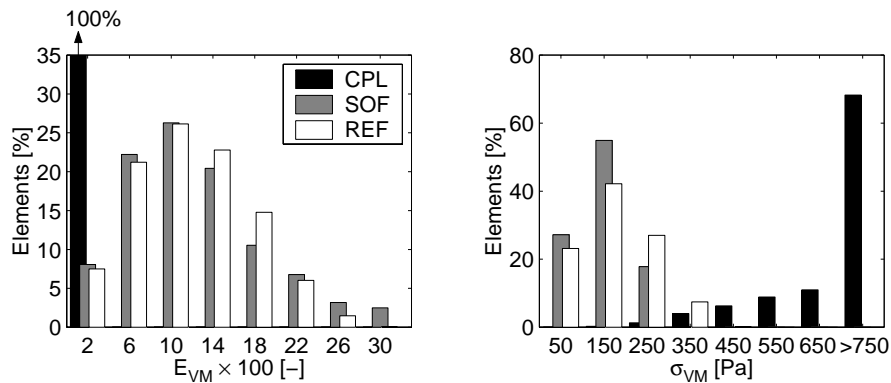


Figure 7.10: Histograms showing the distribution of maximum Von Mises strain, E_{VM} (left) and maximum Von Mises stress, σ_{VM} (right) over the elements in the brain. Results of all modelling variants shown.

respect to the reference simulation. The pressure response did not follow the input angular acceleration anymore. However, posterior-anterior pressure differences were similar to the reference simulation, indicating that conservation of momentum has been satisfied.

7.5 Conclusions

In this chapter, it is investigated how the choice of brain constitutive model affects the dynamic response of brain tissue in a three-dimensional head model. Effects of shear softening and decoupling of deviatoric and hydrostatic behaviour on the response have been investigated leading to the following conclusions:

- Shear softening mainly influences the levels of deviatoric strain and stress but not their spatial and temporal distributions.
- The decoupling of deviatoric and hydrostatic parts of the deformation in the stress formulation has large influence on both spatial and temporal distribution of stress and strain. Using a fully coupled model (linearly coupling second-order Piola-Kirchhoff stress to Green-Lagrange strain) causes severe overestimation of material stiffness for nearly incompressible materials such as brain tissue.
- With the fully decoupled model large strains at modest impact conditions were found. This is probably caused by the shear stiffness used which were a factor 10 lower than those used in head models in literature but comparable to recent material measurement data on brain tissue.
- The pressure history, and especially the pressure gradient history is a poor measure for determining the quality of a head model, as often done in literature. During the load applied in present study, which is typical for traffic related impacts, the pressure gradient is completely determined by the equilibrium of momentum, and thus independent of the choice of the brain material model.

Chapter 8

Discussion, Conclusions and Recommendations

In this Chapter, an integral discussion of the results of the previous chapters will be provided. Conclusions will be drawn and recommendations for further study will be provided.

8.1 Introduction

The head is identified as the body region most frequently involved in life-threatening injury in crash situations [46]. For a better understanding of the way in which an external mechanical load applied on the head during an impact leads to brain injury, the internal mechanical response of the brain tissue has to be known. Finite Element head models are an important tool for assessment of the internal mechanical response in various research strategies. This research aims to contribute to the improvement of these FE models. The objectives of this research were formulated in Chapter 1 as:

- to investigate the accuracy of numerical methods commonly used for predicting brain response (explicit FEM) in crash impact, especially in relation to wave propagation,
- to develop a constitutive model for describing the nearly incompressible, non-linear viscoelastic behaviour of brain tissue in a Finite Element model,
- to assess the effects of non-linear material behaviour on the internal mechanical response by applying the constitutive model in a 3-D Finite Element model, and
- to discuss the consequences of this research for current state of the art head modelling.

Developments on spatial and temporal discretisation methods used in the Finite Element Method were not a topic of this research. In section 8.2 the way in which these objectives were met are discussed. Then conclusions will be drawn in section 8.3. Finally, recommendations for future research will be provided.

8.2 Discussion

8.2.1 Requirements for the numerical accuracy of FE head models

The internal mechanical response of the head may be either of wave propagation nature or of structural dynamics nature, depending on the type of impact on the head. The modelling requirements for wave phenomena are higher than for modelling a structural dynamics response since higher strain gradients are present over smaller volumes of material. The relevance of wave propagation in the internal mechanical response was investigated on the basis of a small strain analysis in Chapter 2. It was found that shear waves (S-waves) can be expected during a traffic related impact, (frequencies between 25 and 300 Hz), while compressive waves (P-waves) are expected during short duration, high velocity, ballistic impacts (frequencies between 10 kHz and 3 MHz). For this reason FE head models should be capable of accurate replication of strain wave propagation inside brain tissue.

When modelling wave propagation using the explicit Finite Element Method with reduced integrated elements and lumped mass matrices (common in crash research FE modelling) two types of error appear in the solution: numerical dispersion and

spurious reflection due to mesh inhomogeneities. These errors cause the predicted wave propagation velocity to be too low and strain and strain rate levels will deviate from reality. These errors can be reduced by choosing spatial discretisation sufficiently small. From one-dimensional simulation results in Chapter 2 it was estimated that at least 24 elements per maximum wave length are required for reducing the error in wave propagation velocity to less than 1%. The errors in strain and strain rate, which increase with distance traveled, then equal 1% and 2.5% respectively after a wave has traveled 1.66 its maximum wavelength. The physical model simulation results in Chapter 6 indicate that this mesh density requirement is also valid for a three-dimensional deformation situation. The error made by applying the Central Difference time integration scheme proved to be compensatory for the error by the spatial discretisation. For this reason the time step was kept as large as possible, but within the range for obtaining a stable solution (Courant number close to 1).

8.2.2 Brain tissue constitutive behaviour: experiments and model

In Chapter 3, the small strain behaviour of porcine brain tissue was determined using oscillatory shear experiments on a rotational plate-plate viscometer. Frequencies to 1000 Hz could be obtained using the Time/Temperature Superposition principle. The large shear strain behaviour was investigated in Chapter 4, at strain levels associated with the occurrence of injury (20% shear strain [141]). Stress relaxation experiments were performed since these allow interpretation of the experimental results at constant strain without making constitutive choices beforehand. Brain tissue showed shear softening (i.e. decrease in stiffness) for strains above 1% (approximately 35% softening for shear strains up to 20%) while the time relaxation behaviour was nearly strain independent. The validity of the time-strain factorization is valid still needs to be investigated for frequencies above 10 Hz , especially since recent experimental data suggests that time-dependent non-linearities might be present in brain tissue at higher frequencies [39].

A non-linear viscoelastic material model for the large strain behaviour of brain tissue in impact conditions has been presented in Chapter 5. Hydrostatic and deviatoric parts of the strain are separated in the stress formulation. The hydrostatic part is assumed to be linear elastic and depends on volumetric deformation only. The inelastic, time dependent behavior is described with a simple Newtonian law that acts on the deviatoric stress contribution only. The shear softening observed is described by the deviatoric elastic part which is modelled by a non-linear second-order Mooney-Rivlin model, based on isochoric deformation only. The constitutive behaviour is formulated in differential form, in which the Cauchy stress is calculated in a total Lagrangian formulation. This allows easy alterations to both elastic and viscous behaviour when needed. Furthermore, in contrast to an incremental Updated Lagrangian approach commonly used, no time-step dependent approximation errors are introduced when large rotations are present. To this authors knowledge this is the first time that a non-linear viscoelastic model is implemented in this manner in an explicit Finite Element code. Brain tissue material parameters were obtained from small strain oscillatory experiments and the constant strain part from the stress

relaxation experiments.

The deviatoric part of the model has been tested by 3-D simulations of the rotational viscometer stress relaxation experiments including the transient loading part. It was found that the model captures the mechanical phenomena observed experimentally, shear softening and viscous behaviour, for strains within the experimental region i.e. shear strains up to 20%. For strains outside this region the model is not validated. In fact, for simple shear exceeding 20% shear strain the model predicts a negative tangential stiffness. To prevent this from happening, the constitutive model was extended with third order terms. For shear strains over 40% the extended model predicts shear stiffening behaviour instead of shear softening which is probably not realistic for brain tissue (refer to Appendix B). Furthermore it is unknown whether the method used for preventing negative tangential stiffness is valid for every arbitrary deformation.

The importance of correct separation of deviatoric and volumetric parts of the deformation in the stress formulation was illustrated in simulations of physical model experiments (Chapter 6). In these experiments, a cylindrical cup filled with silicone gel, mimicking the brain material, was subjected to a transient rotation. It was shown that the model could predict measured gel displacement within 20% error range. Application of a material model without correct decoupling of isochoric and volumetric strain parts in the formulation, clearly showed that the response in a closed geometry was severely underestimated resulting in a nearly rigid body like motion of the gel.

8.2.3 Application in a three-dimensional head model

The non-linear material model was applied in a three-dimensional head model in Chapter 7. The external mechanical load on the 3-D FE head model (an eccentric rotation) was chosen such as to obtain strains within the validity range of the material model (i.e. up to to the tissue level tolerance level of 20% shear strain). It was observed that, in the head model, the tissue tolerance level was reached at external loading values below the ones associated with injury in literature (e.g. in [109]).

This discrepancy may be partly explained by the fact that shear stiffness in the model is low compared to that in other models presented in literature. However, the stiffness values used are considered to be realistic since they fit the experimental data well (see Chapter 5), while the experimental data is in range of material data found in recent literature (see Chapter 3).

Another possible explanation may be that hydrostatic and deviatoric parts of the deformation are completely decoupled in the stress formulation, which has not been verified experimentally. An indication for the presence of some degree of coupling is provided by the simulation results of the physical model in Chapter 6. The gel response in the open cup was less overestimated than in the closed cup. This indicates that, at least for the silicone gel used, volumetric behaviour (open versus closed cup) influences deviatoric behaviour (shear strain levels) in the physical model.

Finally the reason for limiting the validity of the material model to 20% shear strain can be discussed. This range was based on two observations: first, obtaining reliable

experimental data at strains outside this range was not possible with current test setup, second, a 20% strain threshold for axonal injury was found in literature [141]. For this reason it was assumed that 20% strain represents an upper boundary for strains present in brain tissue during impact of the head. However, in a recent study there was no evidence of mechanical damage during brain tissue stress relaxation experiments up to 50% [123]. This implies that strain values exceeding 20% shear strain might be present during head impact.

The effect of shear softening on the brain response was investigated by applying the material model with and without shear softening in the head model. The results showed that maximum Von Mises strain values increased by approximately 21% whereas maximum Von Mises stress values decreased by approximately 11% when shear softening was applied. When interpreting these differences it should be noted that maximum strain levels were concentrated in relatively small areas inside the model. As a result, only a small fraction of the brain material experiences strains large enough to be influenced by shear softening. Furthermore, it should be noted that these differences hold for one specific loading condition in one specific model only.

8.2.4 Consequences for head modelling

In Chapter 2 it is concluded that wave propagation is likely to occur during impacts on the head. For this reason, head models should be capable of accurate prediction of wave propagation. When using explicit FEM, this accuracy depends on element size used. In current state of the art 3-D human head models the element size equals typically 5 mm. This means that S-waves can be modelled accurately for frequencies up to 42 Hz, about one tenth of the upper relevant frequency for S-waves to be present in the head. P-waves can be modelled for frequencies up to 13 kHz, about one hundredth of the upper relevant frequency for P-waves to exist. This means that none of these models will accurately predict wave propagation. As a result, computed maximum strain values and strain rate values will be incorrect. Both quantities are associated with the occurrence of brain injury (refer to Table 1.1 in Chapter 1) and should be predicted correctly.

Despite the limited accuracy of current head models, reported validation results suggest good performance of these models. The reason for this is that current 3-D head models are almost exclusively tested against pressure data obtained by Nahum *et al.* [104] from human cadavers subjected to frontal impact. The duration of this impact is typical for traffic related impacts and equals approximately 8 ms. This is too long to introduce P-waves. As a result, a constant spatial pressure gradient will occur which is completely determined by the equilibrium of momentum, and thus independent of the choice of the brain material model. This has been confirmed by the invariance of the pressure (gradient) response on the material model used in the numerical model results in Chapter 7. Correct simulation of this pressure response, does not imply correct simulation of shear wave response.

In current 3-D head models, brain tissue is modelled as a linear viscoelastic solid. The simulation results with the non-linear material model in Chapter 7 indicate

that the reported strain values, obtained with linear models, are under estimated while stress values are overestimated. However, the validity of these conclusions in different models and loading conditions is not straight forward due to many differences between models such as different skull-brain interface models, different (linear) material parameters, etc.

8.3 Conclusions

- Wave propagation is likely to be present during impacts on the head. Dilatational (P) waves will propagate during ballistic impacts whereas distortional (S) waves will propagate during traffic related impacts.
- For correct numerical modelling of propagation of both P-waves and S-waves, in explicit FE models, typically 24 elements per wavelength should be used. Furthermore the time step should be chosen as large as possible, i.e. the Courant number should be close to 1.
- Spatial discretisation in current 3-D Finite Element head models is too coarse to model wave propagation accurately. As a result, predicted maximum strain levels and strain rate values will deviate from the real solution.
- Pressure history, measured in traffic related impact experiments is often used to assess FE head model quality. Since pressure history during traffic related impacts is completely determined by static equilibrium of momentum, it is not a critical measure for testing.
- For simple shear, brain tissue behaves as a non-linear viscoelastic solid. It displays shear softening (i.e. decrease in stiffness) for strains above 1%.
- The time relaxation behaviour of brain tissue is nearly strain independent. However, for frequencies above 10 Hz this remains to be investigated.
- A three-dimensional non-linear viscoelastic material model that describes the shear softening observed in brain tissue under simple shear has been developed and implemented in the explicit MADYMO FE code. It has been shown that the model is capable of predicting realistic deformations by simulating physical model experiments and material experiments.
- The material model has been applied in a three-dimensional head model for a single loading case. It was found that shear softening influences mainly strain and stress levels but not their temporal and spatial distribution. Differences in pressure history were negligible.

8.4 Recommendations

8.4.1 Numerical quality, validation of head models

Head models in explicit FEM can be made suitable for modelling S-waves by reducing the mesh size to 0.5 *mm*. This seems feasible considering the rapid advances in computer hardware. However, for P-waves, reducing the mesh size to 0.05 *mm* is not a realistic option. Instead alternative spatial discretisation methods should be pursued such as the use of elements with quadratic displacement functions or generalised mass matrix. Another method for increasing mesh density while maintaining realistic computational costs is the use of two-dimensional head models. A trend can be seen towards the development of two-dimensional head models that represent a cross sectional area of the head with very detailed geometry [100; 110]. However, additional assumptions on stress and strain boundary conditions are needed (plain stress / plain strain). Furthermore, out of plane phenomena cannot be studied in this type of models.

Validation methods for head models for traffic related impacts should focus on the deviatoric strain response. A potential method to gain data on the deviatoric strain response in biological models is the MRI tagging method [43]. In principle this method enables non-invasive quantification of the strain field inside the brain in animal experiments with high spatial resolution. However, application in the high frequency range is not trivial and requires further investigation. A different source of data from ongoing research are human cadaver experiments in which high speed x-ray marker tracking techniques are used [3]. Drawbacks of this method are the invasiveness (application of physical markers is required) and the low spatial resolution that can be reached. However, its main advantage is the high temporal resolution, sufficient for impact recording. Finally, the present research showed that physical models can be used to obtain more insight in the presence of numerical artefacts when they are designed to minimise the number of modelling assumptions and to maximise mechanical accessibility. For this reason the use of physical models in this manner should be encouraged.

8.4.2 Constitutive modelling of brain tissue

The high-strain, high-frequency behaviour of brain tissue has to be determined. Inertial effects will have to be taken into account during analysis of the high frequency experimental data. This makes the analytical correction of the inhomogeneous strain field applied in the rotational viscometer impossible. For this reason it is recommended to use a translating shear device that better approximates the homogeneous simple shear conditions (see e.g. [39; 123]). Furthermore such device allows the investigation of anisotropic material behaviour inside brain tissue. Also the validity range of the material model has to be increased up to at least 50% [123]. The interaction between hydrostatic compression and deviatoric response in brain tissue has to be investigated. For this reason material experiments in future studies should aim at acquiring three-dimensional stress data by for instance recording the

normal force during stress relaxation experiments.

The simple shear deformation, applied in the material experiments, is insufficient to reveal the complete constitutive behaviour of brain tissue. Using a different deformation mode, such as unconfined compression, allows determination of the remaining material parameters.

Finally, the non-linear viscoelastic material model has to be applied in a three-dimensional head model under different impact conditions. This will provide more insight in the effect of the non-linear constitutive model on stresses and strains in the brain.

8.4.3 Geometry and interface description in head models

The work in this thesis focused on numerical quality of head models and constitutive modelling of brain tissue. The strain field inside the head (and so the effect of shear softening) is also influenced by geometry and the interfaces present between the various parts of the brain (e.g. meninges and CSF, tentorium, falx).

Insight in the effect of geometrical detail on the internal response can be gained using physical models [24; 71; 157]. It has been shown that, for example, the presence of the CSF filled ventricles in the brain can reduce strain levels inside brain tissue by 40% [71].

FE simulations of physical model experiments indicate that introducing relative motion between skull and brain leads to strain reduction at smooth parts of the brain whereas strain increases at relatively sharp invaginations such as the falx [34; 55; 149]. In the FE head model used in Chapter 7, the sliding effect in the skull-brain interface is modelled by using a single layer of elements with low shear modulus tied to the brain tissue as done previously by various authors [72; 99; 167]. It has been shown that this method does not suffice to predict the relative motions observed experimentally [3].

For this reason a more realistic manner of modelling the skull-brain interface should be investigated. However, detailed insight in the mechanics of the skull-brain interface is still lacking. A problem in this is that the effect of this interface depends on the pressure in the CSF which depends on blood pressure. For this reason experiments on *in-vivo* biological models should be aimed for. The internal response then should be measured by preferably a non-invasive method such as MR tagging [43].

References

- [1] Achenbach, J.D. (1973): *Wave Propagation in elastic solids*, North-Holland publishing company, London, Amsterdam, Elsevier publishing company, inc, New-York.
- [2] Adams, J.H., Graham, D.I., and T.A. Gennarelli (1983): "Head injury in man and experimental animals: neuropathology", *Acta Neuro chir.*, **32**, pp.15-30.
- [3] Al-Bsharat, A.S., Hardy, W.N., Yang, K.H., Khalil, T.B., Tashman, S. and A.I. King (1999): "Brain Skull Relative Displacement Magnitude Due to Blunt Head Impact: New experimental Data and Model", *Proceedings of the 43th Stapp Car Crash Conference*, Paper no. 99sc22, pp. 321-332.
- [4] Arbogast K.B, Meaney, D.F. and L.E. Thibault (1995): "Biomechanical Characterization of the Constitutive Relationship for the Brainstem", *Proceedings of the 39th Stapp Car Crash Conference*, SAE Paper 952716, pp.153-159.
- [5] Arbogast, K.B. and S.S. Margulies (1997): "Regional Differences in Mechanical Properties of the Porcine Central Nervous System", *Proceedings of the 41st Stapp Car Crash Conference*, SAE Paper 973336, pp. 293-300.
- [6] Arbogast, K.B., Thibault, K.L., Pinheiro, B.S., Winey, K.I. and S.S. Margulies (1997): "A high frequency shear device for testing soft biological tissues", *Journal of Biomechanics*, **7**, pp. 757-759.
- [7] Arbogast, K.B., Prange, M.T, Meaney, D.F. and S.S. Margulies (1997): "Properties of Cerebral Gray and White Matter Undergoing Large deformation", *Proceedings of the Seventh Injury Prevention through Biomechanics Symposium*, Centers for Disease Control, Wayne State University, USA.
- [8] Arbogast, K.B. and S.S. Margulies (1998): "Material characterization of the brainstem from oscillatory shear tests", *Journal of Biomechanics*, **31**, pp. 801-807.
- [9] Bain, A.C. and D.F. Meaney (1999): "Thresholds for Mechanical Injury to the In Vivo White Matter", *Proceedings of the 43th Stapp Car Crash Conference*, Paper 99SC19, pp. 295-302.
- [10] Bain, A.C. and D.F. Meaney (2000): "Tissue-Level Thresholds for Axonal Damage in an Experimental Model of Central Nervous System White Matter Injury", *Journal of Biomechanical Engineering*, ASME, **122**, pp. 615-622.
- [11] Bandak, F.A. and R.H. Eppinger (1994): "A three-dimensional finite elements analysis of the human brain under combined rotational and translational accelerations", *Proceedings of the 38th Stapp Car Crash Conference*, SAE Paper 942215, pp. 148-163.
- [12] Bandak, F.A. (1995): "On the mechanics of impact neurotrauma: A Review and critical synthesis", *Journal of Neurotrauma*, **12**(4), pp. 635-649.
- [13] Bandak, F.A. (1997): "Impact traumatic brain injuries: a mechanical perspective" in *Neurotraumatology: Biomechanic aspects, Cytologic and Molecular Mechanisms*, eds. M. Oehmichen and H.G. Konig, Schmid-Romhild, pp. 58-83.

- [14] Bandak, F.A., Chan, P.C., Yu, J. and J. Stuhmiller (1999): "Influence of the subarachnoidal cerebrospinal fluid layer on the dynamic response of the brain: an experimental and computational study", in *Injury Biomechanics Research: Proceedings of the 27th human subjects biomechanics workshop*, San Diego, U.S.A., pp. 115-139.
- [15] Bandak, F.A., Zhang, A.X., Tannous, R.E., DiMasi, F., Masiello, P. and R. Eppinger (2001): "SIMon: a simulated injury monitor: application to head injury assessment", *Proceedings of the 17th Int. technical conference on the Enhanced Safety of Vehicles*, Amsterdam, The Netherlands.
- [16] Bathe, K.J. (1996): *Finite element procedures*, Englewood Cliffs : Prentice Hall,.
- [17] Bažant, Z.P. (1978): "Spurious reflection of elastic waves in nonuniform finite element grids", *Computer Methods in Applied Mechanics and Engineering*, **16**, pp. 91-100.
- [18] Bax, P.T.M. (2001): *Pressure wave propagation in tissue model material after ballistic impact, numerical and experimental analysis*, Technical Report, Dynamics and Control Technology, D&C 2001.03.
- [19] Bedford, A. and D.S. Drumheller (1994): *Introduction to elastic wave propagation*, Wiley Publishers, Chichester, N-Y, Brisbane, Toronto, Singapore.
- [20] Belytschko, T. and R. Mullen (1977): "On Dispersive Properties of Finite Element Solutions", in *Modern Problems in Elastic Wave Propagation, Int. Union of Theoretical and Applied Mechanics*, ed by. J. Miklowitz and J.D. Achenbach, Wiley Publishers, New York, Chichester, Brisbane, Toronto, pp. 67-82.
- [21] Bird, R.B., Armstrong, R.C., and O. Hassager (1987): *Dynamics of Polymer Liquids: Vol. 1: Fluid Mechanics*, John Wiley and Sons, N.Y., U.S.A.
- [22] Bolduc, M. and S. Tylko (1998): "Hybrid III head response to undefeated combat helmet in a ballistic environment", presented at the 2nd meeting of the NATO Task Group: Behind Armour Blunt Trauma, Colchester, UK.
- [23] Booij, S.M. (1998): "Optische weergave en kwantificatie van druktgolven in gelatine bij inslag van een projectiel", *Trainee report*, Delft University of Technology, in Dutch.
- [24] Bradshaw, D.R.S., Ivarsson, J., Morfey, C.L. and D.C. Viano (2001): "Simulation of acute subdural hematoma and diffuse axonal injury in coronal head impact", *Journal of Biomechanics*, **34**, pp. 85-94.
- [25] Brands, D.W.A. (1998): "Constitutive modelling of brain tissue (literature review)", *Technical report, WFW 98.020*, Eindhoven University of Technology, Eindhoven, The Netherlands.
- [26] Brands, D.W.A. (1999): "Wave propagation in head impact response: Assessment of physical possibility and numerical artifacts", *Technical report, WFW 99.005*, Eindhoven University of Technology, Eindhoven, The Netherlands.
- [27] Brands, D.W.A., Bovendeerd, P.H.M., Peters, G.W.M., Paas, M., Bree, van J. and J.S.H.M. Wismans (1999): "Comparison of the dynamic behaviour of brain tissue and two model materials", *Proceedings of the 43th Stapp Car Crash Conference*, Paper no. 99sc21, pp. 57-64.
- [28] Brands, D.W.A., Bovendeerd, P.H.M., Peters, G.W.M. and J.S.H.M. Wismans (2000): "The large strain dynamic behaviour of in-vitro porcine brain tissue and a silicone gel model material", *The Stapp Journal*, **44**, pp. 249-260.
- [29] Brands, D.W.A., Bovendeerd, P.H.M., and G.W.M. Peters (2000): "Finite shear behaviour of brain tissue under impact loading", *ASME-WAM, Conf. on Crashworthiness, Occupant Protection and Biomechanics in Transportation Systems*, AMD-Vol. 246/BED- 49, pp.175-188.

- [30] Bree, J. (1999): "Impact duration of soft rubber bullet", personal communication.
- [31] Brooks, C.A., Gabella B, Hoffman R, Sosin D, and G. Whiteneck (1997): "Traumatic brain injury: designing and implementing a population-based follow-up system.", *Arch Phys Med Rehabil*, **78**(8) : S26-S3.
- [32] Carsten, O. and J. Day (1988): "Injury Priority Analysis, Task A.", in *Technical Report DOT HS 807 224*, U.S. Dept. of Transportation National Highway Traffic Safety Administration (NHTSA), Washington D.C., USA.
- [33] Chan, R. K.-C., Maseillo, P.J., and G.S. Srikantiah (1986): "PORTOS-A computer code for solving general three dimensional time-dependent two-fluid equations", *ASME 86-WA/NE-3 Winter Annual Meeting*, Anaheim, CA., USA.
- [34] Cheng, L.Y., Rifai, S., Khatua, T. and R.L. Piziali (1990): "Finite Element Analysis of Diffuse Axonal Injury", *Proceedings of the 34th Stapp Car Crash Conference*, SAE Paper 900547, pp. 141-154.
- [35] Chu, C-S., Lin, M-S, Huang, H-M. and M-C Lee (1994): "Finite element analysis of cerebral contusion", *Journal of Biomechanics*, **27**(2), pp. 187-194.
- [36] Claessens (1997): *Finite Element Modelling of the Human Head under Impact Conditions*, Ph.D. dissertation, Eindhoven University of Technology, Eindhoven, The Netherlands.
- [37] Claessens, M., Sauren, F and J. Wismans (1997): "Modelling of the Human Head under Impact Conditions: A Parametric Study", *Proceedings of the 41th Stapp Car Crash Conference*, SAE 973338, pp. 315-328.
- [38] Courant, R., Friedrichs, K. and H. Lewy (1928): "On the Partial Difference Equations of Mathematical Physics", *Math. Ann*, **100**, pp. 32-74.
- [39] Darvish, K.K. and J. R. Crandall (2000): "Comparison between quasilinear and a nonlinear viscoelastic model for brain tissue", *ASME-WAM Proceedings*, Orlando, Florida, USA.
- [40] DiMasi, F, Marcus, J. and R. Eppinger (1991): "3D anatomic brain model for relating cortical strains to automobile crash loading", *Proceedings of the 13th Technical Conference on the Safety of Experimental Safety Vehicles*, Paper no. 91-S8-0-11, Paris, France.
- [41] DiMasi, F, Eppinger, R. and F.A. Bandak (1995): "Computational analysis of head impact response under car crash loadings", SAE Paper 952718.
- [42] NHTSA (2000): "Federal Motor Vehicle Safety Standards: Standard No. 208; Occupant crash protection", in *Technical Report 49 CFR 571.208*, U.S. Department of Transportation, National Highway Traffic Safety Administration.
- [43] Dougherty, L., Ross, K., Afshar, P. and S.S. Margulies (1999): "Measurements of intracranial tissue distortion during rapid angular motions", *CDC-Proceedings: Injury Prevention through biomechanics*, M.J. Grimm ed., Novi, Michigan, U.S.A, pp.85 - 94.
- [44] Estes, M.S. and J.H. McElhaney (1970): "Response of brain Tissue to Compressive Loading", *ASME Paper*; 70-BHF-13.
- [45] Etoh A., Mitaku, S., Yamamoto, J. and K. Okano (1994): "Ultrasonic Absorption Anomaly of Brain Tissue", *Japanese Journal of Applied Physics*, **33**, pp. 2874-2879.
- [46] European Transport Safety Council (1993): *Report in Motorcycle Safety*, European Experimental Vehicles Committee Ad-Hoc Group.
- [47] European Transport Safety Council (1997): *A strategic Road Safety Plan for the European Union*, Brussels, Belgium.
- [48] European Transport Safety Council (1999): *Exposure Data for Travel Risk Assessment*.

- [49] Ewing, C.L. and D.J. Thomas (1972): "Human head and neck response to impact acceleration", Monograph 21, USAARL 73-1, Naval Aerospace and Regional Medical Centre, Pensacola, USA.
- [50] Fallenstein, G.T., Hulce, V.D. and J.W. Melvin (1969) "Dynamic Properties of Human Brain Tissue", *Journal of Biomechanics*, **2**, pp 217-226.
- [51] Ferry, J. (1980): *Viscoelastic properties of polymers*. John Wiley & Sons, New York, NY, USA.
- [52] Flanagan, D.P. and T. Belytschko (1981): "A uniform strain hexahedron and quadrilateral and orthogonal hourglass control", *International Journal Meths. Engineering*, **17**, pp. 679-706.
- [53] Fung, Y.C. (1970): "Stress strain history relations of soft tissues in simple elongation", in *Biomechanics, its Foundations and Objectives*, Prentice Hall, Englewood Cliffs, NJ.
- [54] Fung, Y.C. (1990): *Biomechanics: motion, flow, stress and growth*, Springer-Verlag, Berlin, Germany.
- [55] Galbraith, C.G. and P Tong (1988): "Boundary Conditions in Head Injury Finite Element Modelling", *Int. Workshop on Human Subjects for Biomechanical Research*, pp. 179-193.
- [56] Galbraith, J.A., Thibault, L.E. and D.R. Matteson (1993): "Mechanical and Electrical Responses of the Squit Giant Axon to Simple Elongation", *Journal of Biomechanical Engineering*, **115**, pp. 13-22.
- [57] Galford, J.E. and J.H. McElhaney (1970): "A viscoelastic Study of Scalp Brain and Dura", *Journal of Biomechanics*, Vol. 3, pp.211-221.
- [58] Ganong, W. (1981): *Review of Medical Physiology*. Lange medical Publications, Los Altos, CA, USA.
- [59] Gennarelli, T.A. (1981): "Mechanistic Approach to the Head Injuries: Clinical and Experimental Studies of the Important Types of Injury", *Head Injury Criteria - A Consensus Workshop*, U.S. Government Printing Office, Washington D.C., USA, pp. 20-25.
- [60] Gennarelli, T.A., Thibault, L.E., Tomei, G., Wiser, R., Graham, D. and J Adams (1987): "Directional dependence of axonal brain injury due to centroidal and non-centroidal acceleration", *Proceedings of the 31st Stapp Car Crash Conference*, SAE Paper 872197, pp.49-53.
- [61] Goldman, D.E. and T.F. Hueter (1956): *Journal of the Acoustical Society of America*, **28**, p.35.
- [62] Goldsmith, W. (1966): "The physical processes producing head injury", *Proceedings of the Head Injury Conference*, Lippincott, pp 350-382.
- [63] Goldsmith, W. and P Lubock (1980): "Experimental Cavitation Studies in a Model Head-Neck System", *Journal of Biomechanics*, **12**, pp. 211-222.
- [64] Gosh, H.H., Gooding, E. and R.C. Schneider (1969): "Distortion and displacement of the brain in experimental head injuries", *Surgical Forum*, 20-425-6.
- [65] Gosh, H.H., Gooding, E. and R.C. Schneider (1970): "The lexan calvarium for the study of cerebral responses to acute trauma", *Journal of Trauma*, **10**, pp. 370-376.
- [66] Gurdjian, E.S., Webster, J.E. and H.R. Lissner (1955): "Observations on the Mechanics of Brain Concussion, Contusion and Laceration", *Surg. Gynecology and Obstetrics*, **101**, pp. 680-690.

- [67] Gurdjian, E.S., Lissner, H.R. and L.M. Patrick (1962): "Protection of the head and neck in sports", *Journal of the American Medical Association*, **182**, pp. 509-512.
- [68] Hardy, W.N., Foster, C.D., King, A.I., and S. Tashman (1998): "Update on the study of headinjury kinematics", *Symposium proceedings*, Centers for Disease Control, pp. 177-184.
- [69] Hodgson, V. R., Mason, M. W. and L.M. Thomas (1972): "Head model for impact", *Proceedings of the 16th Stapp Car Crash Conference*, SAE report 720969, SAE, New York, pp. 1-13.
- [70] Holbourn, A.H.S. (1945): "The mechanics of brain injuries", *Br. Med. Bull.*, **3**, pp. 147-149.
- [71] Ivarsson, J., Viano, D.C., and Lvsund, P and B. Aldman (2000): "Strain relief from the cerebral ventricles during head impact: experimental studies on natural protection of the brain", *Journal of Biomechanics*, **33**, pp. 181-189.
- [72] Kang, H-S., Willinger, R., Diaw, B.M. and B. Chinn (1997): "Validation of a 3D Anatomic Human Head Model and Replication of Head Impact in Motorcycle Accident by Finite Element Modelling", *Proceedings of the 41th Stapp Car Crash Conference*, SAE 973339, pp.329-338.
- [73] Kenner, V.H. and W. Goldsmith (1973): "Impact on a simple physical model of the head", *Journal of Biomechanics*, **6**, pp. 1-11.
- [74] Khalil, T.B. and D.C. Viano (1982): "Critical issues in finite element modeling of head impact", *Proceedings of the 26th Stapp Car Crash Conference*, SAE, pp.87-102.
- [75] Kinsler, L.E., Frey, A.R., Coppens, A.B. and J.V. Sanders (1982): *Fundamentals of Acoustics*, Third Edition, John Wiley & Sons, New-York, p 462.
- [76] Kolsky, H. (1963): *Stress waves in solids*, Dover Publications Inc. New York, U.S.A.
- [77] Krabbel, G. (1998): *Ein rechnerisches Schädel-Hirn-Modell zur Untersuchung dynamischer Belastungen des Kopfes*, Ph.D. dissertation, Technische Universität Berlin, ISBN 3-7983-1767-4, in German.
- [78] Kosloff, D. and G.A. Frazier (1974): "Treatment of hourglass patterns in low order finite element codes", *Int. Journal Anal. Meth. Geomech.*, **2**, pp.57-72.
- [79] Kreyszig, E. (1993): *Advanced Engineering Mathematics*, 7th edition, Wiley, New York
- [80] Lakes, R.S. (1999): *Viscoelastic Solids*, Chapter 2, CRC Press LLC, London, UK.
- [81] Leonov, A. (1976): "Non equilibrium thermodynamics and rheology of viscoelastic polymer media", *Rheologica Acta*, **15**, pp. 85-98.
- [82] Lighthall, J.W. (1988): "Controlled cortical impact: A new experimental brain injury model", *Journal of Neurotrauma*, **5**, pp. 1-15.
- [83] Lin, S-C, Shieh, S-J and M.J. Grimm (1997): "Ultrasonic measurements of brain tissue properties", *Proceedings of the Symposium of the Centers for Disease Control and Prevention*, pp. 27-31.
- [84] Lin, S-C and M.J. Grimm (1998): "Characterization of the mechanical properties of brain tissue using ultrasound", *Proceedings of the Symposium of the Centers for Disease Control and Prevention*, pp. 59-64.
- [85] Lissner, H.R., Lebow, M. and F.G. Evans (1960): "Experimental studies on the relation between acceleration and intracranial pressure changes in man", *Surg. Gynecology and Obstetrics*, **111**, pp. 320-338.

- [86] LSTC (1996): *LS-Dyna User Manual, version 940*, Livermore Software Technology Corporation.
- [87] Macosko C.M. (1993): *Rheology: principles, measurements and applications*, VCH Publishers, USA, Germany and UK.
- [88] MARC Analysis Research Corporation (1994), MARC K6.1.
- [89] MathWorks, Inc. (1999): *Matlab 5.3 User's Guide*, South Natick, MA, USA.
- [90] Margulies, S.S., Thibault, L.E. and T.A. Gennarelli (1990): "Physical Model Simulations of brain Injury in the Primate", *Journal of Biomechanics*, **23**, 8, pp. 823-836.
- [91] McElhaney, J.H., Melvin, J.W., Roberts, V.L. and H.D. Portnoy (1972): "Dynamic characteristics of tissue of the head", *Symposium Perspectives in Biomedical Engineering*, pp. 1-8
- [92] Meaney, D.F., Ross, D.T., Winkelstein, B.A., Brasko, J., Goldstein, D., Bilston, L.B., Thibault, L.E. and T.A. Gennarelli (1994): "Modification of the cortical impact model to produce axonal injury in the rat cerebral cortex", *Journal of Neurotrauma*, **11** (5), pp. 599-612.
- [93] Meaney, D.F., Smith, D.H., Shreiber, D.I. Bain A.C. Miller R.T. Ross, D.T. and T.A. Gennarelli (1995): "Biomechanical Analysis of Experimental Diffuse Axonal Injury", *Traumatic Brain Injury: Bioscience and Mechanics*, Mary Ann Liebert, Inc. pp.167-172.
- [94] Mendis, K.K. (1992): *Finite element modeling of the brain to establish diffuse axonal injury criteria*, Ph. D. dissertation, Ohio State University, USA.
- [95] Mendis, K.K., Stalnaker, R.L. and S.H. Advani (1995): "A constitutive relationship for large deformation Finite Element Modelling of Brain tissue", *Journal of Biomechanical Engineering: Transactions of the ASME*, **117**, pp. 279-285.
- [96] Miller, K. and K. Chinzei (1997): "Constitutive modelling of brain tissue: Experiment and Theory:", *Journal of Biomechanics*, **30** (11/12), pp. 1115-1121.
- [97] Miller, K. (1999): "Constitutive model of brain tissue suitable for finite element analysis of surgical procedures", Technical note in *Journal of Biomechanics*, **32**, pp. 531-537.
- [98] Miller, K., Chinzei, K., Orssengo, G. and P Bernarz (2000): "Mechanical properties of brain tissue in-vivo: experiment and computer simulation", *Journal of Biomechanics*, **33**, pp. 1369-1376.
- [99] Miller, R.T., Margulies, S.S., Leoni, M., Nonaka, M., Chen, X., Smith, D.H. and D.F. Meaney (1998): "Finite element modelling approaches for predicting injury in an experimental model of severe diffuse axonal injury", *Proceedings of the 42nd Stapp Car Crash Conference*, Paper no. SAE 983154, pp. 155-167.
- [100] Miller, R.T., Smith, D.H., Chen, X., Xu, B-N., Leoni, M. Nonaka, M. and D.F. Meaney (1999): "Comparing Experimental Data to Traumatic Brain Injury Finite Element Models", *Proceedings of the 43rd Stapp Car Crash Conference*, Paper no. 99sc20, pp. 303-312.
- [101] Mooney (1940): "A theory of large elastic deformation", *Journal of applied physics*, **11**, pp. 582-592.
- [102] Moore, P. (1997): "A Very Smart Dummy", *New Scientist*, **2089**, pp. 38-42.
- [103] Mullen R. and T. Belytschko (1982): "Dispersion analysis of finite element semidiscretizations of the two-dimensional wave equation", *Int. Journal for numerical methods in engineering*, **18**, pp. 11-29.
- [104] Nahum, A.M. Smith, R.W. and C.C. Ward (1977): "Intracranial pressure dynamics during head impact", *Proceedings 21st Stapp Car Crash Conference*, SAE Paper 770922, pp. 339-366.

- [105] NATO (1981): Evaluation Procedures for future NATO Small Arms Weapon Systems, Report AC/225 (Pane-III) D/14 (redraft 1980).
- [106] Nayfeh, A.H., and B. Balachandran (1995): *Applied Non Linear Dynamics: Analytical, Computational and Experimental Methods*, John Wiley & Sons, New York, USA.
- [107] Newman, J.A. (1980): "Head Injury Criteria in Automotive Crash Testing", *Proceedings of the 27th Stapp Car Crash Conference*, SAE Paper 801317, pp. 701-747.
- [108] Newman, J.A. (1986): "A Generalized Acceleration Model for Brain Injury Threshold (GAMBIT)", *Proceedings of the 1986 International IRCOBI Conference*, Bron, France.
- [109] Newman J., Barr, C., Beusenberg, M., Fournier, E., Shewchenko, N., Welbourne, E., and C. Withnall (2000): "A New Biomechanical Assessment of Mild Traumatic Brain Injury Part 2: Results and Conclusions"; *Proceedings of the 2000 IRCOBI Conference on the Biomechanics of Impact*, Montpellier, France, pp. 223-233.
- [110] Nishimoto, T. and S. Murakami (2000): "Direct impact simulations of diffuse axonal injury by axial head model", *JSAE Review*, **21**, pp. 117-123.
- [111] Nusholtz, G., Glascoe, L.G. and E.B. Wylie (1996): "Modelling Cavitation during Head Impact", *Proceedings of NATO/AGARD Head Impact Conference*, Paper 6.
- [112] Nusholtz, G.S., Glascoe, L.G. and E.B. Wylie (1997): "Cavitation During Head Impact", *Proceedings 41st Stapp Car Crash Conference*, SAE Paper 970390, pp. 151-162.
- [113] Nusholtz, G.S. and Y. Shi (1998): "Physical reality in FE head models: rotation and strain", *Proc. Mech. of Protection*, SP-1355, Paper no. SAE 980355, pp.37-54.
- [114] Ommaya A.K. (1988): "Mechanisms and Preventive Management of Head Injuries, a Paradigm for Injury Control", *Proceedings 32nd AAAM conference*.
- [115] Ommaya, A.K., Thibault L., and F.A. Bandak (1994): "Mechanisms of Impact Head Injury", *International Journal of Impact Engineering*, **15**(4), pp. 535-560.
- [116] Ono, K., Kikuchi, A., Nakamura, M., Kobayashi, H. and N. Nakamura (1980): "Human head tolerance to sagittal impact: reliable estimation deduced from subhuman primates and human cadaver skulls", *Proceedings 24th Stapp Car Crash Conference*, SAE Paper 801303, pp. 101-160.
- [117] PAM-CRASH, PAM Systems International, ESI group.
- [118] Pamidi M.R. and S.H. Advani (1978): "Nonlinear Constitutive Equations for Human Brain Tissue", *transactions of the ASME*, **100**, pp. 44-48.
- [119] Pheasant, S. (1986): *Bodyspace: anthropometry, ergonomics and design*, Taylor & Francis, London.
- [120] Peters, G., Meulman, H and A. Sauren (1997): "Application of the Time Temperature Superposition Theory on Brain Tissue", *Biorheology*, **34**, pp. 127-138.
- [121] Pike, J.A. (1990): *Automotive safety - Anatomy, Injury, Testing and Regulation*, Society of Automotive Engineering, Inc. 400 Commonwealth Drive, Warrendale, PA. 15069-0001, USA.
- [122] Prange M.T. and S.S. Margulies (1999): "Anisotropy and Inhomogeneity of the Mechanical Properties of Brain Tissue at Large Deformation", *Symp. Proc. Centers of Disease Control and Prevention*, Wayne State University, pp. 95-100.

- [123] Prange, M.T., Meaney, D.F. and S.S. Margulies (2000): "Defining Brain Mechanical Properties: Effects of Region, Direction and Species", *The Stapp Journal*, **44**, pp. 205-214.
- [124] Ran, A., Koch, M. and H. Mellander (1984): "Fitting Injury versus Exposure Data into a Risk Function", *Proceedings of the International IRCOBI Conference on the Biomechanics of Impact held at Delft, The Netherlands, Bron, France, 1984*.
- [125] Rheometric Scientific (1993): *Advanced Rheometric Expansion System, ARES*, with 2K FRTN1 force transducer and liquid Nitrogen air temperature control, *Instrument manual*, 902-30004, Piscataway, New Jersey, USA.
- [126] Ruan, J.S., Khalil, T. and A.I. King (1991): "Human Head Dynamic Response to Side Impact by Finite Element Modeling", *Journal of Biomechanical Engineering*, **113**, pp. 276-283
- [127] Ruan, J.S., Khalil, T. and A.I. King (1992): "Finite element analysis of the human head to impact", *Advances in Bioengineering*, ASME-BED 22, pp. 249-252.
- [128] Ruan, J.S., Khalil, T. and A.I. King (1993): "Finite Element Modeling of Direct Head Impact", *Proceedings 37th Stapp Car Crash Conference*, SAE Paper 933114, pp. 69-81.
- [129] Ruan, J.S., Khalil, T.B and A.I. King (1997): "Impact Head Injury Analysis using an Explicit Finite Element Human Head Model", *Journal of Traffic Medicine*, **25** (1/2).
- [130] Sauren, A.A.H.J. and M.H.A. Claessens (1993): "Finite element modelling of head impact: The second decade", *Proceedings of the 1993 International IRCOBI Conference*, pp. 241-254.
- [131] Schreiber D.I., Bain, A.C. and D.F. Meaney (1997): "In Vivo Thresholds for Mechanical Injury to the Blood-Brain Barrier", *Proceedings of the 41th Stapp Car Crash Conference*, SAE Paper 973335, pp. 277-291.
- [132] Shatsky, S., Alter III, W., Evans, D. Armbrustmacher, V., Earle, K. and G. Clark (1974): "Traumatic distortions of the primate head and chest: Correlation of biomechanical, radiological and pathological data", *Proceedings of the 18th Stapp Car Crash Conference*, SAE Paper 741186, pp. 351-381.
- [133] Sheldon, C.H., Pudenz, R. Restarski, J.S. and W.M. Craig (1944): "The lucite clavarium - a method for direct observation of the brain", *Journal of Neurosurgery*, **1**, pp. 67-75.
- [134] Shuck, L. Haynes, R. and J. Fogle (1970): "Determination of Viscoelastic Properties of Human Brain Tissue", ASME Paper, No. 70-BHF-12.
- [135] Shuck, L.Z. and S.H. Advani (1972): "Rheological Response of Brain Tissue in Shear", *ASME Journal of Basic Engineering*, pp. 905-911
- [136] Shugar, T.A. and M.G. Kalona (1975): "Development of finite element head injury model", *Journal of the engineering mechanics division: ASCE*, **101**, EM3, pp. 223-239.
- [137] Seth B.R. in Reiner M. and D. Abir, Eds. (1964): *Second-Order Effects in Elasticity, Plasticity and Fluid Mechanics*, Pergamon, Oxford, pp. 162-
- [138] Soskey P.R., and H.H. Winter (1984): "Large Step Shear Strain Experiments with Parallel-Disk Rotational Rheometers", *Journal of Rheology*, **28**(5), pp. 625-645.
- [139] Stelwagen, U. and E. Boer (2000): *Ultragehuidsmetingen aan siliconengel*, TNO-Report HAI-RPT-000020, TNO-TPD, Delft, The Netherlands, In Dutch.
- [140] Tarriere, C. (1981): *Head and Neck Injury Criteria - A Consensus Workshop*, pp. 218-228, A.K. Ommaya ed., U.S. Dept. of Transport, NHTSA, Washington D.C., USA.

- [141] Thibault, L.E., Gennarelli, T.A., Margulies, S.S., Marcus, J., and Eppinger, R. (1990): "The strain dependent pathophysiological consequences of inertial loading on central nervous system tissue", *Proceedings IRCOBI conference on biomechanics of impact*, Lyon, France, pp. 191-202.
- [142] Thibault, K.L. and S.S. Margulies (1996): "Material Properties of the Developing Porcine Brain", *Proceedings IRCOBI conference on biomechanics of impact*, Dublin, pp. 75-85.
- [143] Thibault, K.L. and S.S. Margulies (1998): "Age-dependent material properties of the porcine cerebrum: effect on pediatric inertial head injury criteria", *Journal of Biomechanics*, **31**, pp. 1119-1126.
- [144] Thunnissen, J.G.M. Wismans, J.S.H.M., Ewing C.L. and D.J. Thomas (1995): "Human Volunteer Head-neck Response in Frontal Flexion: A New Analysis", *Proceedings 39th Stapp Car Crash Conference*, Paper no SAE 952721, pp. 439-460.
- [145] TNO (1997): *MADYMO Theory manual, Version 5.3*, TNO-Road Vehicles Research Institute, Delft, The Netherlands.
- [146] TNO (1999): *MADYMO User's manual 3D*, Version 5.4, TNO-Automotive, Delft, The Netherlands.
- [147] TNO (1999): *MADYMO Programmer's manual 3D*, Version 5.4, TNO-Automotive, Delft, The Netherlands.
- [148] TNO (2001): *MADYMO Theory manual*, Version 6.0, TNO-Automotive, Delft, The Netherlands.
- [149] Tong, DiMasi, Carr, Eppinger, Marcus and Galbraith (1989): "Finite Element Modeling of Head Injury Caused by Inertial Loading", *12th International Conference on Experimental Safety Vehicles*, Göteborg, pp. 617-627.
- [150] Trosseille, X., Tarrière, C., Lavaste, F., Guillon, F. and A. Domont (1992): "Development of a F.E.M. of the human head according to a specific test protocol", *Proceedings 35th Stapp Car Crash Conference*, SAE Paper 922527, pp. 235-252.
- [151] Turquier, F., Kang, H.S., Trosseille, X., Willinger, R., Lavaste, F., Tarrière, C. and A. Dômont (1996): "Validation Study of a 3D Finite Element Head Model Against Experimental Data", *Proceedings of the 40th Stapp Car Crash Conference*, SAE Paper 962431, pp. 283-294.
- [152] Ueno, K. Melvin, J.W., Li, L. and J.W. Lighthall (1995): "Development of tissue level brain injury criteria by finite element analysis", *Journal of Neurotrauma*, **12**(4), pp.695-706.
- [153] U.S. National Library of Medicine (1996): *The Visible Human Project*, World Wide Web page: http://www.nlm.nih.gov/research/visible/visible_human.html.
- [154] Verhoeve, R.S.J.M. (1998): *Computer Model of the Human Head to Assess Mechanical Brain Loading in Car Collisions*, ISBN 90-5282-941-1, Stan Ackermans Institute, Eindhoven, The Netherlands.
- [155] Versace, J. (1971): "A review of the severity index", *Proceedings of the 15th Stapp Car Crash Conference*, SAE Paper 710881.
- [156] Viano, D., Holst, H. von, and E. Gordon: *Serious brain injury from traffic related causes: Priorities for primary prevention*.
- [157] Viano, D., Aldman, B., Pape, K., van Hoof, J. and H. von Holst (1997): "Brain Kinematics in physical model tests with translational and rotational acceleration", *Int. Journal of Crashworthiness*, **2** (2), pp.191-205.

- [158] Viano, D., Holst, H. von, and E. Gordon (1997): "Serious brain injury from traffic related causes: Priorities for primary prevention", *Accident Analysis & Prevention*, **29**(6), pp. 811-816.
- [159] Vosbeek, P.H.J. (1994): *A Micromechanical Approach to Deformation and Failure of Discrete Media*, Ph.D. Dissertation, Eindhoven University of Technology, Eindhoven, The Netherlands.
- [160] Waxweiler, R.J., Thurman, D., Snizek, J., Sosin, D. and J. O'Niell (1995): "Monitoring the impact of traumatic brain injury: A review and update", *Journal of Neurotrauma*, **12**(4), pp. 509-516.
- [161] Willinger, R. and D. Cesari (1990): "Determination of Cerebral Motion at Impact through Mechanical Impedance Measurement", *Proceedings of the 1990 International IRCOBI Conference*, pp. 203-213.
- [162] Willinger, R., Baumgartner, D., Chinn, B. and E. Schuller (2001): "New dummy head prototype: development, validation and injury criteria", *Int. Journal of Crashworthiness*, **6**(3), pp. 281-293.
- [163] WISQARS (2001): "Leading Causes of Death Report, 1998", in *Web-based Injury Statistics Query and Reporting System (WISQARS)*, Centers for Disease Control and Prevention, Word Wide Web Page: <http://webapp.cdc.gov/sasweb/ncipc/leadcaus.html>.
- [164] Whorlow, R. (ed.) (1992): *Rheological techniques*. Ellis Horwood, Chichester, West Sussex, Great Britain.
- [165] Young, P.G. and C.L. Morphey (1998): "Intracranial Pressure Transients caused by head impacts", *Proceedings IRCOBI conference on biomechanics of impact*, G"oteborg, pp. 391-403.
- [166] Zeidler, F. Pletchen, B., Mattern, R., Alt, B., Miksch, T., Eichendorf, W. and S. Reiss (1989): "Development of a New Injury Cost Scale", *33rd annual proceedings*, Association for the Advancement of Automotive Medicine.
- [167] Zhang, L., Yang, K. H. and A.I. King (2001): "Comparison of brain responses between frontal and lateral impacts by finite element modeling", *Journal of Neurotrauma*, **18**(1), pp. 21-30.
- [168] Zhou, C., Khalil, T.B. and A.I. King (1995): "A New Model Comparing Impact Responses of the Homogeneous and Inhomogeneous Human Brain", *Proceedings of the 39th Stapp Car Crash Conference*, SAE Paper 952714.
- [169] Zhou, C. Khalil, T.B. and A.I. King (1996): "Viscoelastic response of the human brain to sagittal and lateral rotational acceleration by finite element analysis", *Proceedings of the International IRCOBI Conference on the Biomechanics of Impact*, pp.35-48.
- [170] Zoetelief, W. (1992): *On the numerical simulation of the multilayer injection moulding process*, Technical Report WFW 92.100, Eindhoven University of Technology, Eindhoven, The Netherlands

Appendix A

Test of numerical implementation

A series of benchmark tests are performed for determining which integration method has to be used for obtaining sufficient accuracy at time steps commonly used in impact simulations ($\Delta t = O(10^{-6})$ s). It will be shown why the Euler Improved method was chosen instead of a less computationally expensive Euler Forward method. Both methods are compared in the simple shear experiment discussed in Chapter 5. Furthermore different deformation histories have been applied to check the accuracy of the Euler Improved integration method with respect to objectivity and correct decoupling of hydrostatic and deviatoric parts.

A.1 Introduction

As explained in Chapter 5, a time integration scheme is needed to update the inelastic right Cauchy-Green strain tensor C_p using the evolution equation (5.11). In section 5.4 it is shown that the Euler Improved integration scheme is accurate for a simple shear stress relaxation experiment. In this chapter, different loading conditions for testing the numerical accuracy of the material model are applied. It will be shown why the Euler Improved method was chosen instead of a less computationally expensive Euler Forward method. Also analytical solutions are provided which are not shown in the main text. The loading conditions and their motivation are listed below,

1. Simple shear stress relaxation: For comparison of Euler Forward and Euler Improved integration schemes
2. Uni-axial deformation followed by rotation: For testing the objectivity of the formulation
3. Hydrostatic compression: For testing whether the hydrostatic part is purely elastic
4. Combined shear and extension: Checking for residual stresses after cyclic loading and unloading

To perform the simulations, the stress update scheme of Figure 5.6 and both time integration schemes, were implemented in MATLAB 5.3 [89]. Single mode, brain-like material properties were applied according to Table A.1.

A.2 Simple shear stress relaxation

In this section, it will be investigated if the Euler Improved method, which is computational expensive per time step, is really needed for numerical accuracy. The computation time is important when performing crash impact simulations since many degrees of freedom and small time steps are used. A simple shear stress relaxation experiment has been simulated using both Euler Improved and the less computational expensive Euler Forward method (equation (5.35)) and results have been compared.

| Material parameter | Value in load case | | | | Equation number |
|------------------------|--------------------|----------------|----------------|----------------|-----------------|
| | 1 | 2 | 3 | 4 | |
| $C_{10} = C_{01}$ [Pa] | 250 | 250 | 250 | 250 | (5.21,5.25) |
| $C_{20} = C_{02}$ [Pa] | 0 | 0 | 0 | 0 | (5.21) |
| K [Pa] | $1 \cdot 10^9$ | 2000 | $1 \cdot 10^9$ | $1 \cdot 10^9$ | (5.22) |
| λ [s] | 1 | $1 \cdot 10^9$ | 1 | 1 | (5.13,5.26) |

Table A.1: Material parameters typical for brain like tissue used in the simple one-mode test problems performed in MATLAB. Load case numbers correspond with summary in text.

The following deformation gradient tensor history is used,

$$\mathbf{F}(t) = \begin{bmatrix} 1 & \gamma(t) & 0 \\ 0 & 1 & 0 \\ 0 & 0 & 1 \end{bmatrix} \text{ with } \begin{cases} \gamma(t) = 0 & 0 \leq t < 0.5 - \Delta t \\ \gamma(t) = \gamma_0 & 0.5 < t \leq 20 \end{cases} \quad (\text{A.1})$$

in which Δt represents the time step used. The maximum shear strain, γ_0 , was set to 0.2, a strain value commonly associated with brain injury.

For single mode linear viscoelastic material behaviour the analytical solution for the stress history can be obtained (see e.g. [80]) in matrix form,

$$\underline{\sigma}(t) = \begin{bmatrix} \frac{2}{3}\gamma(t)(2C_{10} + C_{01}) & 2(C_{10} + C_{01}) & 0 \\ 2(C_{10} + C_{01}) & -\frac{2}{3}\gamma(t)(C_{10} + 2C_{01}) & 0 \\ 0 & 0 & 0 \end{bmatrix} M(t) \quad (\text{A.2})$$

in which,

$$\begin{cases} M(t) = 0 & t < 0.5 - \Delta t \\ M(t) = \dot{\gamma}_0 \lambda (1 - e^{-(t-0.5+\Delta t)/\lambda}) & 0.5 - \Delta t \leq t \leq 0.5 \\ M(t) = \dot{\gamma}_0 \lambda (1 - e^{-\Delta t/\lambda}) e^{-(t-0.5)/\lambda} & t > 0.5 \end{cases} \quad (\text{A.3})$$

Note that the stress consists of a deviatoric part only, so there will be no volumetric contribution, i.e. $\sigma^v = \mathbf{0}$.

Results

Stress data of a run with the Euler Improved scheme and a time step of 10^{-4} s is shown in the left column of Figure A.1. As expected, σ_{zz} , σ_{yz} and σ_{zx} remain zero. The other stress components show a relaxation behaviour, which is present in the deviatoric stress part only (compare middle and right plots). Furthermore, the right plot shows a straight line indicating indeed a single time constant to be present. However, when observing the volumetric normal stresses in the middle part of the figure, it can be seen that these do not remain zero. This error is caused by numerical inaccuracy in combination with the high bulk modulus, K , used. It decreases with decreasing time step, as shown in Figure A.2. The Euler Improved scheme shows a quadratic convergence whereas the Euler Forward scheme provides linear convergence. The residual stresses were plotted against CPU time in the same figure. It can be concluded that the Euler Improved method provides the best result for a certain, fixed, CPU time.

To investigate the error during stress relaxation in shear stress component, σ_{xy} , the time histories of the relative error at various time steps used have been plotted in Figure A.3. It can be seen that for both methods the relative error decreases to approximately 1% when sufficient small time steps are used. However for the Euler Improved method a time step of 0.01 s suffices to achieve this accuracy whereas $\Delta t = 10^{-4}$ s is required for the Euler Forward scheme.

It can be concluded that the Euler Improved method is computationally more beneficial compared to a simple Euler Forward integration rule, which takes less CPU

effort per time step but requires smaller time steps for given accuracy. For this reason the Euler Improved method is chosen in the numerical model formulation in Chapter 5.

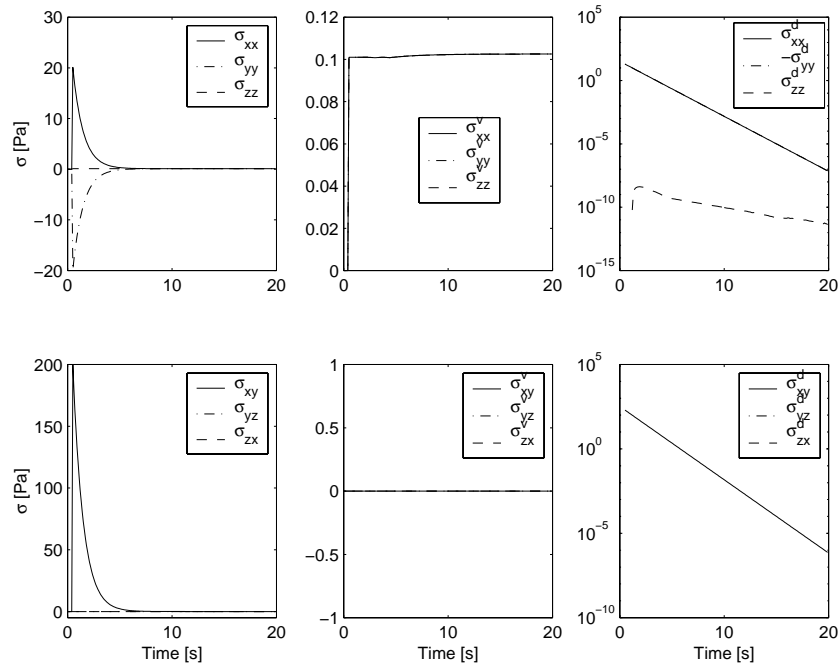


Figure A.1: Simulation results of step response using Euler Improved time integration . $\Delta t = 10^{-4}$ s, $\gamma_0 = 0.2$. Left: Stress components versus time. Middle: volumetric part σ^v . Right: deviatoric part σ^d .

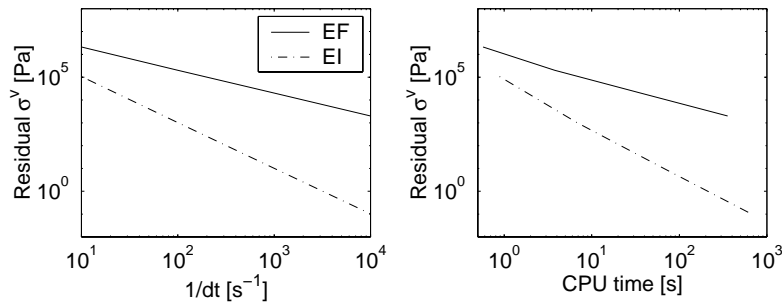


Figure A.2: Convergence study of two integration methods, Euler Forward (EF) and Euler Improved (EI). Left: Residual volumetric stress versus time step. Right: residual volumetric stress versus CPU time of MATLAB simulation.

A.3 Objectivity: uni-axial deformation

For testing the objectivity of the material model, the following deformation history has been applied to a material body,

$$\mathbf{F} = \mathbf{R} \cdot \mathbf{U}$$

with,

$$\underline{\mathbf{R}} = \begin{bmatrix} \cos \phi(t) & \sin \phi(t) & 0 \\ -\sin \phi(t) & \cos \phi(t) & 0 \\ 0 & 0 & 1 \end{bmatrix} \text{ and } \underline{\mathbf{U}} = \begin{bmatrix} \lambda(t) & 0 & 0 \\ 0 & 1 & 0 \\ 0 & 0 & 1 \end{bmatrix} \quad (\text{A.4})$$

the rotation and the elongation tensors, \mathbf{R} and \mathbf{U} , in matrix notation respectively. The time histories for $\lambda(t)$ and $\phi(t)$ are shown in Figure A.4. First an uni-axial compression is applied. Then the compressed material is rotated twice. After this the compression is released and a uni-axial stretch is applied. The compressed material is rotated twice again. After this the material deformation is released again. Elastic material behaviour is obtained by setting the time constant of the damper to 10^9 s. This prevents stress relaxation of the deviatoric stress for better observing the objectivity of the stress. Furthermore the bulk modulus, K , has been lowered to 2000 Pa, since otherwise the hydrostatic part of the stress will overshadow the deviatoric part. The accuracy of the solution has been determined via the analytical solution for the principal stresses. Since $\underline{\mathbf{U}}$ is a diagonal matrix, the principal stresses, σ_{11} , σ_{22} and σ_{33} , can be calculated by substituting $\underline{\mathbf{U}}$ for \mathbf{F} in constitutive equations (5.21) and (5.22). Written in terms of stretch, $\lambda(t)$, this yields,

$$\begin{aligned} \sigma_{11} &= \frac{4}{3}C_{10} (\lambda^{1/3} - \lambda^{-5/3}) - \frac{4}{3}C_{01} (\lambda^{-7/3} - \lambda^{-1/3}) + K (\lambda - 1) \\ \sigma_{22} &= \frac{4}{3}C_{10} (\lambda^{-5/3} - \lambda^{1/3}) - \frac{4}{3}C_{01} (\lambda^{-1/3} - \lambda^{-7/3}) + K (\lambda - 1) \\ \sigma_{33} &= \frac{4}{3}C_{10} (\lambda^{-5/3} - \lambda^{1/3}) - \frac{4}{3}C_{01} (\lambda^{-1/3} - \lambda^{-7/3}) + K (\lambda - 1) \end{aligned} \quad (\text{A.5})$$

The principal stresses of the numerical solution have been determined as the eigenvalues of the Cauchy stress matrix using the EIG command in MATLAB [89].

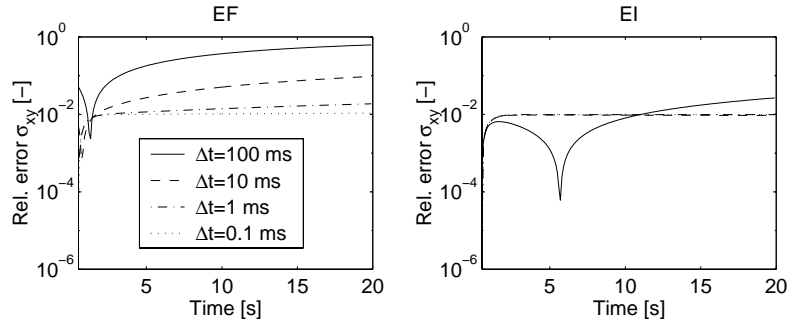


Figure A.3: Relative error histories for shear stress as a function of time step and integration method used (relative error definition in equation (5.37)). Left: Euler Forward results (EF), Right: Euler Improved results (EI).

Results

The resulting Cauchy stresses are shown in Figure A.4 in both fixed coordinates (lower left graph) as well as in principal directions (lower right graph). The relative error in the principal stresses is on the order of $5 \cdot 10^{-9}$ when $\Delta t = 0.01$ s. Increasing the bulk modulus to 2 GPa provides relative errors on the order of 10^{-13} while $K = 0$ provides maximum relative errors of $6 \cdot 10^{-9}$.

A.4 Hydrostatic compression

A hydrostatic compression is applied as to assess whether the deviatoric part is completely decoupled from the hydrostatic part in the numerical implementation. Since viscous behaviour acts on the deviatoric part only, no viscous effects are expected during hydrostatic compression. The following deformation tensor is applied,

$$\mathbf{F} = \lambda(t)\mathbf{I} \quad (\text{A.6})$$

From this it follows that $\mathbf{B} = \lambda^2(t)\mathbf{I}$ and $\overline{\mathbf{B}}^d = \mathbf{0}$. As a result the Cauchy stress will be purely volumetric and elastic,

$$\boldsymbol{\sigma}(t) = \boldsymbol{\sigma}^v(t) = \lambda^3(t)K_1\mathbf{I}$$

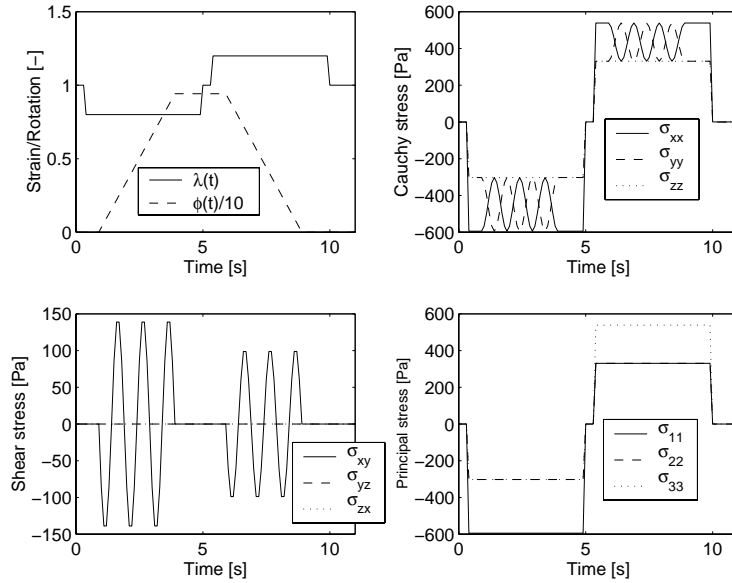


Figure A.4: In and output data from combined uni-axial extension and compression with $\Delta t = 0.01$ s. Upper left: Prescribed elongation $\lambda(t)$, and rigid body rotation angle $\phi(t)$. Upper right, lower left: Cauchy stress components, Lower right: Principal stresses, sorted $\sigma_{11} > \sigma_{22} > \sigma_{33}$.

The elongation factor $\lambda(t) = 0.8$ for $0.5 < t < 5$ s and $\lambda(t) = 1.2$ for $10 < t < 15$ s. At other moments in time between 0 and 20 s, $\lambda(t) = 1$. Viscoelastic material parameters according to Table A.1 are used.

Results

The results of a simulation using $\Delta t = 0.1$ s are shown in Figure A.5. It can be seen that the deviatoric stress remains indeed close to zero (10^{-14}), whereas relaxation is absent in the volumetric stress. The relative error found when comparing the volumetric stress values during the with analytical ones was on the order of 10^{-32} .

A.5 Combined shear and extension: cyclic loading and unloading

A cycle of applying simple shear, stretching the sheared volume in one direction with elongation factor $\lambda(t)$, releasing the shear strain and releasing the stretch has been simulated. The objective of this exercise is to investigate the residual stresses after this cyclic loading.

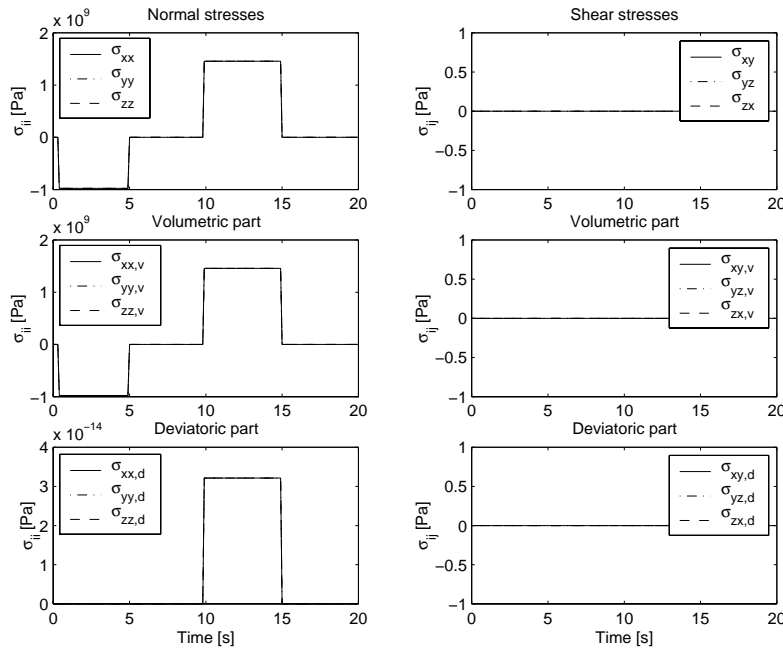


Figure A.5: Stress history for hydrostatic compression experiment. Upper: Total Cauchy stress. Middle: Volumetric part. Lower: deviatoric part.

The deformation gradient tensor can be written as,

$$\mathbf{F}(t) = \begin{bmatrix} 1 & \gamma(t) & 0 \\ 0 & \lambda(t) & 0 \\ 0 & 0 & 1 \end{bmatrix} \quad (\text{A.7})$$

in which $\lambda(t)$ and $\gamma(t)$ are chosen as shown in Figure A.6. The residual volumetric normal stresses and normal deviatoric stresses at the end of the simulation for both integration methods are compared with each other.

Results

It is shown in Figure A.7 that the residual normal volumetric stresses converge to zero when a sufficiently small time step is used. This convergence is quadratic when the Euler Improved scheme is used. Extrapolating this result to a time-step $\Delta t = 10^{-6} s$ provides a volumetric stress on the order of $10^{-5} Pa$ as was the case in the simple shear experiment. The residual deviatoric stresses converge to a constant value which corresponds with the relaxed stress present at that time.

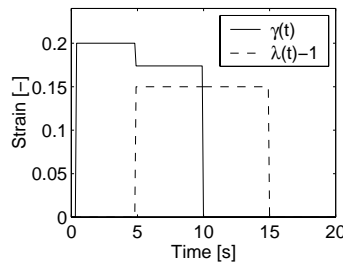


Figure A.6: Deformation history of combined shear and extension case.

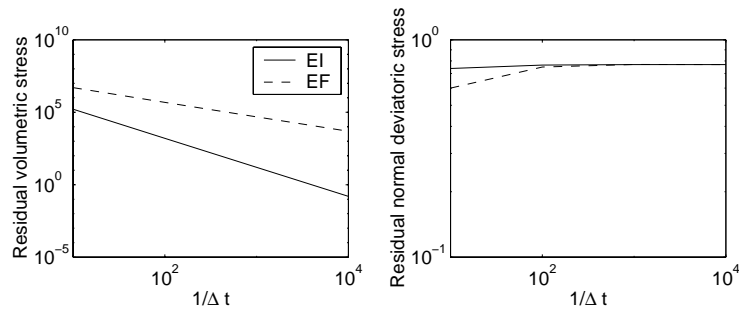


Figure A.7: Residual normal stresses. Left: Erroneous volumetric stresses, Right: Deviatoric stresses. EI: Euler Improved, EF: Euler Forward.

A.6 Conclusions

- Application of the Euler Improved integration method is needed for reducing errors to acceptable values when time steps on the order of 10^{-6} s, typical in automotive impact simulations are used.
- The numerical implementation of the Cauchy stress formulation meets the objectivity requirement.
- Hydrostatic deformation is completely decoupled from the deviatoric deformation.
- Cyclic loading and unloading, another potential cause of errors did not lead to different error causes than the ones discussed for the simple shear simulation in Chapter 5.

Appendix B

Modification of non-linear viscoelastic material model

The non-linear material model presented in Chapter 5 describes the behaviour of brain tissue for simple shear strains up to 20%. However, for strains outside this strain region, negative stiffness can occur due to the negative second order Mooney-Rivlin parameters applied. To prevent this from happening, the model is modified as to ensure that the influence of this correction within the validated range of 0 to 20% shear strain is as small as possible. To retain maximum biofidelity, the model is fitted to the experimental results again. As with the original model, the predicted response outside the experimental strain range does not resemble brain tissue behaviour, in fact strain stiffening behaviour will be predicted whereas brain tissue is expected to show shear softening (recall that shear softening only means a decrease in stiffness, not negative stiffness). The solution presented in this appendix should be seen as a method for preventing numerical problems in cases when localised high strains in a model are unavoidable.

B.1 Modification of the model

The fits on the damping functions in Chapter 5 provide negative second order Mooney-Rivlin parameters, C_{02} and C_{20} . This results in negative stiffness values when strains are beyond the 20% shear strain for which the model is validated experimentally. This is not wanted since this does not resemble brain tissue behaviour [123]. Furthermore it causes numerical problems.

The simplest manner of preventing negative stiffness without altering the complete material model is by adding a stress contribution that has negligible effect at small strains but overrules the negative stiffness induced by the second order parameters at large strains. In present model this is achieved by adding positive third order Mooney-Rivlin terms. The isochoric part of the SED, equation (5.20), then becomes,

$$\bar{W} = C_{10}(\bar{I}_1 - 3) + C_{01}(\bar{I}_2 - 3) + C_{20}(\bar{I}_1 - 3)^2 + C_{02}(\bar{I}_2 - 3)^2 + C_{30}(\bar{I}_1 - 3)^3 + C_{03}(\bar{I}_2 - 3)^3 \quad (\text{B.1})$$

The deviatoric part of the Cauchy stress tensor, σ^d , derived from this SED, becomes,

$$\sigma^d = \frac{2}{J_e} \left\{ C_{10} + 2C_{20}(\bar{I}_1 - 3) + 3C_{30}(\bar{I}_1 - 3)^2 \right\} \bar{\mathbf{B}}_e^d - \frac{2}{J_e} \left\{ C_{01} + 2C_{02}(\bar{I}_2 - 3) + 3C_{03}(\bar{I}_2 - 3)^2 \right\} (\bar{\mathbf{B}}_e^{-1})^d \quad (\text{B.2})$$

The volumetric part is left unaltered. In this manner, the occurrence of negative stiffness is prevented without losing the advantages of a hyperelastic formulation.

B.2 Requirements for positive stiffness

To prevent negative stiffness during an arbitrary deformation the incremental stiffness tensor, or Jacobian $\mathbf{J} = \partial\sigma/\partial\varepsilon$ should be determined (in which ε is the incremental, infinitesimal strain). When all eigenvalues of the Jacobian tensor are greater than 0, the incremental stiffness is larger than zero [159]. For an incremental material formulation this check can be performed relatively easy. However, for the present material model a total Lagrangian form is used. To check for negative stiffness then would imply explicit derivation of the incremental stiffness matrix at every time step before its eigenvalues can be determined. This is unwanted from a computational costs point of view.

For this reason, a more simple approach is chosen in this dissertation. It is assumed that simple shear is the strain situation most critical for the occurrence of negative incremental stiffness. During simple shear, the shear stress, σ_{ij} , given by the third order Mooney-Rivlin equation (B.2) can be written as,

$$\sigma_{ij} = 2(C_{10} + C_{01})\gamma + 4(C_{20} + C_{02})\gamma^3 + 6(C_{30} + C_{03})\gamma^5 \quad (\text{B.3})$$

Positive incremental stiffness now can be obtained by requiring,

$$\frac{\partial\sigma_{ij}}{\partial\gamma} = G_{min} \quad (\text{B.4})$$

for every shear strain, γ . Stiffness, G_{min} , is an arbitrarily chosen minimum, positive, stiffness that is allowed in the simple shear solution. By writing G_{min} as a fraction, α , of the small strain shear stiffness,

$$G_{min} = 2\alpha(C_{10} + C_{01}) \quad (\text{B.5})$$

the sum of the third order terms can be solved from equation (B.4),

$$C_{30} + C_{03} = \frac{3f_{nls}^2}{5 - 5\alpha} (C_{10} + C_{01}) \quad (\text{B.6})$$

in which $f_{nls} = \frac{C_{20} + C_{02}}{C_{10} + C_{01}}$, the non-linear shear parameter. By posing the additional assumption that $C_{30} = C_{03}$, as done for the first and second order parameters, the third order parameters are defined.

B.3 Determination of brain tissue material parameters

As the modification acts on the strain dependent behaviour only, the only parameter influenced by this modification is the non-linear shear parameter, f_{nls} . This parameter has been fitted again to the experiment data. The damping function used for fitting is already corrected for inhomogeneous strain field with the original model (refer to Chapter 5)).

For simple shear, the damping function of the third order Mooney-Rivlin formulation can be written as,

$$h(\gamma) = 1 + 2\gamma^2 \frac{C_{02} + C_{20}}{C_{01} + C_{10}} + 3\gamma^4 \frac{C_{03} + C_{30}}{C_{01} + C_{10}} \quad (\text{B.7})$$

By eliminating $C_{03} + C_{30}$ from equation (B.7) using equation (B.6), the damping function becomes,

$$h(\gamma) = 1 + 2\gamma^2 f_{nls} + \frac{9}{5}\gamma^4 \frac{f_{nls}^2}{1 - \alpha} \quad (\text{B.8})$$

This function, with $\alpha = 0$ is fitted to the damping function.

Fit results

Fitting the damping function of equation (B.7) to the corrected data of Chapter 5 provides $f_{nls} = -5.5553$. Figure B.1 shows the fits of the damping functions within the experimental range. It can be seen that the modified model (MR3) fit differs slightly from the original fit presented in Chapter 5. This is confirmed by the mean error and standard deviation of the error at each experimental data point. This error equals $4.5 \cdot 10^{-3} \pm 8.8 \cdot 10^{-3}$ and is higher than the original fit (error: $3.0 \cdot 10^{-3} \pm 8.6 \cdot 10^{-3}$) but still acceptable. The damping functions for strains beyond the experimental range are shown in the right graph in Figure B.1. The original fit decreases below zero while the modified fit starts to increase again after a certain strain. Table B.1 provides an overview of all material parameters fitted with the modified material model.

B.4 Implications for material behaviour

The implications of the modification for the elastic stress behaviour are illustrated using simple shear results using the elastic mode of Table B.1 only. The left graph in Figure B.2 shows that differences between modified and original model are indeed

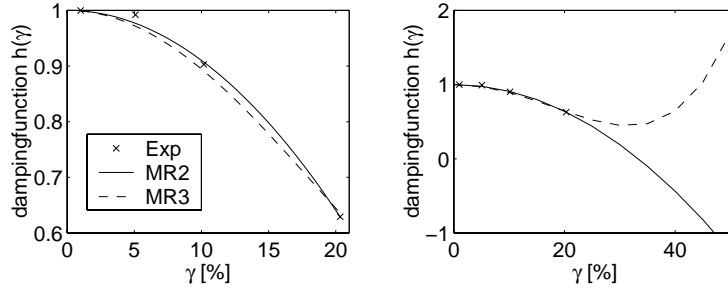


Figure B.1: Effect of modification on damping function. Fits of original (MR2) and modified (MR3) model versus corrected experimental data from G2 sample (Exp) (refer to Chapter 4). Left: Experimental strain range. Right: Larger strain range.

Table B.1: Material parameters obtained from fitting the modified non-linear material model on brain tissue shear data (sample G2 in Chapter 4)

| Mode | Maxwell parameters | | Non-linear parameters | | | Bulk modulus |
|------|---------------------------------|------------------|-----------------------|----------------|----------------|--------------|
| | $G_i = 2(C_{10} + C_{01})$ [Pa] | λ_i [ms] | f_{nls} [-] | f_1 [-] | f_2 [-] | |
| 0 | 255.26* | ∞ | -5.5553 | 1 ⁺ | 1 ⁺ | 2.5 |
| 1 | 269.08 | 70.1 | -5.5553 | 1 ⁺ | 1 ⁺ | 0 |
| 2 | 322.63 | 7.63 | -5.5553 | 1 ⁺ | 1 ⁺ | 0 |
| 3 | 426.96 | 1.41 | -5.5553 | 1 ⁺ | 1 ⁺ | 0 |
| 4 | 3299.4 | 0.123 | -5.5553 | 1 ⁺ | 1 ⁺ | 0 |

* G_0 obtained from stress relaxation data using equation (5.31)

+ Constants chosen arbitrarily, could not be determined from shear experiments

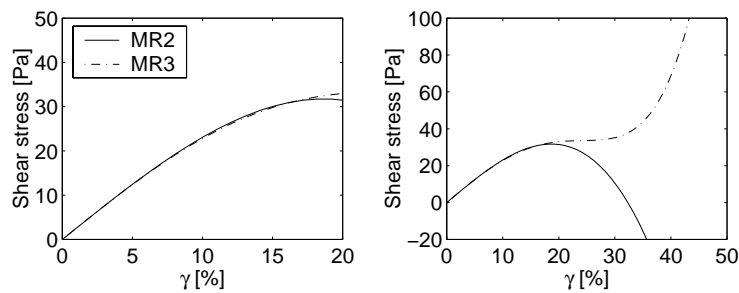


Figure B.2: Shear stress versus strain. Elastic material behaviour assumed by modelling only the elastic mode in Table B.1. Fits of original (MR2) and modified (MR3) model used. Left: Experimental strain range. Right: Larger strain range.

small for strains up to 20%. The right graph shows that the original model already predicted negative incremental stiffness for strains exceeding approximately 19%. For larger strains the stress decreases until negative values occur at 32% strain approximately. The modified model shows a monotonically increasing stiffness. For strains over 34% the stiffness exceeds the initial small strain stiffness, whereas for strain above 42% the model predicts higher stresses than a linear material model would have done.

B.5 Discussion and conclusions

The non-linear viscoelastic material model presented in Chapter 5 has been modified to prevent negative stiffness at strains beyond the validity range of the original model by adding a third order Mooney-Rivlin term to the original second order formulation. In this manner advantages of a hyper elastic formulation (no energy absorption, objectivity) are maintained.

As the stress dependent behaviour of the material has been altered, the non-linear shear parameter is fitted to the experimental determined dampingfunction again.

Simple shear simulations showed that negative strains are indeed prevented by the modification, but for strains over 34%, the incremental stiffness exceeds the initial small strain stiffness. The model then actually does not predict shear softening anymore but shear stiffening. Furthermore, this may lead to instability of the, conditionally stable, explicit Central Difference Time integration scheme used (refer to section dealing with the Courant number in Chapter 2 for details).

It can be concluded that the model still describes the shear behaviour of brain tissue when strains do not exceed 20%. For larger strains, biofidelity is not guaranteed but numerical problems due to negative stiffness are prevented. However, it is recommended to prevent these strains from being present in the model.

Samenvatting

Jaarlijks overlijden er meer dan een miljoen mensen aan verkeersongevallen terwijl er meer dan honderdmiljoen gevallen met letsel voorkomen. Bij een ongevalssituatie is het hoofd een van de meest kwetsbare delen van het menselijk lichaam. Om te begrijpen hoe een inslag op het hoofd tot hersenletsel leidt, is het belangrijk de mechanische responsie van het hoofd te kennen. Het is niet mogelijk om deze responsie met behulp van *in-vivo* experimenten (experimenten met levende wezens) te bepalen. Daarom worden vaak numerieke eindige-elementenmodellen (E.E.M.) gebruikt. De huidige E.E.M. van het hoofd bevatten een zeer gedetailleerde weergave van de anatomie maar zijn sterk vereenvoudigd m.b.t. de beschrijving van het materiaalgedrag van het hersenweefsel en de contact interacties tussen de verschillende anatomische delen van het hoofd. Ook treden er fouten op door de gebruikte numerieke benaderingsmethode, de expliciete eindige-elementenmethode. De doelstelling van deze studie is het verbeteren van eindige-elementen hoofdmodellen, met name de volgende twee aspecten: de nauwkeurigheid van de numerieke methode en de beschrijving van het materiaalgedrag van de hersenen. Om de nauwkeurigheid van de numerieke methode te bepalen dienen we eerst te weten welk type mechanische responsie te verwachten valt. Met name golfverschijnselen zijn hierbij van belang daar deze hoge eisen stellen aan de numerieke methoden. Een analytische studie naar de inslagomstandigheden waarbij golfffenomenen in de hersenen kunnen voorkomen gaf aan dat het waarschijnlijk is dat ze aanwezig zijn. Afschuifgolven (S-golven) worden verwacht tijdens verkeersongevallen (frequenties tussen 25 Hz en 300 Hz). Druk golven (P-golven) kunnen ontstaan bij hoge-snelheidsinslagen (bijvoorbeeld kogel inslagen op het beschermde hoofd) bij frequenties tussen de 10 kHz en 3 MHz .

Uit het voorafgaande volgt dat de numerieke methode voor het modelleren van een hoofd gedurende een inslag geschikt moet zijn om golfffenomenen nauwkeurig te kunnen beschrijven. Daarom is een analytische nauwkeurighedsanalyse van bestaande hoofdmodellen uitgevoerd. Deze analyse is geldig voor kleine rekken en laat zien dat er twee typen fouten ontstaan in eindige-elementensimulaties van golfffenomenen: numerieke dispersie en numerieke reflecties. Deze fouten worden beïnvloed door de discretisatie in ruimte en tijd. Bijgevolg zullen de voorspelde rekken en reksnelheden incorrect zijn. Daar deze grootheden geassocieerd worden met het ontstaan van letsels is correcte voorspelling noodzakelijk. Met de elementgrootte typisch voor huidige hoofdmodellen (meer dan 5 mm) kunnen

golffenenomenen niet nauwkeurig gemodelleerd worden. Voor het modelleren van afschuifgolven moet de elementgrootte met een factor tien verkleind worden. Voor het modelleren van drukgolven zou de elementgrootte met een factor honderd verkleind moeten worden. Dit geeft echter onrealistisch grote modellen. Daarom zal er voor dit type golven gezocht dienen te worden naar andere discretisatie methoden in ruimte en tijd. Daar dit geen doelstelling was van dit onderzoek wordt in het vervolg alleen nog maar afschuifgedrag beschouwd.

Het mechanische gedrag van hersenweefsel is onderzocht met behulp van afschuifexperimenten. Voor kleine rekken werden experimenten met een harmonisch geëxciteerde rek (amplitude 1%) gebruikt. Door toepassing van het zogeheten Tijd Temperatuur Superpositie beginsel konden materiaal gegevens verkregen worden bij frequenties die relevant zijn bij verkeersongevallen (maximaal 1000 Hz). Afschuifrekken die verantwoordelijk geacht worden voor het ontstaan van van letsel (20% afschuifrek) werden toegepast in spanningsrelaxatie experimenten. Hersenweefsel blijkt zich als een niet-lineair viscoelastisch materiaal te gedragen bij rekken boven 1%. De afschuifstijfheid neemt af bij toenemende rekken terwijl het tijdsafhankelijke gedrag bijna onafhankelijk is van de opgelegde rek.

Gebaseerd op de experimentele bevindingen is een materiaalmodel ontwikkeld. Het model is een niet-lineaire uitbreiding van het multi-mode Maxwell model. De rektensor wordt gesplitst in een elastisch en een inelastisch deel via een multiplicatieve decompositie. Het inelastische, tijdsafhankelijke gedrag is gemodelleerd als een eenvoudige Newtonse vloeistof. Het rekafhankelijke, elastische deel is gemodelleerd met een hyperelastische formulering (2de orde Mooney-Rivlin). De modelformulering is geschikt om anisotroop gedrag (zoals aangetoond aanwezig in sommige delen van de hersenen) te implementeren maar voor deze studie is voornamelijk isotroop materiaalgedrag aangenomen. Materiaalparameters voor hersenweefsel werden bepaald uit de kleine-rekexperimenten en het constante rekdeel van de spanningsrelaxatie experimenten.

Het materiaalmodel is geïmplementeerd in het expliciete eindige-elementenpakket MADYMO. Om bij modelleren van het bijna incompressibele hersenweefsel, met gangbare tijdstappen, nauwkeurige oplossingen te krijgen is een predictie-correctie integratie methode toegepast. De spanningsrelaxatie-experimenten, inclusief het transiënte deel van de rekgeschiedenis dat niet voor parameterfitten gebruikt is, zijn met succes gesimuleerd.

Om zowel de bevindingen over numerieke nauwkeurigheid en de constitutieve formulering te testen is een laboratorium hoofdmodel ontwikkeld. Het dynamische gedrag van de hersenen is nagebootst met Dow Corning Sylgard 527 A&B siliconengel. De mechanische eigenschappen van deze gel zijn op de zelfde manier bepaald als die van hersenweefsel. De gel gedraagt zich lineair viscoelastisch voor de geteste rekniveaus tot 50% afschuiving. De materiaalparameters van de siliconengel liggen dicht bij die van hersenweefsel al is er meer materiaaldemping bij hoge frequenties. Er is geconcludeerd dat deze siliconengel gebruikt kan worden in een laboratorium hoofdmodel voor trend studies en testen van numerieke modellen. Een cilindervormig bakje, gevuld met siliconengel, is belast met een transiënte hoekversnelling zoals die bij een verkeersongeval kan voorkomen. De vervorming

van de gel is geregistreerd met behulp van marker detectie in high-speed video-opnamen. De gel is gemodelleerd met het nieuwe constitutieve model en de laboratorium hoofdmodel experimenten zijn gesimuleerd. De experimentele en numerieke resultaten vertoonden grote overeenkomsten. Dit geeft aan dat het materiaalmodel inderdaad een realistische responsie kan beschrijven. Ook het belang van een correcte splitsing van volumetrische en deviatorische deformatie in de spanningsformulering bij het modelleren van bijna niet-samendrukbare materialen is aangetoond.

Tenslotte is het materiaalmodel toegepast in een bestaand 3-dimensionaal model van het menselijke hoofd. De belasting op het hoofd (een excentrische rotatie) was zo gekozen dat de rekniveaus in de experimentele range lagen. Resultaten met en zonder toepassing van niet-lineair materiaalgedrag werden vergeleken. Het niet-lineaire materiaalgedrag zorgde ervoor dat de rekniveaus met 21% toenamen terwijl de spanningsniveaus met 11% daalden. De ruimtelijke verdeling en de tijdsgeschiedenis veranderden echter nauwelijks. Het effect van het niet-lineaire materiaalgedrag is echter maar voor één belasting conditie onderzocht. Ook de manier waarop andere structuren in het hoofd gemodelleerd zijn zullen de responsie, en dus het effect van niet-lineair materiaalmodel beïnvloeden. Verder onderzoek hierna wordt sterk aanbevolen.

Verder was het opvallend dat rekken in het model bereikt werden die geassocieerd worden met het ontstaan van letsel (20%) bij een belasting op het hoofd die veel lager was dan belastingen die in de literatuur met letsel in verband gebracht worden. Een mogelijke oorzaak hiervoor is dat de stijfheid van het hersenweefsel in hoofdmodellen uit de literatuur te hoog is in vergelijking met materiaalgegevens uit de recente literatuur en uit eigen experimenten. Een andere mogelijke verklaring kan zijn dat er wellicht toch een (zwakke) koppeling tussen deviatorisch en volumetrisch deel van de rek in het materiaalmodel aanwezig dient te zijn.

Dankwoord

Graag wil ik iedereen bedanken die op welke manier dan ook heeft meegeholpen aan het tot stand komen van mijn proefschrift en aan het aangenaam maken van mijn periode als promovendus bij de Technische Universiteit Eindhoven.

Allereerst wil ik mijn copromotor Peter Bovendeerd bedanken. Peter, jouw didactische vaardigheden en vermogen om elk probleem terug te brengen naar fundamentele theorie waren erg verhelderend. Verder was het altijd fijn een bakkie koffie te scoren/tanken. Jammer dat jij dit vakgebied gaat verlaten. Peter, veel succes met je troetelkindje, de hartmechanica. Ook Gerit Peters, bedankt voor jouw inbreng m.b.t. materiaalkarakterisering en je welgemeende interesse in dit vakgebied.

Er was een grote toestroom van studenten die middels stages en afstudeer opdrachten een grote bijdrage leverden aan dit onderzoek. Dit onder andere door de PR van Peter tijdens een studiereis in Amerika. Daarom wil ik jullie, Niels Plasmans, Michiel Roersma, Maarten van der Burght, Ronald Faassen, Erik Folgering, Roy Bours, Jiska Kotte, Patricia Bax, Olaf Bressers en Marijn Theulings bedanken voor jullie inzet.

Rob van de Berg, bedankt voor het bouwen van het laboratorium hoofdmodel. Niet alleen jouw vaardigheden op het gebied van draaien, frezen, schroeven, enz. maar vooral ook voor jouw vermogen om van een simpele schets een bruikbare opstelling te maken.

Ook de mensen bij de afdeling MADYMO bij TNO-Automotive in Delft wil ik bedanken voor de door hun verleende faciliteiten bij het implementatie van het materiaalmodel. Met name Pier Nauta, bedankt voor jouw inzet, meedenken en hulp bij het implementeren.

Uiteraard wil ik Jan van Bree van TNO-PML in Rijswijk niet vergeten. Jij was initiator van dit onderzoek en hebt voor de financiële ondersteuning vanuit TNO-Prins Maurits Laboratorium zorggedragen. Wat ik erg gewaardeerd heb aan onze samenwerking is de vrijheid die ik gekregen heb om dit onderzoek naar eigen inzicht in te kunnen vullen.

Verder wil ik mijn collega's bedanken die ervoor zorgen dat de werksfeer hier erg goed is. Mijn mede-bestuursleden 1998-1999 van het AiO genootschap Hora Est zijnde Eric van den Bosch, Liesbeth Geerts, Alex Serrarens en Henri Brouwers. Met name het survival weekend en de excursie naar het pathologisch museum in Nijmegen en de daarop volgende gebeurtenissen waren voor mij onvergetelijke ervaringen.

Ook mijn kamergenoten wil ik niet vergeten. Frans Duinhouwer jij was het die het online Doomen (na werktijd) introduceerde in de vakgroep. Mariëlle Bosboom, als er

ook maar iets was dat geregeld moest worden was jij het die als echte regelneef ervoor zorgde dat we niets te kort kwamen op onze kamer. En last but zeker not least, Eric van den Bosch, mede-biker en vraagbaak voor menig MATLAB of \LaTeX probleem. De manier waarop wij elkaar aanvoelden op het gebied van zinnige en onzinnige zaken grensde aan telepathie. Eric, bedankt voor jouw motivatie door jouw optimistische kijk op zaken (wederzijdse motivatie technieken) en veel succes in jouw toekomst. Verder wil ik mijn ouders bedanken voor hun stimulans om aan deze studie te beginnen. Tenslotte jou, lieve Bianca, jij was er altijd als ik je nodig had en ik was er vaak genoeg niet voor jou. Nu kan ik er wat meer voor jou zijn.

Curriculum Vitae

Dave Brands was born on February 8, 1972 in Maastricht, The Netherlands. He studied Mechanical Engineering at Eindhoven University of Technology, The Netherlands. He received his Master's degree in November 1996 on Finite Element Modelling of a motor cycle helmet during impact. This research was conducted at The Netherlands Research Organisation, TNO, Road Vehicles in Delft, The Netherlands. During this study he got interested in impact biomechanics research. He decided to continue in this field and started this Ph.D. study in February 1997 at Eindhoven University of Technology, within the section Dynamics and Biomechanics of Prof.dr.ir. Dick van Campen and Prof.dr.ir. Jac Wismans. This work was supported by the Prins Maurits Laboratory of The Netherlands Research Organisation, TNO in Rijswijk, The Netherlands. During this research he received the Stapp Car Crash Conference Student Award in 1999. As of July 15, 2001 Dave is employed at the Materials Technology group in the section mechanical engineering at Eindhoven University of Technology.

